Variability in ISOW vigor over the last 1300 years and its relationship to climate

By

Tor Lien Mjell

MASTER THESIS IN GEOLOGY

Field of study: Marine geology and paleoclimate

Department of Earth Science

University of Bergen

June 2009

ABSTRACT

Resolving the scale and origins of recent low frequency (decadal-centennial) climate variations, such as the AMO, is crucial for predicting how natural variability and anthropogenic forcing will interact to affect future climate evolution. These multi-decadal to centennial variations are often postulated to involve, or even be driven by, changes in the Atlantic Meridional Overturning Circulation (AMOC). Assessing this hypothesis for events such as the Little Ice Age (LIA) and the Atlantic Multidecadal Oscillation (AMO) requires records capable of depicting multidecadal changes in past ocean circulation.

Here we use well dated (^{210}Pb and AMS ^{14}C), high sedimentation rate, multi and gravity cores taken on the Gardar Sediment Drift (60°19N, 23°58W, 2081 m water depth) to reconstruct decadal to centennial variability in the properties and vigor of the eastern branch of the Nordic Seas overflows over the past millennium. The Gardar drift accumulates on the eastern flank of the Reykjanes ridge due the supply of sediments provided by the overlying Iceland Scotland Overflow Water (ISOW)—an important component of NADW. We reconstruct the bottom water physical and chemical properties of ISOW using the oxygen and carbon isotopes of benthic foraminifera (C. *wuellerstorfi*), while changes in the vigor of near bottom flow are inferred from size variations in the sediment mean sortable silt ($\overline{\text{SS}}$). The data produced to date provide a sub-decadally sampled history of ISOW variability spanning the last ~1300 years. In addition, changes in surface hydrography are reconstructed using δ^{18}O of the planktonic foraminifer species *G. bulloides*, *N. pachyderma* (d), and *G. inflata*.

This study provides the first evidence that AMOC variability is tightly coupled to low frequency variations in basin-wide climate (AMO). Our results show multi-decadal and centennial variability in ISOW vigor throughout the past ~1300 years. During the past ~350 years ISOW vigor is in phase with reconstructed AMO on both inter-decadal and centennial timescales—with increased (decreased) ISOW vigor during warm (cold) AMO phases. This strong coherence suggests that low frequency variability in key components of AMOC is tightly coupled to basin wide temperature perturbations. However, our reconstructions of local near surface hydrography are out of phase with both the ISOW vigor and basin scale temperature pattern (AMO). This we attribute to variations in the dynamics of the Atlantic subpolar gyre rather than basin-wide climate, possibly related to NAO forcing.

ACKNOWLEDGEMENTS

First of all, I would like to express my greatest gratitude to my supervisors Ulysses S. Ninnemann and Helga (Kikki) F. Kleiven for their excellent guidance, discussion and assistance throughout this period, and for giving me the opportunity to work on such an interesting and challenging topic. I would also like to thank Dr. Ian Hall at the University of Cardiff for his guidance and instructions while acquiring the astonishing mean sortable silt data, Eirik Vinje Galaasen for helping me while acquiring the mean sortable silt data, Shauna McAuley at the University of Belfast for producing the *G. inflata* data, and Rune Søraas at the GMS laboratory at BCCR for his useful instructions and guidance in using the mass spectrometers.

I am very grateful to my supervisors and the Bjerknes Centre for Climate Research for giving me the opportunity and economical support to take part in the AMOCINT cruise in the North Atlantic Ocean during summer 2008, and for the great experience I obtained from the AGU conference in San Francisco in December 2008, giving me the opportunity to present my study to a broad scientific audience.

A thank to the scientific party for very cheerful company during the AMOCINT cruise, and fellow students and scientists for great company during AGU

I would also like to thank my fellow students at the Institute of Earth Science for great company and friendship during these five years and of course my family for mental and financial support throughout all my studies.

Bergen, June 2009

Tor Lien Mjell

1 INTRODUCTION

1.1 Projects

This study contributes to two research projects at the Bjerknes Centre for Climate Research (BCCR): “Resolving the AMOC-Climate connection over the last 1500 years”, an internal Research Group 1 (Dynamics of Past Climate Variability-Marine Paleoclimatology), and “Thermohaline Overturning-at Risk?” (THOR), a large scale integrating EU FP7 project. This thesis has been supervised by Associate Professor Dr. Ulysses S. Ninnemann and Dr. Helga (Kikki) F. Kleiven from the Department of Earth Science, and BCCR at the University of Bergen.

1.1.1 Resolving the AMOC-Climate connection over the last 1500 years

This project’s main goal is to invoke a better understanding of the Atlantic Meridional Overturning Circulation (AMOC) and its response to the ongoing global warming. Low frequency multidecadal climate variations like the Atlantic Multidecadal Oscillation (AMO), and multidecadal-centennial variations like the Little Ice Age (LIA), are often postulated to involve, or even be driven by, changes in the AMOC. Presently, there is no direct evidence linking changes in the AMO with changes in the AMOC. Therefore a better characterization of AMO’s behavior and origin is crucial to predict the future evolvement of the AMOC. Lund et al. (2006), presented evidence showing that the transport in the Gulf Stream decreased and surface salinity increased during the LIA. However, it is not possible to infer changes in the AMOC from ocean surface circulation alone; thus paleo-reconstructions from the deep overflowing branches are needed to asses if the AMOC changed during the LIA.

In order to address these problems, the project concentrates on four main objectives: **1)** To investigate if the production rate and intensity of the Nordic Seas overflow waters changed during the LIA, which is the most recent of the multidecadal-centennial climate changes; **2)** investigate whether AMO variations are present in the surface inflowing branches to the Nordic Seas and the deep outflowing branches; **3)** whether or not AMO variations are found in the surface and deep waters, the project will investigate whether the intensity and frequency of the AMO is stable through the LIA and after; **4)** investigate the possibility that the LIA is a longer lasting version of AMO.

1.1.2 Thermohaline Overturning-at Risk? (THOR)

THOR is an EU FP7 project involving scientists from 10 different nations. The project's main purpose is to contribute to a better understanding of the strength and variability of the ocean's Thermohaline Circulation (THC) and the effect it has on climate, with special emphasis on the North Atlantic/European region. THOR aims to broaden our understanding of the THC in the North Atlantic by establishing a system that will monitor and forecast decadal changes in the THC, to better assess its stability and the possibility of a reduction, or even shut-down, of the THC in the future, as a response to the ongoing global warming. The project is organized into 5 core themes. The present study is part of core theme 1.

Core Theme 1: Quantifying and modeling THC variability using paleoclimate observations and simulations

Core Theme 1 aims to reconstruct the THC variability over the last millennium on decadal-centennial resolution by using paleo-reconstructions from high resolution marine sediment cores and model simulations. The BCCR is involved in reconstructing the properties and variability of the Nordic Seas overflow waters on multidecadal-centennial resolution on both the eastern branch of the overflow (Gardar Drift), and the integrated overflows (Eirik Drift). Furthermore, the reconstructions of the deep overflows will be compared with surface hydrography reconstructions (salinity/SST) in order to investigate the link between variations in the deep overflowing branches and climate. The BCCR will specifically investigate whether multidecadal climate variations like the AMO are mirrored in the deep overflowing branches.

1.1.3 Key questions and objectives

1. What is the natural variability in the Nordic Seas overflows, and how does it relate to climate on decadal to centennial timescales?

- This thesis aims to reconstruct the properties and vigor of the eastern branch of the Nordic Seas overflows over the past 1500 years.
- The material comes from high sedimentation rate, multi and gravity cores, taken on the Gardar Sediment Drift (60°19N, 23°58W, 2081 m water depth). The Gardar Drift accumulates on the eastern flank of the Reykjanes Ridge due to supply of sediments provided by the overlying Iceland-Scotland Overflow Water (ISOW), which is an important component of the North Atlantic Deep Water (NADW).

- Based on ^{210}Pb dating and AMS ^{14}C dates using the planktonic foraminifer species *Neogloboquadrina pachyderma* (dextral), a chronology is established that spans from ~700-2002 AD.
- We reconstruct the changes in near bottom flow vigor of ISOW from the paleocurrent proxy mean sortable silt ($\overline{SS}$), while the bottom water physical and chemical properties are reconstructed using the oxygen and carbon isotopes from the benthonic foraminifer species *Cibicides wuellerstorfi*. In addition, changes in surface hydrography are reconstructed using $\delta^{18}O$ of the planktonic foraminifer species *Neogloboquadrina pachyderma* (dextral), *Globigerina bulloides*, and *Globorotalia inflata*.

2. Did AMOC change in association with the LIA, and are climate fluctuations like the AMO associated with changes in the AMOC?

   We aim specifically to get a better understanding of low frequency climate variations like the LIA and the AMO roles in the AMOC variability over the last 1500 years. Recently, master student Iva Vivoll Johansen completed a complementary study of the integrated Nordic Seas overflow from high resolution sediment cores taken from the Eirik Drift. Together, these two studies, will add to the picture of the variability of the Nordic Seas overflow water over the past ~1500 years, and will provide new insight into the AMOC's role in the climate, which will hopefully give a better foundation for predicting future climate scenarios.

1.2 Background and previous work

1.2.1 Atlantic Meridional Overturning Circulation (AMOC)

Figure 1.1 shows a very simplified sketch of the world's overturning circulation. This circulation pattern is often called Meridional Overturning Circulation (MOC), or Atlantic Meridional Overturning Circulation (AMOC) when referring to the circulation pattern within the Atlantic region. A related term, which is often used as a synonym for the AMOC, is the Thermohaline Circulation (THC). However, the AMOC and the THC are actually different from each other: "*The AMOC is defined as the total (basin-wide) circulation in the latitude depth plane, as typically quantified by a meridional transport streamfunction.*"(Delworth et al., 2008). Thermohaline circulation on the other hand "*…is the part of ocean circulation which is driven by fluxes of heat and freshwater across the sea surface and subsequent mixing of heat and salt…*"(Rahmstorf 2006), hence it is strictly buoyancy driven, while the AMOC

has both THC driven parts and wind driven parts (Delworth et al., 2008). In order to avoid misunderstandings we will use the term AMOC throughout this thesis.

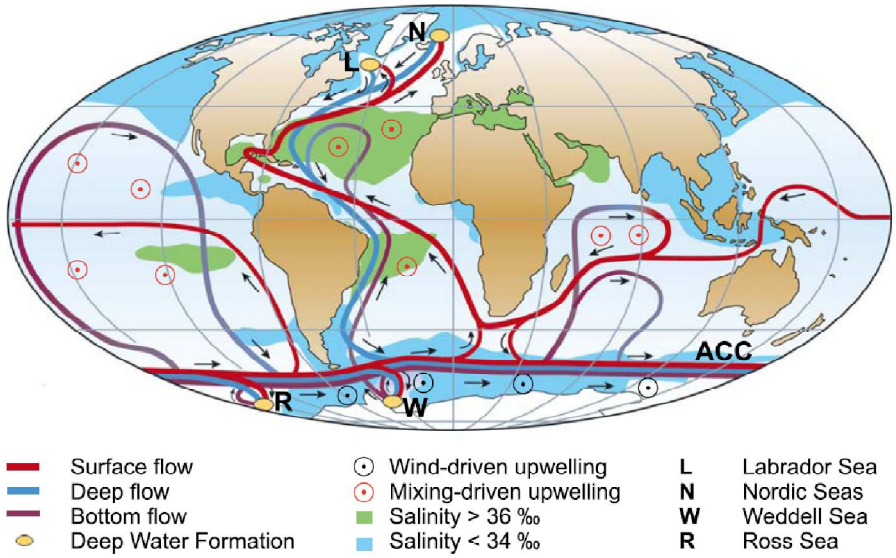

Fig. 1.1: A very simplified sketch of the Earth's global overturning circulation pattern. The circulation pattern seen within the Atlantic region is called the Atlantic Meridional Overturning Circulation. Seen in red are wind induced ocean surface currents which flows in every ocean basin and are connected with each other through the Antarctic Circumpolar Current (ACC). At the southern tip of South Africa, surface currents from the Indian Ocean are joined by surface currents from the ACC, and the Pacific Ocean through the Drake Passage, and flows as a single surface current northward in the South Atlantic. See the text for further description. After Kuhlbrodt (2007).

The AMOC consists of an upper and lower overturning cell, where the upper cell involves the warm top 1000 m of the oceans (Delworth et al., 2008). In the mid-latitudes of the North Atlantic, surface waters are heated by the strong sun overhead, and since evaporation rates exceeds precipitation rates, the surface waters have rather high salinities (Fig. 1.1). Because of the actions of wind and tides these warm and salty surface waters are mixed downward into the deeper layers by diapycnal mixing, causing internal waves in the interior of the ocean, which cause turbulent mixing when they break (Kuhlbrodt et al., 2007). The turbulent mixing of warm surface waters down into the deeper ocean decreases the density of the water present there, causing them to rise (Kuhlbrodt et al., 2007) (Fig. 1.1 & 1.2). The resulting surface and intermediate waters are thereafter transported northwards by the anti-cyclonic subtropical gyre, which has the Gulf Stream and the North Atlantic Current (NAC) as its western boundary current (Talley 1996). The NAC branches into two separate flows, one flows into the Labrador Sea, while the other flows north-east between Iceland and Scotland, and into the Nordic Seas (Fig. 1.1).

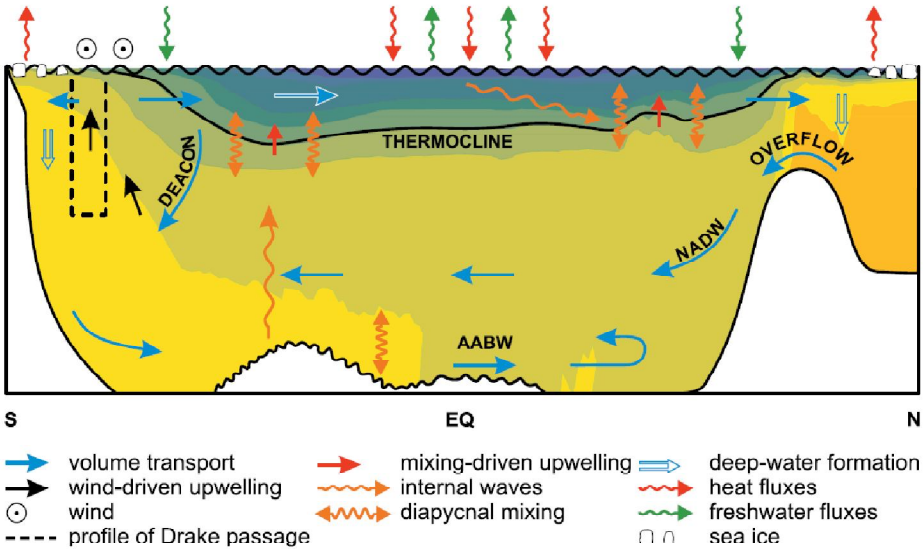

Fig. 1.2: A schematic profile of the Atlantic Basin which shows the AMOC. The blue arrows denote the AMOC, which are described in the text. The color shading illustrates the density differences. Highest density waters are in orange, and lowest in blue. After Kuhlbrodt (2007).

In the Nordic Seas the relative saline NAC looses heat to the surrounding colder waters and the colder atmosphere above, which increases its density. Even though freshwater dilutes the water through precipitation, melting sea-ice, and continental run-off, the water retains enough salinity, and therefore has high enough density to infer sinking when it cools (Hátún et al., 2005). The surface water sinks down to form intermediate and deepwater that overflows the Greenland-Scotland Ridge, on both sides of Iceland, mixes and entrains deepwater formed in a similar manner in the Labrador Sea, and flows back south as North Atlantic Deep Water (NADW) at depths between 1500-4500 m (Delworth et al., 2008). The lower overturning cell consists of Antarctic Bottom Water (AABW) produced in the Weddell Sea in the Antarctic Circumpolar Current (ACC) which flows north into the Atlantic from the ACC at depths below 4500 m, but as it reaches the North Atlantic it gradually rises and becomes mixed with the overlying NADW (Delworth et al., 2008) (Fig. 1.2).

Around Antarctica there is a circumpolar wind system, and due to Ekman transport the surface waters are transported northward, which induces upwelling (Kuhlbrodt et al., 2007). Normally, upwelling causes only shallow and intermediate waters to resurface, but because of the Drake Passage Effect (Rahmstorf 2006) deepwater resurfaces, which in the ACC is mostly inhabited by southward flowing NADW (Kuhlbrodt et al., 2007). Thus, the NADW resurfaces in the ACC and is transported northward by the wind induced surface currents towards the equator, thereby completing the meridional circulation pattern.

The AMOC's climatic impact and changes in its circulation pattern

The AMOC has a profound effect on climate in the North Atlantic region due to the great heat transport associated with it. Heat transport in the North Atlantic Ocean is at its maximum around 30°N were it amounts to ~ 1.3 PW (1 PW = 10^{15} W) (Ganachaud & Wunsch, 2000). The heat comes from the warm surface waters, mainly the Gulf Stream, and according to Rahmstorf (2002) it amounts to a warming of the air above the ocean by up to 10 °C in the North Atlantic, with a declining effect inland over the continents. This great exchange with the atmosphere is apparent even in the high Northern latitudes, were the heat delivered by the Gulf Stream, and its continuation, the NAC, warms the coastal areas around northern Norway making it habitable all year around.

Studies suggest that on several occasions over the last 20 000 years, large amounts of freshwater was released into the North Atlantic deepwater formation sites either by rapid outburst from ice dammed lakes (Broecker et al., 1989; Clarke et al., 2003; Ellison et al., 2006; Kleiven et al., 2008), or from melting icebergs (Delworth et al., 2008). These rapid freshwater perturbations diluted the surface waters and stopped, or greatly reduced, the formation of deepwater (McManus et al., 2004; Ellison et al., 2006; Kleiven et al., 2008), which resulted in reduced northward transport of heat by the surface ocean currents. Thus, it induced a cooling in the North Atlantic region (Andersen et al., 1995; Rahmstorf 2006; Kleiven et al., 2008). From these evidences it is evident that the North Atlantic climate is sensitive to variations in NADW.

Several studies suggest that the strength and pattern of NADW have changed on multiple timescales during both glacial and interglacial periods during the late Quaternary period (Sarnthein et al., 1994; Bianchi & McCave, 1999; Rahmstorf 2002; Oppo et al., 2003; Hall et al., 2004). In the late Holocene period, the North Atlantic region and Europe especially experienced abrupt climate changes on multidecadal to centennial timescales. On centennial timescales the most recent climate changes are the Medieval Warm Period (MWP) and the Little Ice Age (LIA), while on multidecadal timescales the most recent climate changes are the Atlantic Multidecadal Oscillation (AMO) and the North Atlantic Oscillation (NAO). It is of great importance to investigate whether the AMOC plays a role in these abrupt climate changes.

The traditional view of the climate evolution over the last millennium is a warm MWP followed by a cool LIA period which lasted until the late 1800s, when a warming period

started which has continued until today (Nesje & Dahl, 2003). However, recent evidence has shown that this simplistic view is probably not correct(Nesje et al., 2007 and references therein). The MWP, or Medieval Climatic Optimum, is believed to have lasted from 900-1300 AD, and was a period of unusual warmth in Europe and nearby regions (Mann 2002b), with temperatures 0.5-0.8°C warmer than today (Nesje et al., 2005). In this period the climate in large parts of Europe warmed so much that Norse settlers colonized Greenland, and grapes were grown in England, which is impossible today (Mann 2002b). It has been suggested that the MWP was a global phenomenon, but evidence indicate that it involved regional variability, with warmer and cooler periods at different times in different areas (Bradley 1999; Mann 2002b; Jansen et al., 2007).

The LIA is assumed to have lasted from ~1550-1925 AD, and was one of the most severe cooling events in the entire Holocene period (Nesje et al., 2005). However, the timing of the event, and the climatic impact it had is much debated, and it seems to involve both cool and warm periods (Bradley & Jones, 1992; 1993; Bradley 1999; Mann 2002a; Andersson 2003; Nesje & Dahl, 2003; Matthews & Briffa, 2005; Nesje et al., 2005; 2007). Nevertheless, within the time period from ~1550-1925 AD the climate in Europe was at times cooler than today, with great expansions of mountain glaciers in Scandinavia and the European Alps (Grove 1988; Bradley & Jones, 1993; Bradley 1999; Mann 2002a; Nesje & Dahl, 2003; Nesje et al., 2005; 2007).

One of the proposed forcing mechanisms for the MWP and the LIA are changes in the AMOC. Currently, the only evidence suggesting a change in the AMOC linked with the MWP and the LIA comes from studies done on a transect of cores in the Florida Straits. In this, Lund et al. (2006) show that the transport decreased, and surface salinity increased in the Gulf Stream during the LIA, which amounted to, 10 % weaker volume transport in the current compared with modern estimates, thus implying that the reduced heat transport to the North Atlantic contributed to the observed cooling (Fig. 1.3). Lund et al., (2006) also found that the Gulf Stream transport during the Medieval Warm Period (MWP) was of the same order as the modern one. About half of the Gulf Stream is caused by the wind induced subtropical gyre, and the other half is caused by the upper limb of the AMOC, which compensates for the southward flow of NADW (Denton & Broecker, 2008). If the 10 % reduction of the Gulf Stream during the LIA measured by Lund et al. (2006) was caused by a reduction of the AMOC upper limb, Denton & Broecker (2008) argue that it would correspond to a 20 % reduction of the AMOC.

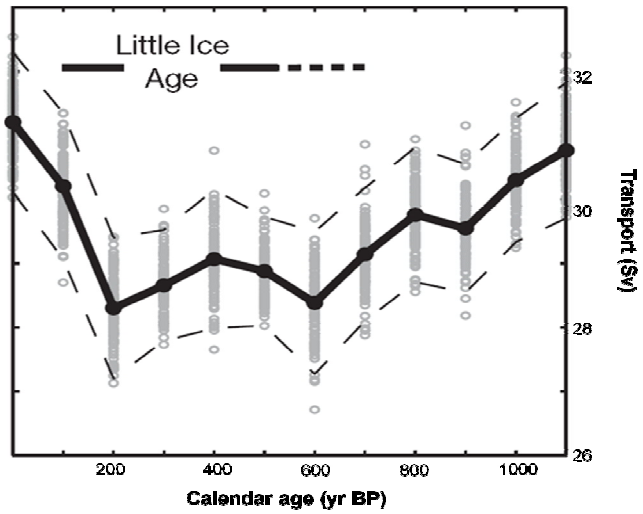

Fig. 1.3: Estimates of total transport in the Gulf Stream from 0-1100 BP. The thick black line is the best estimate for transport variability, while the dotted lines are the 95 % error envelope (±2σ). Modified after Lund et al. (2006).

The findings of Lund et al., (2006) are intriguing. Yet firm conclusions about the AMOC cannot be derived from records of upper ocean transport alone, because the relative contributions of ocean overturning and wind driven circulation changes are impossible to separate in such records. Consequently, reconstructions of the deep overflowing branches (NADW) are required to determine whether such events truly involve changes in ocean overturning.

Low frequency, multidecadal variability in sea-surface temperature (SST) is observed in the North Atlantic Ocean from instrumental records (1856-present) (Gray et al., 2004). This variability has been labeled the Atlantic Multidecadal Oscillation (AMO) (Kerr 2000). The oscillations are quasi-periodic (Knight et al., 2005) and last 65-80 years (temperature range of 0.4 °C) (Gray et al., 2004), with observed cold periods between1905-1925 and 1970-1990 (Enfield et al., 2001), and warm periods between 1860-1880 (Enfield et al., 2001), and 1931-1960 (Sutton & Hodson, 2005). The AMO is a near global climatic oscillation pattern (Knight et al., 2006), but it is most prominent in the North Atlantic Ocean and nearby regions (Enfield et al., 2001). During AMO warm phases most of the United States receive less precipitation (Enfield et al., 2001), while the Caribbean encounters more hurricanes due to the increase of the SST (Goldenberg et al., 2001). Furthermore, the AMO warm phases cause the Inter-Tropical Convergence Zone (ITCZ) to shift northwards, which induces increased summer rainfall over the Caribbean, India, and the Sahel region (Africa) (Knight et al., 2006; Zhang & Delworth, 2006; Delworth et al., 2007). Thus, the AMO seems to modulate the climate over much of the Northern Hemisphere during the last ~150 years. Nevertheless, two full cycles of the AMO are not enough to conclude that it is a consistent climatic pattern in the record;

reconstructions further back in time are therefore needed. Gray et al. (2004) reconstructed the AMO between 1567-1990 AD from tree-ring chronologies gathered from 0-70°N in the Northern Hemisphere (Fig. 1.4) Gray et al. (2004) argue that the AMO has been a consistent climatic feature at least for the past 423 years, and that the reconstructed oscillations (1567-1856 AD) are similar in amplitude to the observed oscillations from instrumental records. Furthermore, their reconstruction over the past ~150 years correlates very well with the observed AMO from instrumental time-series.

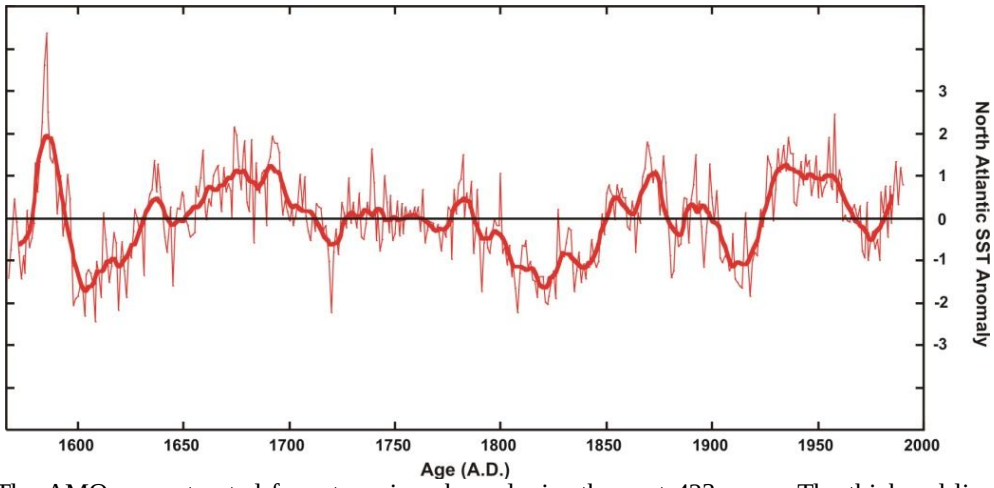

Fig. 1.4: The AMO reconstructed from tree-ring chronologies the past 423 years. The thick red line is the 10 year running mean of the SST variability, while the thin red line is the annual average SST variability. Slightly modified after Gray et al. (2004).

One of the proposed driving mechanisms for the AMO is changes in the AMOC. The scenario is as follows: An enhanced AMOC delivers more heat to the North Atlantic Ocean, thereby increasing the SST (warm AMO mode), but an enhanced AMOC also affects ocean surface currents, hence it eventually slows down the currents that transport saline waters into the deepwater formation sites, which results in less sinking, and reduced northward heat transport, creating a cooling of the SST in the North Atlantic (cool AMO mode) (Kerr 2000; Kerr 2005). Eventually the AMOC will speed up again, because the reduced AMOC allows the salty waters to resume the northward flow into the deepwater formation sites, which enhances sinking and northward heat transport, resulting in that the AMO goes into a warm mode again (Kerr 2000; Kerr 2005).

Presently, the only evidence suggesting a connection between the AMO and the AMOC comes from modeling results. Recent numerical modeling results manage to simulate the observed AMO variability reasonably well, and imply that the AMOC is responsible for, or at least modifies, the AMO pattern (Knight et al., 2005; Sutton & Hodson, 2005; Knight et al.,

2006). However, the different models use different mechanisms to force the simulations (Delworth et al., 2007), which affects their results, and can potentially lead to errors. One way to avoid the shortcomings of model simulations is to reconstruct the variability of the deep overflowing branches from the Nordic Seas (NADW), and look for similar climatic characteristics such as the AMO.

The North Atlantic Oscillation (NAO) is an atmospheric circulation pattern caused by sea-level pressure (SLP) differences between Iceland and Portugal (Hurrell et al., 2003). A high NAO index indicates a lower pressure than normal north of 55°N, and a higher pressure than normal south of 55°N (Hurrell 1995), while a low NAO index is the opposite. During a high NAO index event, the low and high pressure zones create stronger than normal westerly winds (westerlies) towards northern Europe and Scandinavia (Hurrel & van Loon, 1997), which results in warmer and wetter winters than average in much of Northern Europe, Scandinavia, Russia, and central Asia (Hurrell 1995). Due to the presence of the strong high pressure close to Portugal during high NAO index events, southern Europe, the Mediterranean, and northern Africa experience colder and drier winters than average (Hurrell 1995). The NAO does not only modulate winter temperatures and precipitations in the North Atlantic region, but also affects the storminess, ocean heat content and currents (Hurrell et al., 2003), and sea ice extent and transport (Dickson et al., 2000; Lu & Greatbatch, 2002). Thus, the NAO has wide climatic effects. The NAO exhibits inter-annual variability, but on decadal timescales instrumental observations the last ~150 years have shown that there has been high NAO index periods as well as low NAO index periods (Hurrell 2008).

One of the proposed driving mechanisms for the NAO is AMOC variability. Recent measurements of the ISOW flow speed from the Gardar Drift in the Iceland Basin, which is the eastern branch of the Nordic Seas overflow water, show that the flow speed variability is inversely correlated with the NAO index over the last 230 years (Boessenkool et al., 2007b). However, the authors relate this connection to the influence of Labrador Sea water rather than actual changes in the overflow. This is intriguing evidence, but reconstructions further back in time is needed to firmly establish this connection.

Based upon the previous sections, it becomes apparent that the scientific community's understanding of the AMOC role in multidecadal to centennial climate changes is inadequate. This thesis aims to contribute to the current knowledge about the AMOC role in abrupt climate changes by reconstructing the vigor of the eastern branch of the Nordic Seas overflow

water (ISOW) through near bottom flow speed ($\overline{SS}$) reconstructions, while the bottom water physical and chemical properties are reconstructed using the oxygen and carbon isotopes from benthonic foraminifers. We are looking specifically for changes in the overflow that can be related to recent climate variations such as the MWP, LIA, AMO, and NAO.

2 STUDY AREA

The sediment cores used in this study (GS06-144-09 MC-D & GS06144-08 GC) were taken from the Gardar drift (60°19 N, 23°58 W, 2081 m water depth) on the eastern flank of the Reykjanes Ridge in the Iceland Basin. This site is ideally situated to reconstruct changes in the eastern branch of the Nordic Seas overflows (ISOW), and the high sedimentation on the drift rates provides us with high resolution records.

2.1 Geographical setting

The Iceland Basin is separated from the Irminger Basin by the Reykjanes Ridge (RR) to the west, and from the Rockall Channel by the Rockall Plateau to the east, while to the north it is separated from the Arctic Mediterranean by the Greenland-Scotland Ridge (GSR) (Hansen & Østerhus, 2000) (Fig 2.1). The Arctic Mediterranean is a collective name for the Arctic and Nordic Seas, where the Nordic Seas constitute the Barents, Norwegian, Iceland, and Greenland Seas (Hansen & Østerhus, 2000). Another name often used for the Norwegian, Iceland, and Greenland Seas are the GIN Sea (Talley 1996). The Arctic and Nordic Seas are connected through the Fram Strait (Hansen & Østerhus, 2000).

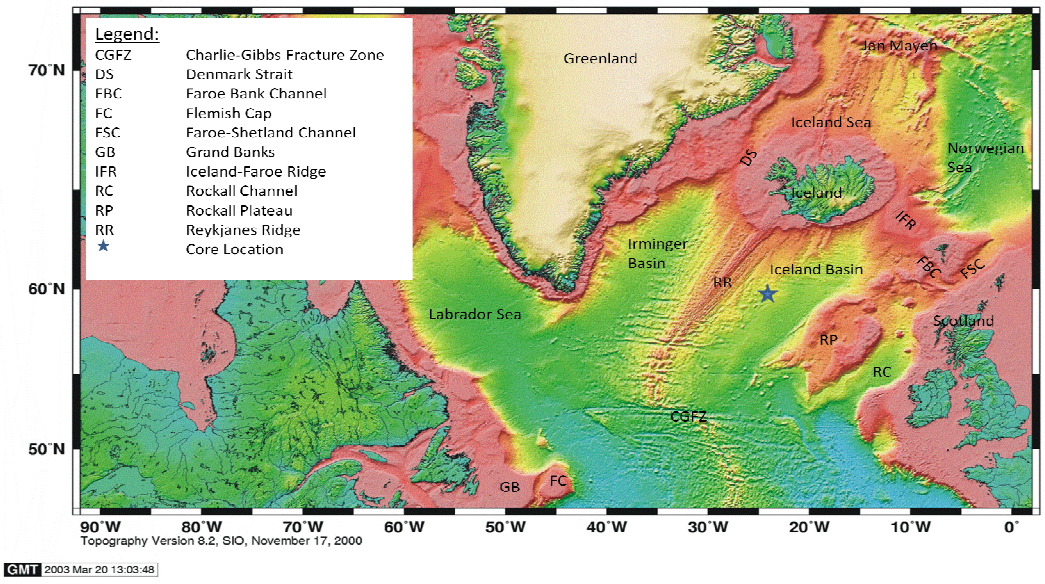

Fig. 2.1: Bathymetric map over the study area and nearby regions. The topographic system connecting Greenland, Iceland, and Scotland is called the Greenland-Scotland Ridge (GSR). Modified after Smith & Sandwell (1997).

2.1.1 The Greenland-Scotland Ridge

The Greenland-Scotland Ridge is not a continuous ridge separating the North Atlantic from the Arctic Mediterranean, but has several shallow sills which allow for water exchange between the basins (Fig. 2.1 & 2.2).

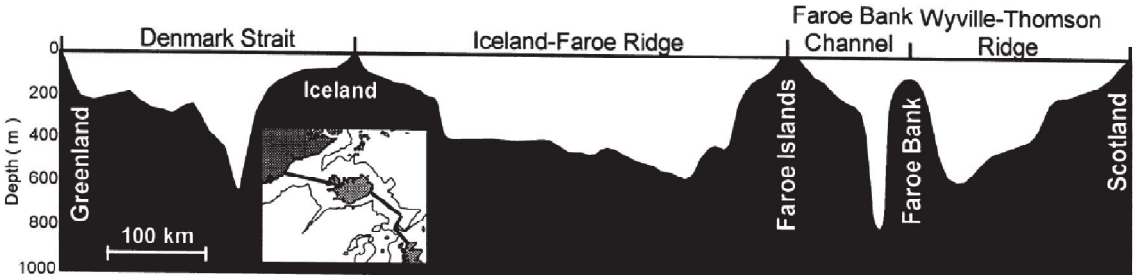

Fig. 2.2: Profile of the Greenland-Scotland Ridge illustrating the different sills. The indicated depths are meters below sea surface. Also shown in the figure is the transect along which the profile is constructed. From Hansen & Østerhus, 2000.

The Denmark Strait between Greenland and Iceland is fairly wide and deepens to the east with a maximum depth of 620 m (Hansen & Østerhus, 2000). East of Iceland, the water exchange between the Nordic Seas and the Iceland Basin occurs mostly via 4 shallow sills along the wide Iceland-Faroe Ridge, ranging from ~420 m depth close to Iceland, and ~480 m depth on the Faroe side (Hansen & Østerhus, 2000). The Faroe-Bank Channel is a narrow, ~850 m deep (Dickson & Brown, 1994) sill between the Faroe Islands and the Faroe Bank (van Aken & Eisma, 1987), whereas the Scotland and Faroe Bank are connected through the ~600 m deep Wyville-Thomson Ridge (Hansen & Østerhus, 2000). North of the Wyville-Thomson Ridge, the Faroe-Shetland Channel (Fig. 2.1) connects the Faroe Islands with Scotland (van Aken & Eisma, 1987), but since this channel is blocked by the Wyville-Thomson Ridge in the southern end, most of the water flowing from the Arctic Mediterranean is forced through the Faroe-Bank Channel on its route to the North Atlantic, while some passes over the Wyville Thomson Ridge (Hansen & Østerhus, 2000).

2.2 Oceanographic setting

The surface and deepwater hydrography in the North Atlantic region is an important part of the AMOC, which is an integrated part of the oceans climate system. Thus, changes in the deepwater overflow across the Greenland-Scotland Ridge, or changes in the heat and volume transport of the North Atlantic Current (NAC), will have profound effects on North Atlantic climate.

2.2.1 Surface hydrography and water masses

The surface circulation pattern in the Nordic Seas is meridional, with inflowing relative warm, saline water transported by the Norwegian Atlantic Current as an eastern boundary current, while the outflow is by the cold, fresh, East Greenland Current which transports a great deal of freshwater from the Arctic regions and into the North Atlantic (Jakobsen et al., 2003). According to Hansen & Østerhus (2000) about ¼ of the inflowing Atlantic water to the Nordic Seas flows out back into the Atlantic through the East Greenland Current, while about ¾ overflows the Greenland-Scotland Ridge.

The North Atlantic subtropical gyre has the Gulf Stream (GS) and North Atlantic Current (NAC) as its western boundary current (Talley 1996). The NAC originates from the warm and relative saline GS and travels north from 40-51°N on the eastern side of the Grand Banks (Rossby 1996), at 52-53°N the NAC flows through a gap in the Mid Atlantic Ridge and turns first east, then northeast across the Atlantic Basin towards Iceland (McCartney & Talley1982; Fratantoni 2001; Jakobsen et al., 2003) (Fig. 2.3 & 2.4). North of 53°N the NAC splits into two branches; one branch flows northwards in the Iceland Basin and bifurcates close to Iceland into the southwest flowing Irminger Current (IC), and the northeast flowing Faroe Current (FC) (Orvik & Niiler, 2002; Jakobsen et al., 2003). The second branch of NAC flows through the Rockall Through along the European continent as the Continental Slope Current (CSC) (Hansen & Østerhus, 2000; Orvik & Niiler, 2002; Jakobsen et al., 2003) (Fig. 2.3 & 2.4). The water mass transported in the IC, FC, and CSC originates from the warm NAC, but by cooling and freshening during wintertime it sinks down between the seasonal thermocline and the permanent pycnocline and forms a water-mass called Subpolar Mode Water (SPMW) (van Aken & Becker, 1996), with a temperature range between 4-14°C (McCartney & Talley, 1982).

Due to the presence of the Reykjanes Ridge most of the Irminger Current flows south parallel to the ridge before finding a passage into the Irminger Basin (McCartney & Talley, 1982), while some also flows over the ridge close to Iceland (Orvik & Niiler, 2002) (Fig. 2.4). When approaching the Denmark Strait the Irminger Current bifurcates (McCartney & Talley, 1982; Hansen & Østerhus, 2000; Orvik & Niiler, 2002; Reverdin et al., 2003) (Fig. 2.3 & 2.4). The smallest flow veers anticyclonically around Iceland as the North Icelandic Irminger Current (NIIC)(Reverdin et al., 2003), transporting relative warm, saline waters to the North Icelandic Shelf (Hansen & Østerhus, 2000), while the rest of the Irminger Current turns cyclonically

south and flows parallel to the East Greenland Current down to Cape Farewell on the southern tip of Greenland (Reverdin et al., 2003) (Fig. 2.3).

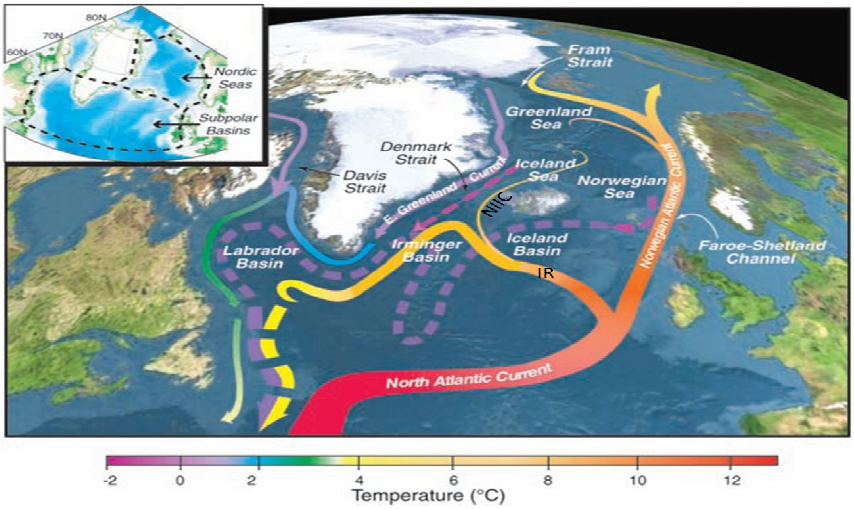

Fig. 2.3: Topographic map over the Nordic Seas and Subpolar Basins showing a simplified version of the main circulation pattern of the northern part of the AMOC. The solid lines indicate surface circulation, while dotted lines indicate the deep overflowing branches from the Nordic Sea. The color scheme indicates different temperatures in the currents. Abbreviations: IR = Irminger Current, NIIC = North Icelandic Irminger Current. The Norwegian Atlantic Current in this map constitutes both the Faroe Current and the Continental Slope Current. See the text for more information about the different currents. Modified after Curry & Mauritzen (2005).

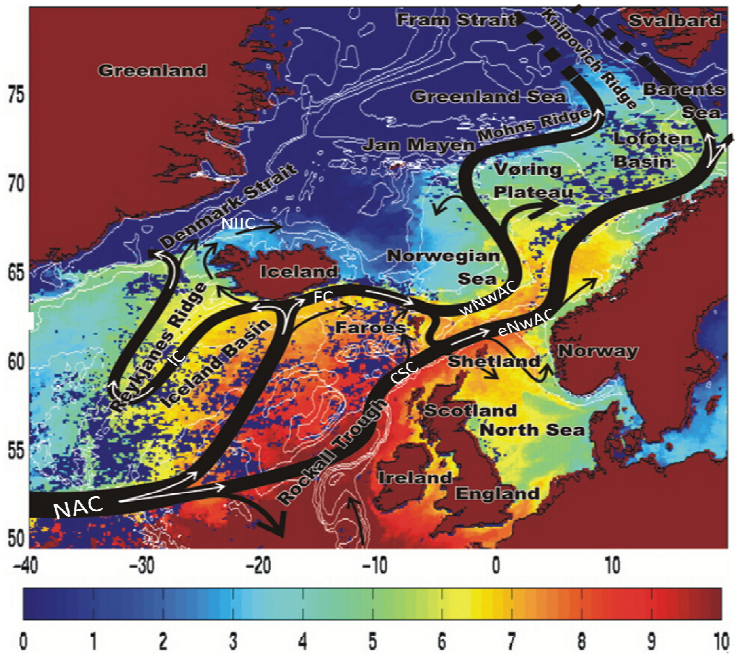

Fig. 2.4: Schematic over the inflowing surface circulation from the North Atlantic to the Arctic Mediterranean. The color scheme indicates sea surface temperature differences, and illustrates the heat transport from the currents to the nearby surface waters. Abbreviations: NAC = North Atlantic Current. IR = Irminger Current. FC = Faroe Current. CSC = Continental Slope Current. NIIC = North Icelandic Irminger Current. eNwAC = eastern Norwegian Atlantic Current. wNwAC = western Norwegian Atlantic Current. Modified after Orvik & Niiler (2002).

When the Faroe Current approaches the Faroe Islands it bifurcates; one branch flows over the Iceland-Faroe Ridge (Fig. 2.4), while the other crosses the Wyville-Thomsen Ridge and flows into the Faroe-Shetland Channel, where it merges with the Continental Slope Current (Hansen & Østerhus, 2000). The western branch of the Faroe Current, which crosses over the Iceland-Faroe Ridge into the Norwegian Sea, is now referred to as the western Norwegian Atlantic Current (Orvik & Niiler, 2002). The Continental Slope Current, which is it is the most saline and warmest current flowing over the GSR into the Nordic Seas (Hansen & Østerhus, 2000), interacts with the eastern branch of the Faroe Current in the Faroe-Shetland Channel, and together flow northeastward as the eastern Norwegian Atlantic Current (Orvik & Niiler, 2002).

2.2.2 Intermediate and deep hydrography and water masses

Most of the deepwater that contribute to the formation of NADW originates in the Nordic Seas from formation of intermediate and deepwater in the Norwegian Sea and Lofoten Basin (Isachsen et al., 2007). The Nordic Seas Intermediate Water (NSIW) and denser Norwegian Sea Deep Water (NSDW) flow towards the Greenland-Scotland Ridge, and overflow on both sides of Iceland (Hunter et al., 2007a). Due to the difference in sill depth along the GSR, NSIW flows through the shallower sills of the Denmark Strait, whereas both NSIW and NSDW overflows through the sills between Iceland and Scotland (Hunter et al., 2007a) (Fig. 2.2). Figure 2.5 shows the deepwater masses and overflowing branches of the northern North Atlantic Ocean.

Iceland-Scotland Overflow Water

Water that overflow the ridges between Iceland and Scotland is referred to as Iceland-Scotland Overflow Water (ISOW), and is more saline than the Denmark Strait Overflow Water (DSOW) because of mixing and entrainment of the overlying warmer and saltier SPMW (NAC origin) (Dickson & Brown, 1994) (Fig. 2.5). There are two main ISOW branches; one through the sills in the Iceland-Faroe Ridge, and one through the Faroe-Shetland Channel. Most of the ISOW flows as a bottom current through the Faroe-Shetland Channel (Dickson & Brown, 1994), where the Coriolis force plasters the current towards the western side of the channel (Faugères et al., 1993). After passing through the channel, most of the water flows northwestward through the Faroe-Bank Channel and into the Iceland Basin, but some also flows over the Wyville-Thomson Ridge (Hansen & Østerhus, 2000). The Wyville-Thomson Ridge overflow water flows through the Rockall Channel on the western side of the Rockall Plateau, interacts with the northward going Antarctic Bottom Water

(AABW) (Fig. 2.5) at the southern end of the Rockall Plateau, where both currents veer to the right due to the Coriolis force, and continue north on the western side of the Rockall Plateau (Wold 1994). Further north in the Iceland Basin the currents join the bottom outflow from the Faroe-Bank Channel (Wold 1994).

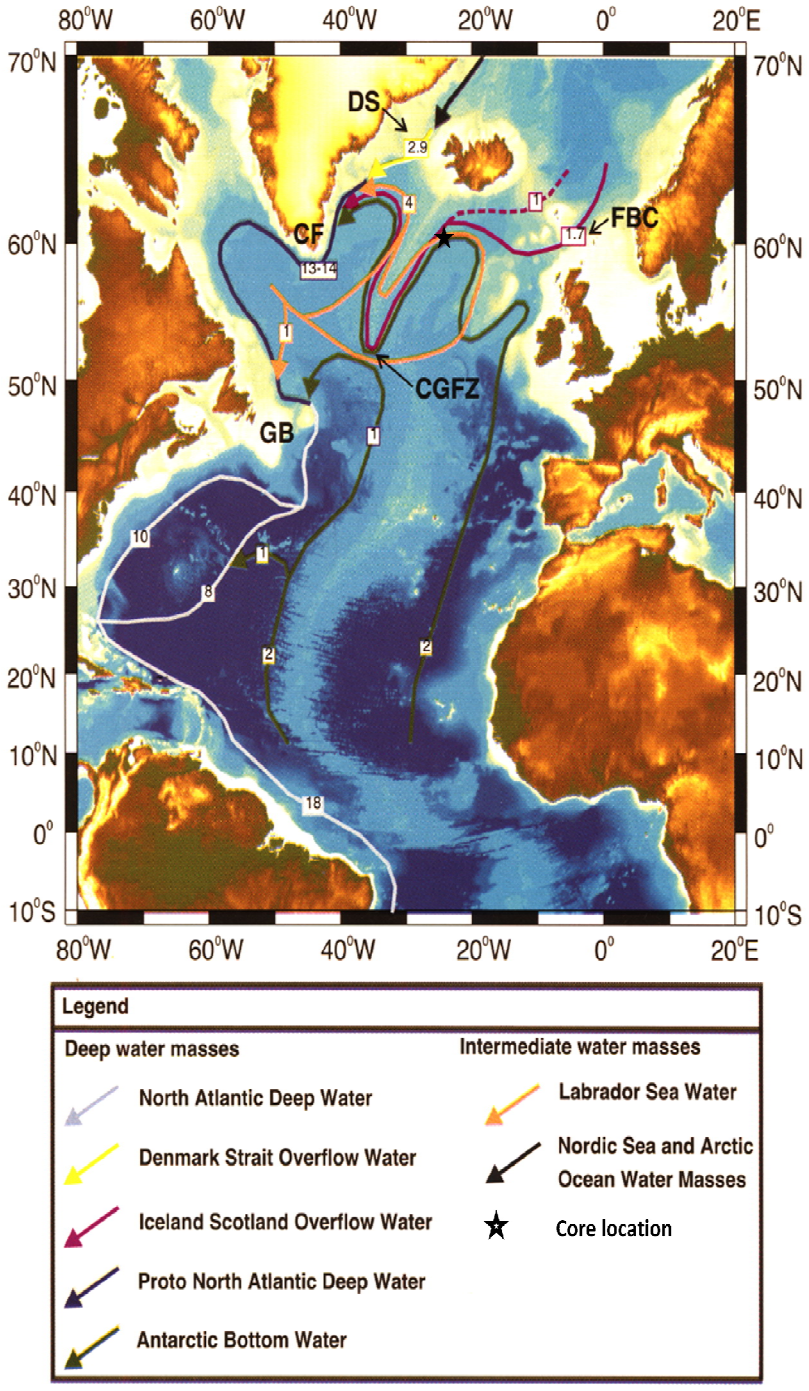

Fig. 2.5: North Atlantic map showing the different deepwater and overflowing branches which ultimately makes up North Atlantic Deep Water. The numbers indicate volume fluxes in Sv. Antarctic Bottom Water (AABW) is referred to as Lower Deep Water (LSW). See text for description of the different water masses. Abbreviations: CF = Cape Farewell, CGFZ = Charlie-Gibbs Fracture Zone, FBC = Faroe Bank Channel, DC = Denmark Strait, GB = Grand Banks. Slightly modified after Hunter et al. (2007b).

The rest of the ISOW exits through the sills in the Iceland-Faroe Ridge, and entrains warm and saline waters from the Faroe Current (SPMW) as it overflows (van Aken & Becker, 1996). Further down the Icelandic slope the current joins with the bottom outflow from the Faroe-Bank Channel, and together flow southwest along the slope of the Reykjanes Ridge. Thus, ISOW is composed of a combination of water from NSIW, NSDW and SPMW, which gives ISOW temperature and salinity characteristics of < 3°C and > 34.94 PSU, respectively (Hansen & Østerhus, 2000). The ISOW continues down into the Icelandic Basin as a deep western boundary current along the eastern slope of the Reykjanes Ridge, while being continuously modified by mixing and entrainment of other less dense water masses (van Aken & Becker, 1996).

Table 2.1 gives the typical watermasses observed in the Iceland Basin, as summarized by Bianchi & McCave (2000). Only SPMW, LSW, and ISOW has significant effect on the modification of ISOW. Labrador Sea Water (LSW) is a intermediate-deep watermass (depth between 1500-2000 m) with low salinity and high oxygen content formed in the Labrador Sea by open ocean convection (Talley 1996). It spreads out from the Labrador Sea into the Irminger and South Iceland Basin where it flows above, but also interacts with, the overflowing waters on either side of Iceland (Dickson & Brown, 1994) (Fig. 2.5). Lower Deep Water (LDW) is observed in the southern Icelandic Basin and in the southern Rockall Channel as watermass underlying the LSW, with relative high amounts of AABW (van Aken & Becker, 1996). LDW is today known as modified AABW (McCartney 1992) (shown as AABW in Fig. 2.5).

Table 2.1: Typical characteristics for the watermasses observed in the Iceland Basin. [a] Characteristics near the Iceland-Faroe Ridge and Faroe Bank Channel sills. [b] Characteristics at 54°N in the Maury Channel. Abbreviations: SPMW = Subpolar Mode Water, IW = Intermediate Water, LSW = Labrador Sea Water, ISW = Icelandic Slope Water, LDW = Lower Deep Water, ISOW = Iceland-Scotland Overflow Water. After Bianchi & McCave (2000)

Watermass	θ (°C)	Salinity (PSU)	O_2 (μmol^{kg-1})	Si (μmol^{kg-1})	NO_3 (μmol^{kg-1})
SPMW[a]	8.00	35.23	270	6.3	15.0
IW	6.00	35.05	230	12.0	18.0
LSW	3.40	34.885	> 275	10.5	17.5
ISW	4.00	34.97-34.99	-	-	-
LDW[b]	2.24	34.94	240	33.0	22.0
ISOW	1.75	35.00	285	7.5	14.5

At depths around 1200 m LSW is incorporated into ISOW, and the combined current continues south towards the northern end of the Maury Channel where LDW is incorporated (Bianchi & McCave, 2000). The combined current, now referred to as North-East Atlantic Deep Water (NEADW), continues south along the eastern flank of the Reykjanes Ridge down to 52°N, where the Coriolis force veers the current to the west through the CGFZ, and north into the Irminger Basin along the western flank of the Reykjanes Ridge (Wold 1994). However, a small part of the current continues west (Wold 1994), while some even continues south along the eastern side of the Mid Atlantic Ridge (Hansen & Østerhus, 2000). In the Irminger Basin the current is now referred to as North-West Atlantic Deep Water (NWADW), and it continues northwest towards the Denmark Strait, where it interacts and mixes with overflow from the Denmark Strait (Wold 1994).

Denmark-Strait Overflow Water

The Denmark Strait Overflow Water (DSOW) is denser than ISOW, due to colder temperatures when it overflows, and it preserves its salinity characteristics because of the small salinity difference between the overlying EGC and the underlying LSW (Dickson & Brown, 1994). When it overflows it entrains water from the LSW, which has a large impact on its properties (Dickson & Brown, 1994).

NADW formation and volume flux

South of the Denmark Strait the northward flowing NWADW is entrained into the southward flowing DSOW, and the combined flow, now referred to as Deep Western Boundary Current (DWBC) (Hunter el al., 2007a), continues south. Due to entrainment of LSW the combined flow of NWADW and DSOW is so strong that it scours the base of the East Greenland slope on its way south (Wold 1994). When the current reaches the southern tip of Greenland the Coriolis force veers it into the Labrador Sea along the western Greenland margin, where the current changes direction, entrains water from the LSW, and continues south as NADW (Wold 1994).

The best estimates for the volume flux of the different branches that make up NADW comes from Schmitz & McCartney (1993), and Dickson & Brown (1994). Dickson & Brown found the total ISOW outflow to be 2.7 Sv, where 1.7 Sv flows out through Faroe Bank Channel, while the remaining 1 Sv flows out through the different sills in the Iceland-Faroe Ridge. Over the Wyville-Thomson Ridge they only found 0.3 Sv, which is not included in 2.7 Sv total outflow. The flow of NEADW through the CGFZ is very uncertain and much debated

(Hansen & Østerhus, 2000, and references therein). Hansen & Østerhus (2000) found the best estimates through the CGFZ only to be 1.2 Sv, which is even less than the ISOW outflow when entrainment of LSW and LDW is not included. However, as Hansen & Østerhus (2000) points out, the NEADW probably flows over the Reykjanes Ridge and into Irminger Basin at other locations further north, hence there is reason to believe that most of the NEADW reaches the Irminger Basin and contribute to the total southward export of NADW. Dickson & Brown (1994) found DSOW to contribute 2.9 Sv to the DWBC, while LSW was found to contribute 4 Sv to the DWBC when reaching Cape Farewell. According to Schmitz & McCartney (1993) LDW contributes 4 Sv to the DWBC, where 2 Sv are entrained around Cape Farewell, and the rest further south along the DWBW path. When combining these branches the flow of DWBC at Cape Farewell amounts to 13.3 Sv (Dickson & Brown, 1994).

From these estimates ISOW is assumed to contribute about half of the Nordic Seas overflow water. Therefore it is an important branch of the total southward flowing NADW.

2.3 Sediment Drifts

The bottom currents overflowing the Greenland-Scotland Ridge have a profound effect on the sediment distribution in the subpolar basins, and have resulted in the construction of several sediment drifts (Miller & Tucholke, 1983). As defined by Stow et al. (2002):

"*Sediment drift is a general term for a sediment accumulation, of no definitive or unique geometry, that has experienced some current control on deposition. It is not restricted to bottom current deposits. Contourite drift is the specific term for a sediment drift that has been formed principally (though not necessarily exclusively) by bottom currents.*"

The circulation pattern of deep ocean currents has resulted in development of 7 major contourite drifts in the subpolar basins, which all are defined as giant elongate drifts (Wold 1994; Faugères et al., 1999) (Fig. 2.6). Giant elongate drifts are huge sediment bodies draped over the topography, that are oriented parallel to the current which has deposited them (Faugères et al., 1993). They develop an elongate geometry due to topographic barriers like mid ocean ridges, which constrain them, and force the sediments to be deposited parallel to the ridge (Faugères et al., 1993). Sediment focusing into drifts is caused by a sediment laden water mass called the nepheloid layer (Wold 1994), which is defined by the American Geological Institutes Glossary of Geology online as "*… A layer of water in the deep ocean*

basin that contains significant amounts of suspended sediment. It is from 200 m to 1,000 m thick."

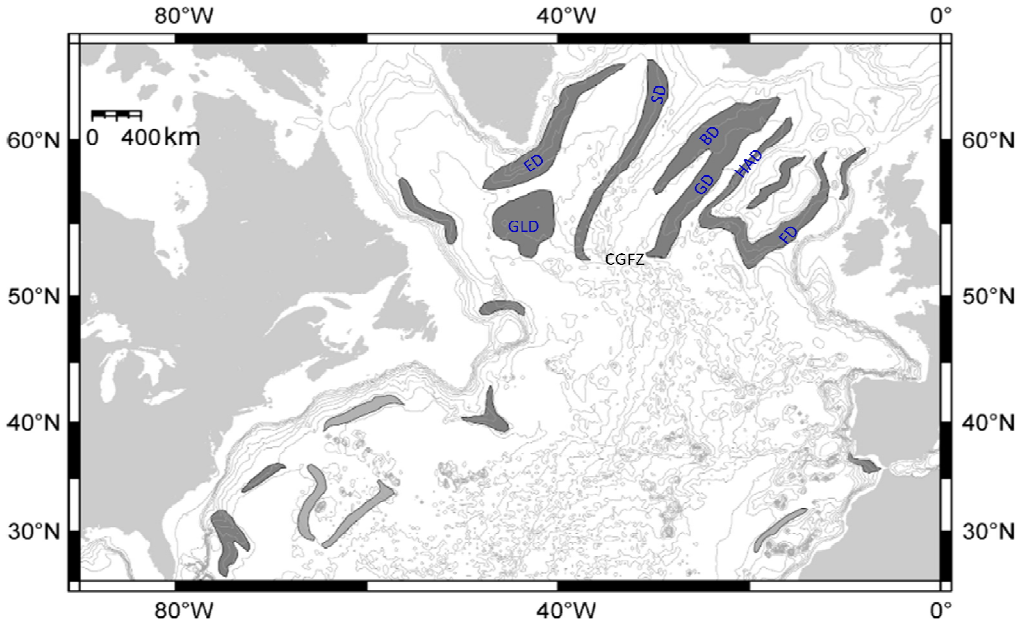

Fig. 2.6: Map over the North Atlantic showing the distribution of contourite drifts. Notice that the drifts orientation and distribution closely resembles the bottom circulation described in chapter 3.2. Abbreviations: BD = Bjørn Drift, CGFZ = Charlie-Gibbs Fracture Zone, ED = Eirik Drift, FD = Feni Drift, GD = Gardar Drift, GLD = Gloria Drift, HAD = Hatton Drift, SD = Snorri Drift. Modified after Faugères et al. (1999).

2.3.1 The Gardar Drift

The Bjørn and Gardar Drift accumulate on the eastern slope of the Reykjanes Ridge (Wold 1994) (Fig. 2.7). Bjørn Drift accumulates on the highest part of the ridge at depths averaging 1800 m, while the Gardar Drift is accumulating further south (Wold 1994). Both drifts have crests, and the crest of the Gardar Drift stretches for more than 1100 km beginning at ~1400 m water depth in the northeast end, and ending in the southwest end near the CGFZ at depths below 3000 m (Bianchi & McCave, 2000). As Fig. 2.7 indicates, the Gardar Drift is not a continuous drift, but rather consists of two main parts. Nevertheless it is the second largest drift of the 7 seen in Fig. 2.7 , and amounts to 201 x 10^{18} g of sediment (Wold 1994).

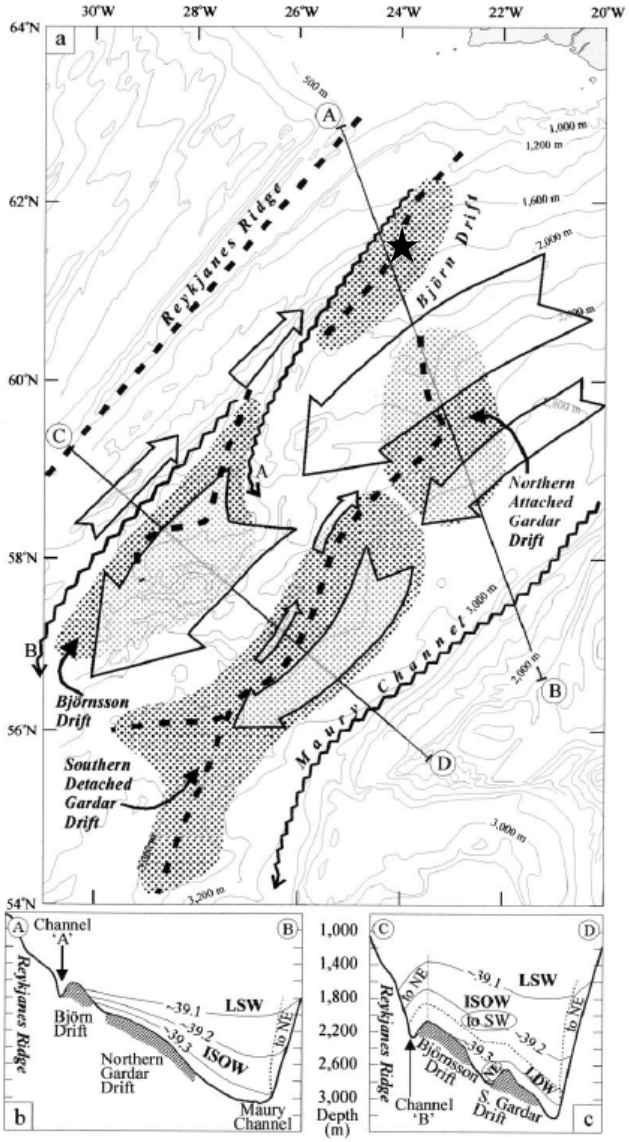

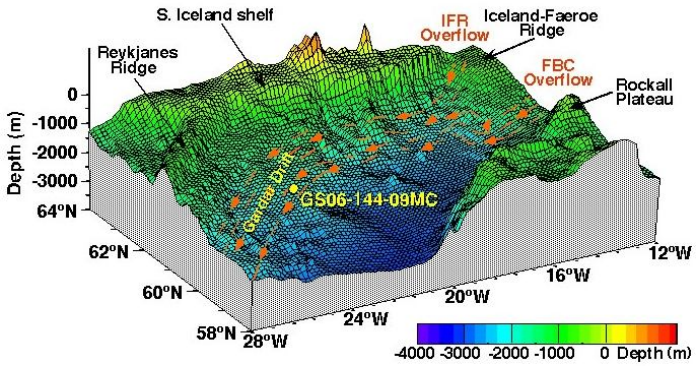

Fig. 2.8: Graphic illustration of the Gardar Drift on the eastern flank of the Reykjanes Ridge. The orange arrows indicate the ISOW current which overflows from the Iceland-Faroe Ridge (IFR) and through the Faroe Bank Chanel (FBC). The yellow dot indicates the core sites.

Fig. 2.7: Bathymetric map over the Iceland Basin showing the geographical extent of the Bjørn, Bjørnsson, and Gardar Drift. Arrows indicate the ISOW flow, where bigger arrows indicate stronger currents. The black star indicates the core sites. Modified after Bianchi & McCave (2000).

The Gardar Drift was first discovered by Johnson & Schneider (1969), and was initially named the Gardar Ridge because of its crest, but was later renamed to the Gardar Drift by Ruddiman (1972) since it is an accumulation of sediments, and not a tectonic feature. As early as 1969 it was already believed to be caused by bottom currents overflowing the Iceland-Scotland Ridge (Johnson & Schneider, 1969). The Gardar drift started accumulating in late Eocene or early Oligocene (Ruddiman 1972; Kidd & Hill, 1987; Wold 1994), when ISOW started flowing over the Iceland-Faroe Ridge and through the Faroe-Bank Channel (Wold 1994). On the Gardar Drift, Pliocene to Holocene sediment packages is much greater than the older sediment deposits, because of erosion of older sediments by the bottom currents and deposition on the drift site (Wold 1994), which explains why the sediment mass on the Gardar Drift is so great. Much of the sediments that are deposited on the Gardar Drift are eroded terrigenous material from the Iceland-Faroe Ridge (Wold 1994).

Figure 2.7 & 2.8 illustrates that the cores used in this study are situated within the main path of the ISOW flow over the Gardar Drift. The profile A-B across the Bjørn Drift and northern

Gardar Drift in Fig. 2.7 shows the watermasses that interact with the Bjørn and Gardar Drifts. According to Bianchi & McCave (2000), there is no indication that LSW interacts with the sedimentation on the northern Gardar Drift, hence, only ISOW has a direct effect on the core site sedimentation. Bianchi & McCave (2000) found from sortable silt mean grain-size measurements that only the drift sites below 1600 m were significantly affected by bottom currents. Furthermore, they found that the core of the ISOW flows at water depths between 2000-2600 m. The cores were gathered at 2081 m below sea-level, and are thus within the main path of the ISOW core flow. In addition, Bianchi & McCave (2000) found Holocene sedimentation rates as high as 21 cm ka^{-1} in the area around core sites, indicating a vigorous ISOW current throughout the Holocene period. Based on these findings, it becomes evident that the study site is ideally located to perform high-resolution reconstructions of the ISOW vigor during the late Holocene period.

3 MATERIALS AND METHODS

3.1 Cores GS06-144-09 MC-D and GS06-144-08 GC

The marine sediments used in this study comes from a multicore (GS06-144-09 MC-D) and a gravity-core (GS06-144-08 GC) taken during the UoB Cruise No: GS06-144, onboard the research vessel R/V *G.O. Sars*, which is jointly owned by the Institute of Marine Research (IMR) and the University of Bergen (UoB). The cruise took place in the North Atlantic from 20 June to 9 July 2006, and its objectives were to collect marine sediments and water samples from the Eirik Drift south of Greenland, Reykjanes Ridge, and Gardar Drift south of Iceland (Fig. 3.1).

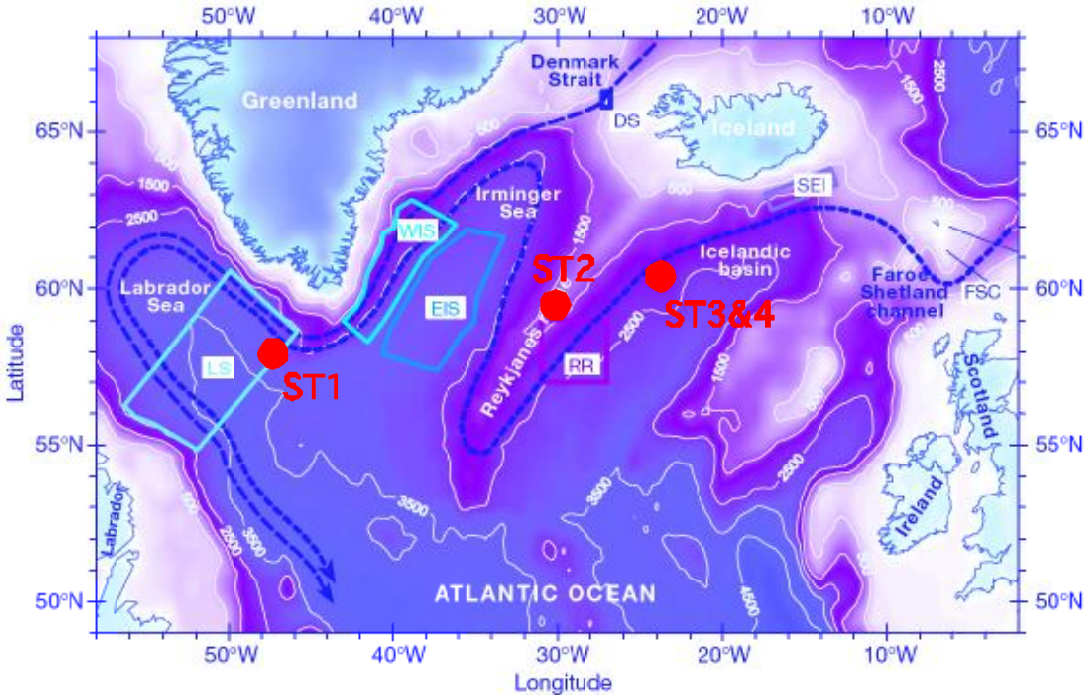

Fig. 3.1: Bathymetric map of the 4 different coring stations during the UoB/BCCR Cruise No: GS06-144. Both cores where collected at station ST4. From Ninnemann et al. (2006), modified after Dickson et al. (2002).

Station ST4 was located at 60°19.18 N, 23°58.00 W on the Gardar Sediment Drift, which is situated on the eastern flank of the Reykjanes Ridge. Both cores where collected at this position, at 2081 m water depth. Gravity core GS06-144-08 GC successfully recovered 5 m of marine sediments, but with a slight over-penetration. However, the brown surface layer seen in the multi-core (GS06-144-09 MC A-D) was present in the barrelhead, thus limiting the over-penetration to more or less 15 cm (Ninnemann et al., 2006). The gravity core was split

into 4 sections, A-D, where D is the top. Part D was 142.6 cm long, and in this study the first 64 cm it is used.

The objectives for the multicore operation at this site was to recover high resolution cores from the top 50 cm of sediment package, thus ensuring possible correlation between the top and instrumental time series. The multi-core operation was successful, and all 4 tubes came up completely filled with undisturbed sediments (GS06-144-09 MC A-D), with a clear sediment-water interface in all 4 tubes (Ninnemann et al., 2006) (Fig. 3.2). In this study GS06-144-09 MC-D is used, which recovered 44.5 cm of undisturbed marine sediments.

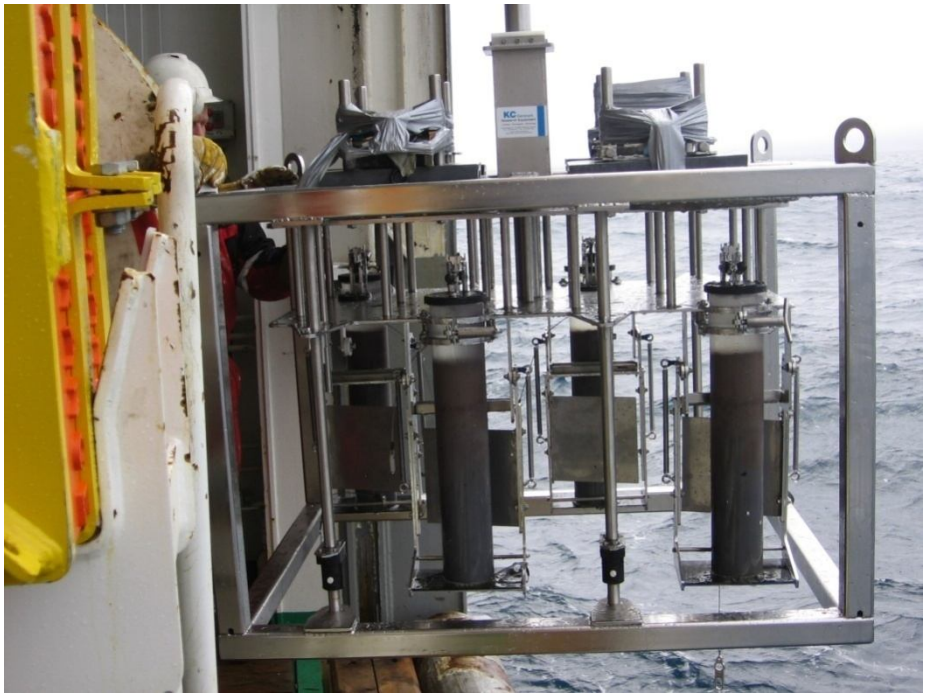

Fig. 3.2: Picture of the GS06-144-09 MC A-D core coming up after a successful multi-core operation. Photo by Ulysses S. Ninnemann.

3.1.1 Core description

GS06-144-09 MC-D and GS-144-08 GC

Visual examination of the multicore shows that it is homogeneous and well sorted throughout the record, and consist mainly of silty clay with abundant planktonic foraminifera, and some benthonic foraminifera. The top 5.5 cm of the core has a light-medium brown color that abruptly changes into a narrow, undulating, dark brown layer that is only ~ 1.5 cm wide (from 5.5-7 cm) (Fig. 3.3). After 7 cm the color shifts back to light brown, which gradually changes

into light gray. At around 10 cm the color is almost purely light gray, with a few brownish patches. From 10-44.5 cm the core remains gray in color, but becomes progressively darker down-core. Visible throughout the core are some small holes which are markings after burrowing animals.

Physical characteristics measured in the cores are density, and magnetic susceptibility (Fig. 3.3). The density at the top of the multicore is ~ 1g/cc, and it increases gradually without any significant excursion until ~ 22 cm down-core, where it reaches 1.2 g/cc. At 22 cm there is a sudden decrease in density of 0.17 in only 1 cm, considering that the variability of the whole core is only 0.4, this is fairly large. It is also the largest excursion throughout the density record. After 23 cm the density steadily decreases down to ~ 33 cm, where it reaches a minimum. From 33-44.5 cm the density increases gradually, but with a steeper gradient than previously in the core. It reaches a core maximum of 1.4 g/cc at around 43 cm. Nevertheless, when looking at the core as a whole, despite the subtle variances, there seems to be a long term trend toward higher density throughout the core. Such a development is expected since continuously burial of sediments increases compaction and density down-core. Water has the density of approximately 1g/cc, while marine sediments usually have higher densities, hence the density scale used in the density record cannot be correct. However, the record still gives valuable information, but rather than expressing absolute density variations, it expresses relative variations.

The magnetic susceptibility shows a similar long term trend with gradually higher values down-core. At the core top it has a value of 100 SI, and about 170 SI at the end. The curve shows multiple small excursions throughout the record and the largest excursion coincide with the sudden drop seen in the density curve, but unlike the density, the magnetic susceptibility recovers after the sudden drop in value. Furthermore, the magnetic susceptibility shows a similar trend as the density between 23-44.5 cm, with a decrease in value towards 33 cm, and an increase afterwards.

The brown band described in the visual examination (between 5.5 and 7 cm in the core) is not expressed in the density, or the magnetic susceptibility record. However, the excursion at ~ 22 cm, expressed in both the density and magnetic susceptibility records, coincide with a burrow marking; hence it is not a physical characteristic of the core. To summarize, the visual core appearance changes does not correspond well with the changes in the physical characteristics.

Core GS-06-144-08 GC overlaps about 15 cm with the bottom of the multicore, and shows similar visual and physical characteristics down-core. Visual examination shows that it is homogenous and well sorted, and consist mainly of silty clay with abundant planktonic foraminifers and some benthonic. The color is gray, and becomes progressively darker down-core. From the physical characteristics it is noted that the density increases steadily down-core without significant excursions, while the magnetic susceptibility shows relatively small excursion around the mean value of 135 SI.

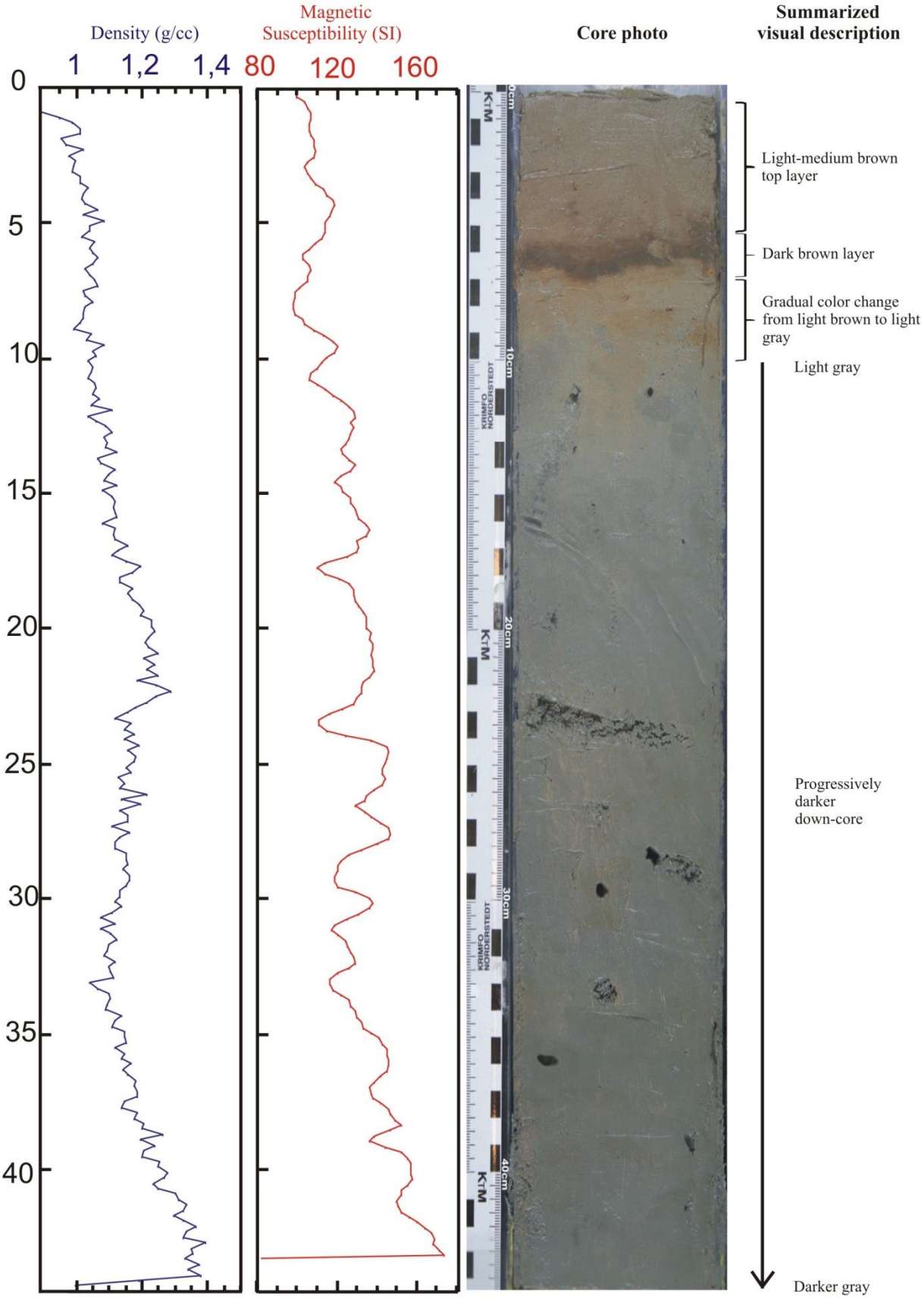

Fig. 3.3: Summary of the visual and physical characteristics of core GS06-144-09 MC-D

3.2 Laboratory methods

The isotopic measurements were carried out at the Geological Mass Spectrometry (GMS) laboratory at the Bjerknes Centre for Climate Research (BCCR), while the sedimentological preparations of the cores where carried out at the sedimentary laboratory of the Department of Earth Science, University of Bergen (UoB). The sortable silt mean grain-size measurements were carried out at the sedimentological laboratory at Cardiff University, Wales, UK, under the supervision of Dr. Ian Hall.

While working with cores (washing, sampling, etc.) it is crucial that proper and accurate handling of the cores is undertaken throughout the different operations, thereby limiting the sources of error.

3.2.1 Sample preparation

Prior to the measurements, the cores were carefully prepared and analyzed. The cores were split longitudinal into two halves, a working half, and an archive half. The archive half was digitally photographed, x-ray photographed, and scanned through a Multi Sensor Track (MST) device that measures, amongst other physical characteristics, bulk density and magnetic susceptibility (see Fig. 3.3), while visual characteristics were examined on the working half. Both halves of the multicore were sampled at intervals of 0.5 cm (0-44.5 cm). The archive half were sent to the Gamma Dating Center in Copenhagen for ^{210}PB dating, while wet and dry weights were measured on the working half. From the gravity core, only the working half was sampled, at intervals of 1 cm (0-142.6 cm). Thereafter, the samples from the working half of both cores were soaked in distilled water and shaken for 12- 24 hours in order to disperse the sediments. Afterwards, the samples were wet-sieved into fractions of > 150 μm, > 63 μm, and < 63 μm. Finally, the samples were placed in a drying cabinet (~55°C) until all the water had evaporated, and then transferred to sampling glasses.

3.2.2 Preparations for sortable silt mean grain-size measurements[1]

The sortable silt mean grain-size method was only applied to the multicore samples. The method is based upon measuring the grain-size variability in the 10-63 μm terrigenous fraction; hence, carbonates and silicates was removed from the samples prior to the analyses.

[1] The de-carbonation and de-silication procedure was received from Dr. Ian Hall, Cardiff University, Wales, UK.

Since only the 10-63 µm fractions of the samples is used, only samples from the < 63 µm were prepared. Prior to the de-carbonation and de-silication processes, the dry samples were crushed using a mortar to ensure a uniform grain-size distribution. To ensure reliable results, 2.5 gram of sediments from each sample was used in the preparations.

De-carbonation

300-350 ml of 1M acetic acid (vinegar) was added to the samples in 400 ml jars while stirring the solution vigorously. Next, the jars were placed in fume cupboards for 24 hours, or until the sediment had settled. After the sediments had settled the supernatant were removed, and the process repeated.

De-silication

The supernatant (acetic acid) were removed and the sediments transferred into conical flasks using a Sodium Carbonate solution filled squirt bottle. 100 ml of 2M Sodium Carbonate (Na_2CO_3) was added to the sediment in the conical flasks, and mixed well. Thereafter, the flasks were transferred to water baths pre-heated to 85 °C for 2 hours. After 2 hours, the flasks were mixed vigorously to re-suspend the sediment while in the bath, and left to stand for another 2 hours. After the additional 2 hours the mixing was repeated, and the flasks were left to stand one last hour in the water bath. The samples were then removed from the bath, and the supernatant extracted when the sediment had settled. Thereafter, the samples were rinsed with de-ionized water, left to settle, and then rinsed once more. Finally, the sediments were transferred into 60 ml nalgene bottles (using a squirt bottle filled with calgon solution), and 50 ml of 2M calgon solution was added. The samples were then stored in cold and dark conditions ready for analyses.

Sortable silt mean grain-size measurements using a Coulter Counter

Prior to the analyses in the Coulter Counter, the nalgene bottles were inserted onto a spinning wheel for 24 hours, to ensure complete disaggregation. The samples were also transferred to an ultrasonic bath for 3 minutes to further disperse the sediments. Finally, 250 ml of sediment, collected precisely at the same depth in the bottles, were transferred into a specialized beaker filled with an electrolysis solution, and inserted into the Coulter Counter.

Every sample was measured in triplicates in order to get a good reproducibility of the sortable silt variability. The first run was used for training, in order to acquire a consistent sampling

method (not used). The two consecutive runs were successful, and showed a high degree of reproducibility. In this study, the presented sortable silt mean grain-size measurements comes from the two last runs.

3.2.3 Picking and selection of foraminifers[2]

All foraminifers used for the stable isotope studies were picked from the > 150 μm fraction. Three planktonic, and one benthonic species were used: *Globigerina bulloides* (hereinafter *G. bulloides*), *Neogloboquadrina pachyderma* (dextral) [hereinafter *N. pachyderma* (d)], *Globorotalia inflata* (hereinafter *G. inflata*), and *Cibicides wuellerstorfi* (hereinafter *C. wuellerstorfi*), respectively. For all species, whole and visually clean specimens were preferred. *G. bulloides* is known to show variability in isotopic values due to differences in the size of the shells (ontogenic effects) (Spero & Lea, 1996; Naidu & Niitsuma, 2004). Thus, to minimize this effect the species was picked only from the 300-250 μm size interval. For the same reason *N. pachyderma* (d) was picked in the 250-150 μm size fraction, and *G. inflata* in the 350-250 μm size fraction. *C. wuellerstorfi* is not known to have ontogenic effects (Wefer & Berger, 1991), and since its abundance in the cores where sparse, every individual were picked. About 40 specimens of *N. pachyderma* (d) and 20 specimens of *G. bulloides* and *G. inflata* were picked for the isotopic studies.

3.2.4 Removal of contaminants

There may be fragments of organic detritus and other contaminants attached to the foraminifer shells, which could potentially affect the isotopic signal. Therefore, contaminants where removed prior to the isotopic measurements. First, the foraminifers were inserted into glass vials and carefully covered with methanol using a pipette. The methanol was added very slowly to ensure that the foraminifers remained in the bottom of the glass vials, and did not float. Secondly, the glass vials was inserted into an ultrasonic bath for 3-7 seconds, depending on the thickness of the shell. The ultrasonic bath removes clay particles and other detritus from the surface of the shells. Thirdly, the methanol was carefully removed using a syringe, and the glass vials were inserted into a drying cabinet at 50 °C, to evaporate the reminder of the methanol. *N. pachyderma* (d) had very thin shells, hence some of them shattered while in the ultrasonic bath. Thus, extra precaution were needed when the methanol was removed in order to hinder that some of the shell fragments was removed with the methanol. Luckily, the

[2] For more information on the different foraminifer species used in this study see chapter 3.4.

shell fragments were large enough that they did not float, and instead gathered at the bottom of the vials. Thus, the loss of shell fragments was minimal.

3.2.5 Mass spectrometer

The GMS lab at Bjerknes Centre for Climate Research has two Nier type dual inlet gas source Isotope Ratio Mass Spectrometers (IRMS), devised to analyses of carbonates; a Finnegan MAT 251, and a MAT 253. All samples of *N. pachyderma* (d), *G. inflata,* and *C. wuellerstorfi* were measured on the Finnegan MAT 253, while *G. bulloides* was measured on Finnegan MAT 253 from 0-19 cm and 40-44.5 cm, and on MAT 251 from 19-40 cm. The MAT 253 has the ability of measuring smaller samples than MAT 251, thus, the MAT 253 was the best choice for measuring *C. wuellerstorfi* since its abundance were low in the cores, and the shells were small. The samples of *G. bulloides* were measured on the MAT 251 in the interval 19-40 cm because the 253 suffered from some problems at the time. The following mass spectrometer analytical procedure will be explained in reference to the MAT 253, but the same procedure also applies to the MAT 251.

Figure 3.4 shows a schematic of a typical modern gas mass spectrometer. There are two inlet sites for gas, one for the sample measured, and one for the reference (standard) gas. Bellows are connected to the inlet system, which are compressed, or expanded, to ensure that the standard and sample gas have the same pressure. The gas flows through a capillary which is fastened to the switching block by a crimp. The function of the crimped capillary is that it reduces the amount of gas that reach the mass spectrometer, and assures viscous flow (Sharp 2007). Viscous flow, rather than molecular flow, is needed to ensure that isotopic fractionation does not occur in the capillary. With molecular flow the lighter isotopes acquire a higher velocity than the heavier ones, and will reach the mass spectrometer first, causing a fractionation that will bias the isotopic signal. At the switching block, rapid switching between the standard and the sample enable the machine to measure the isotopic ratio of both under almost identical conditions, thus eliminating noise caused by electronic instability and other factors (Sharp 2007). After leaving the switching block the gas flows into the ion source where it is bombarded with electrons from a filament that is heated to high temperatures (Sharp 2007). The electron beam strips off the outer electrons of the isotopes, and creates positively charged ions. In the ion source region there is set up a high voltage potential which accelerates the positively charges ions, and by a series of electrical lenses, the accelerated ions are concentrated into a single beam, which is passed through a strong magnetic field (Sharp

2007). The magnetic field deflects the positively charged ions into circular trajectory, were the amount of deflection is controlled by the mass of the isotope. Lighter isotopes are deflected more strongly than heavier ones. The deflected ions are then collected by multiple Faraday cups at the same time, and the difference between the isotopic ratio of the standard and the isotopic ratio of the sample (the δ) is calculated.

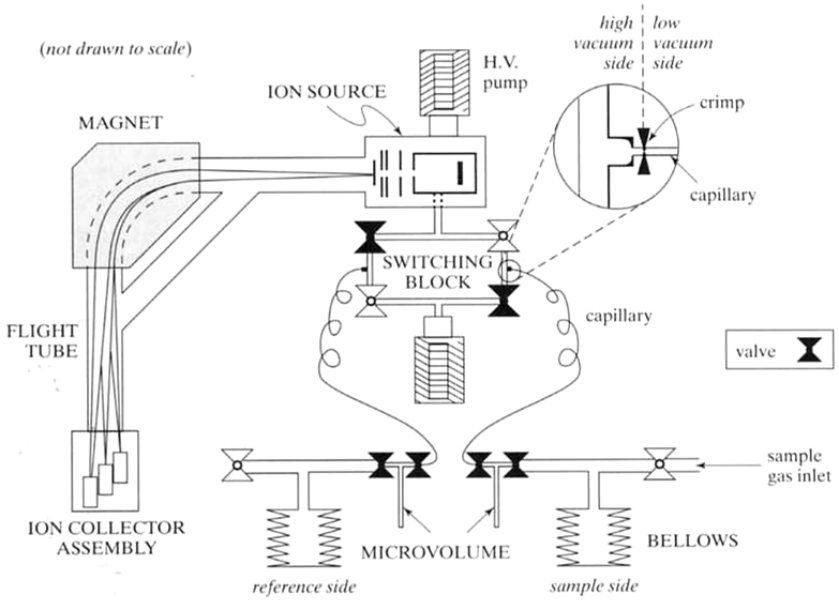

Fig. 3.4: Schematic of a typical modern mass spectrometer. See the text for the operational procedure. Modified after Sharp (2007).

There are three ion beams of CO_2 that reaches the Faraday cups, mass 44 ($^{12}C^{16}O_2$), mass 45 ($^{13}C^{16}O_2$ or $^{12}C^{17}O^{16}O$), and mass 46 ($^{12}C^{16}O^{18}O$) (Clark & Fritz, 1997), which are measured instantaneously and expressed as ratio 46/44 for oxygen isotopes (Sharp 2007), and 45/44 and/or 45/46 for oxygen isotopes. The dual inlet system of the mass spectrometer allows for alternatively measuring the isotopic ratio of the standard, and the sample, hence the fractionation occurring in the ionization process is accounted for (Clark & Fritz, 1997).

The Finnegan MAT 251 and 253 is equipped with a Kiel carbonate preparation device which allows for automatic generation of CO_2 gas from carbonate shells, and direct pumping of CO_2 into the inlet system. The method was developed by McCrea (1950) where CO_2 gas is generated by reacting with 100 % phosphoric acid (H_3PO_4) at 70 °C (equation 3.1).

$CaCO_3 + H_3PO_4 \quad CaHPO_4 + CO_2 + H_2O$ Equation 3.1 (McCrea 1950)

According to the equation, all carbon present in the original calcium carbonate is present in the CO_2 gas, thus, no fractionation of carbon occurs in this reaction. On the other hand, only two of three oxygen atoms present in the $CaCO_3$ goes into the CO_2 gas, which results in a fractionation. Fortunately the fractionation is constant for a given temperature (McCrea 1950), and is easily corrected for. As long as acid does not exchange oxygen with the CO_2 gas, the mass spectrometer will record the correct isotopic signal; hence, it is important to use water-free phosphoric acid (Clark & Fritz, 1997).

The Kiel device has the ability of reacting and producing CO_2 gas from 46 glass vials in one setting, usually 38 samples and 8 standards. The ideal sample weight for the MAT 253 mass spectrometer is 30 µm, but in this study samples as low as 11 µm have been successfully analyzed (*C. wuellerstorfi*). All samples of *C. wuellerstorfi* were weighed to make sure they were within the acceptable limit. The planktonic foraminifers individual weight were checked prior to the measurements, and generally 5-7 shells of *G. bulloides* were used for each sample, and 5 and 10 for *G. inflata* and *N. pachyderma* (d), respectively. Using several shells in each sample ensures a good average isotopic signal for that particular depth in the core, thus limiting possible environmental variations. All three planktonic foraminifer species were measured in duplicates for every 0.5 cm in the multicore. Unfortunately, the abundance of *C. wuellerstorfi* in the multicore was sparse. Therefore, a complete record of every 0.5 cm in the core was impossible, and duplicates were made only when enough shells were present. The abundance of *C. wuellerstorfi* in the gravity core was higher, and nearly a complete record was achieved, with duplicate measurements carried out when enough shells was present. From the gravity core, stable isotopic analyses of planktonic foraminifers were recorded only from *N. pachyderma* (d) and *G. bulloides*, and duplicates from *N. pachyderma* (d) only. The purpose of duplicate measurements is to check that the isotopic signature of the foraminifers reproduces well, thereby limiting the total amount of errors.

3.2.6 Standards

All isotopic measurements preformed by mass spectrometers are calibrated against common accepted standards to ensure that a measured isotopic ratio from one mass spectrometer can be compared with measurements from another mass spectrometer. Thus, the measured isotopic signature of any substance should be the same no matter which mass spectrometer used (Sharp 2007). International standards are available in limited quantities, and are not meant to be used as a working standard in mass spectrometer laboratories. Standards are

available from either the National Institute of Standards and Technology (NIST), formerly known as the National Bureau of Standards (NBS) (Clark & Fritz, 1997), or the International Atomic Energy Agency (IAEA).

The supply of the original carbonate standard, PDB (a Cretaceous belemnite from the Peedee Formation in North Carolina, PDB-1) (Bradley 1999), is completely exhausted, hence a new reference scale has been created by the IAEA called the Vienna PDB (VPDB) (Clark & Fritz, 1997), which all carbonate samples are now reported against. For comparison of oxygen isotopic values between fossil carbonate samples of foraminifers (reported relative to VPDB) and ocean water (reported relative to VSMOW), conversions are needed (Equation 3.2 & 3.3).

$$\delta^{18}O_{VSMOW} = 1.03091 \cdot \delta^{18}O_{VPDB} + 30.91$$ Equation 3.2 (Coplen et al., 1983)

$$\delta^{18}O_{VPDB} = 0.97002 \cdot \delta^{18}O_{VSMOW} - 29.98$$ Equation 3.3 (Coplen et al., 1983)

The GMS laboratory at the BCCR calibrates its own Carrera Marble (CM03) working standard (used in the mass spectrometer), and uses NBS 19 and NBS 18 to convert the measured values from the mass spectrometer to the VPDB reference scale.

3.3 Stable isotopes

Stable isotopes of mainly oxygen and carbon are extensively used for paleoclimatological and paleoceanographical studies. Oxygen isotopes are mainly used for ice volume/sea level studies (Ruddiman 2001), paleotemperature and salinity reconstructions, while carbon isotopes are mainly used for paleocirculations reconstructions. Thus, stable isotopes are a powerful tool for investigating past climate and ocean circulation patterns. However, the field of stable isotope geochemistry is extensive and complicated, thus, only a brief discussion of the more important aspects concerning the nature and distribution of oxygen and carbon isotopes in the atmosphere and oceans will be presented here.

Isotopes are atoms with the same amounts of protons but different amounts of neutrons within their nucleus. Hence, isotopes have the same atomic number, but different atomic weights. Thus, isotopes are abbreviations of the same element based on atomic weight differences. Most isotopes are stable, but some are unstable (radioactive), meaning that the isotopes spontaneously decays to a lower energy configuration because of instability in the nucleus.

3.3.1 Oxygen isotopes

The oxygen atom has 8 protons and 8-10 neutrons in its nucleus, thus, there are three isotopes of this element, ^{16}O (8 protons + 8 neutrons), ^{17}O (8 protons + 9 neutrons), and ^{18}O (8 protons + 10 neutrons). 99.76 % of all oxygen on earth resides as ^{16}O, 0.04 % as ^{17}O, and 0.2 % as ^{18}O (Bradley 1999). Due to its low abundance, ^{17}O has very little significance in paleoclimatological and paleoceanographic studies, and will not be discussed in detail.

Consider the water molecule $H_2{}^{16}O$, and $H_2{}^{18}O$. $H_2{}^{16}O$ has a lower vapor pressure than $H_2{}^{18}O$, hence, during evaporation, $H_2{}^{16}O$ will more readily evaporate from the water body than $H_2{}^{18}O$ (Bradley 1999). Thus, continuing evaporation of a water body will make the vapor enriched in ^{16}O and depleted in ^{18}O, while the water becomes enriched in ^{18}O and depleted in ^{16}O. This effect is called fractionation, and there are three types of fractionation: Physiochemical fractionation under equilibrium conditions, mass dependent kinetic fractionation under non-equilibrium conditions, and molecular diffusion fractionation (Clark & Fritz, 1997). For paleoclimatological and paleoceanographical investigations using oxygen and carbon isotopes, physiochemical fractionation is the most important type. Physiochemical fractionation occurs due to the differences in bond strength between the light and heavy isotopes of a given element (Clark & Fritz, 1997). Lighter isotopes have a higher vibrational energy, and weaker bonds connecting them to the element than the heavier isotope, hence they are more readily broken free during a chemical reaction (Clark & Fritz, 1997). Molecules are always seeking the lowest energy configuration, but as the temperature increases, all isotopes become more energized, and finally, the temperature reach a point where all isotopes have such high vibrational energies that they break free despite the mass differences, and no fractionation between the heavy and light isotopes occurs. Thus, fractionation is mass and temperature dependent (Bradley 1999). The ratio between $^{18}O/^{16}O$ is called the fractionation factor (α) (Emiliani 1955), and is presented as seen in equation 3.4 & 3.5.

$$\alpha = \frac{R_{reactant}}{R_{product}}$$ Equation 3.4 (Clark & Fritz, 1997)

$$\text{e. g. } \alpha^{18}O_{water\text{-}vapor} = \frac{^{18}O/^{16}O_{water}}{^{18}O/^{16}O_{vapor}}$$ Equation 3.5 (Clark & Fritz, 1997)

Fractionation of oxygen will only affect the $^{18}O/^{16}O$ ratio in the fifth to sixth decimal place; thus, normal gas mass spectrometers cannot measure this difference to any extent (Clark & Fritz, 1997). Therefore, rather than measuring the exact α, one measures an apparent ratio

(Clark & Fritz, 1997), the δ, which makes it easier for the mass spectrometer to measure the already small isotopic differences (Emiliani 1955). The δ is calculated by measuring a known reference gas on the mass spectrometer at the same time as the $^{18}O/^{16}O$ ratio of the sample is measured. Thereafter, the ratio of the sample is compared with the ratio of the standard (Equation 3.6) (Clark & Fritz, 1997). Thus, the measured $\delta^{18}O$ value is reported as a deviation from a common reference point (Ruddiman 2001). Equation 3.6 states the $\delta^{18}O$ value is multiplied by 1000 to change the small variations in $^{18}O/^{16}O$ to a more workable numerical form, and reported as deviations from the standard in parts per mill (‰) (Ruddiman 2001).

$$\delta^{18}O = \frac{(^{18}O/^{16}O)\ \text{sample} - (^{18}O/^{16}O)\ \text{standard}}{(^{18}O/^{16}O)\ \text{standard}} \times 1000$$ Equation 3.6 (Emiliani 1955)

Most foraminifer species living in the ocean precipitate shells of $CaCO_3$ from the ambient water. During precipitation fractionation occurs, and the resulting shell becomes slightly enriched in ^{18}O (Bradley 1999), thus, it has a $\delta^{18}O$ value slightly higher than the water which it precipitated from. This fractionation, as mentioned above, is a function of temperature, which was first shown by Urey (1947; 1948). Urey (1948) suggested that if marine carbonate shell secreting organisms precipitate their shells in equilibrium with ambient water, and where then preserved unchanged in the sediments on the ocean bottom, it would only be necessary to measure the $^{18}O/^{16}O$ ratio of the shell to know at which temperature it lived. Following Urey's results, a series of investigations were carried out to define a paleotemperature equation (McCrea 1950; Epstein et al., 1951; Urey et al., 1951; Epstein et al., 1953). Since Urey's findings many paleotemperature equations have been presented, however, they are essentially the same equation, but differs from each other because of the different techniques used during the analyzes, and at different fractionation temperatures (Bradley 1999). Equation 3.7 is a paleotemperature equation based on Epstein et al. (1953) equation, but slightly modified after Craig (1965).

$$T = 16.9 - 4.2\,(\delta_c - \delta_w) + 0.13\,(\delta_c - \delta_w)^2$$ Equation 3.7 (Epstein et al., 1953; Craig 1965)

T is temperature measured in °C, δ_c is the per mill $\delta^{18}O$ difference between the carbonate and the standard used, while δ_W is the per mill $\delta^{18}O$ difference between the water the carbonate precipitated from, and the SMOW (Standard Mean Ocean Water) standard. Based on this equation, it becomes clear that increasing temperatures will result in lower $\delta^{18}O$ values. As the

equation states, the ocean's $\delta^{18}O$ values has to be known to estimate a paleotemperature, which is not a problem for modern samples, but for the past ocean it is not known, and cannot be expected to be the same as today (Bradley 1999). For example, during the last glacial maximum (LGM), the huge ice-sheets that coved much of the northern hemisphere was relatively highly enriched in ^{16}O, caused by fractionation during the repeated evaporation and condensation steps when water vapor moves from the tropics to higher latitudes (Ruddiman 2001). The build up and storage of freshwater enriched in ^{16}O on land affected the $\delta^{18}O$ value of the oceans, thus, making it enriched in ^{18}O.

$\delta^{18}O$ values does not only vary due to temperature and ice-sheet buildup, but also with salinity. With increasing salinity the $\delta^{18}O$ values increases, and there seems to be a 1:1 relationship (Epstein et al., 1951). Thus, if a record of planktonic foraminifers shows increasing $\delta^{18}O$ values through time, it would be tempting to interpret it as a surface ocean cooling, but one needs to consider the possibility that it could be caused by increasing salinity.

At the time Urey (1948; Urey et al., 1951) published their papers, it was known that carbonates could be precipitated in disequilibrium with the ambient water. However, they did not know what caused this disequilibrium precipitation; thus, they labeled it "vital effects". Vital effects in foraminifers are now believed to arise from incorporation of metabolically light CO_2 in the test of foraminifers (Grossman 1987). This leads to precipitation of oxygen and carbon in disequilibrium with the ambient water, which usually results in depletion of the heavy isotopes (lower $\delta^{18}O$ values) (Grossman 1987). The amount of uptake of metabolically light CO_2 is species dependent, and considered constant for any given species (Duplessy et al., 1970). Vital effects are more pronounced in carbon than oxygen, because the oxygen content in water is much greater than carbon. Carbon resides mostly in the form of bicarbonate, which interacts with the various metabolic products associated with shell formation (Wefer & Berger, 1991). According to Grossmann (1987), this can be minimized in foraminifer species living in low oxygen conditions that can exchange gas rapidly with the ambient water. Such species tend to precipitate tests in $\delta^{18}O$ equilibrium with the water.[3]

Other factors which need to be considered when using oxygen isotopes from foraminifer species are depth habitat, geographic distribution, and ontogenic effects. For example, many planktonic foraminifer species is found not to inhabit a specific depth in the water column (Gnassen & Kroon, 2000; Mortyn & Charles, 2003; Field 2004; Keigwin et al., 2005), which

[3] For more on vital effects on planktonic and benthonic foraminifers see chapter 3.4.

is of great importance, since temperatures decreases rapidly with depth in the upper few meters of the oceans. Thus, it affects the measured $\delta^{18}O$ value from the shell of the foraminifers. In chapter 3.4, a more thoroughly presentation will be given of the difficulties concerning the use of stable isotopes in different foraminifer species, including depth habitat, geographic distribution, and ontogenic effects.

3.3.2 Carbon isotopes

The idea of using carbon isotopes for paleocirculation investigations arise from the different fractionations of biological and chemical processes in the ocean (Curry et al., 1988). There two stable isotopes of carbon, and one radioactive, ^{12}C, ^{13}C, and ^{14}C, respectively. 99 % of the Earth's carbon resides as ^{12}C and almost all the rest as ^{13}C (Ruddiman, 2001).[4] As with oxygen isotopes it is the fractionation factor between the heavy and light isotope $^{13}C/^{12}C$ that is interesting. Due to the very small weight differences between the two isotopes, an apparent ratio instead of the real ratio is measured (Equation 4.8). Thus, the measured $\delta^{13}C$ value is reported in the per mill (‰) deviation from a common reference point (Ruddiman 2001)

$$\delta^{13}C = \frac{(^{13}C/^{12}C)\ \text{sample} - (^{13}C/^{12}C)\ \text{standard}}{(^{13}C/^{12}C)\ \text{standard}} \times 1000 \qquad \text{Equation 3.8}$$

When plants extract dissolved inorganic carbon (DIC) from the photic zone (upper 100 m of the water column) during photosynthesis, they preferably take up ^{12}C over ^{13}C, resulting in a $\delta^{13}C$ value of - 20 ‰ lower than the water in which the plants grew (Broecker & Peng, 1982). Animals that consumes the plants, incorporate into their tissue carbon isotopes of approximately the same value as the plants they eat, which when they respire, will give inorganic carbon back to the ocean with the same value (Broecker & Peng, 1982). Plants grow only in the photic zone, and when the leftover plants and dead zooplankton sinks down to greater depths, some of this material is delivered down to the deep ocean. However, most of it is oxidized back to inorganic form, and recycled within the surface waters. Nevertheless, some ^{12}C enriched carbon is transported to the deep ocean by the sinking plants and planktons, thereby enriching the surface waters in ^{13}C. Hence, the DIC in the surface waters typically have a $\delta^{13}C$ value of 1‰ or more. Together, the small amount of organic carbon

[4] Less than 1 % of earth's carbon resides as the radiogenic ^{14}C isotope. In the context of studying paleocirculation the ^{14}C isotope is unimportant, and will not be discussed further.

with $\delta^{13}C$ values of ≈ -20 ‰, and the large amount of DIC with $\delta^{13}C$ values near + 1 ‰, cancels each other out. Thus, the mean $\delta^{13}C$ of the ocean is about 0 ‰ (Ruddiman, 2001).

When plants and organisms take up light isotopes (low values of $\delta^{13}C$), they also take up nutrients from the ocean. Thus, where nutrients are high, the values of $\delta^{13}C$ are low. Of the different nutrient in the ocean, phosphate (PO_4) is a widely used non conservative nutrient, which has an inverse correlation with the $^{13}C/^{12}C$ ratio (Broecker & Peng, 1982). Figure 3.5 shows on the left hand side a plot of the $\delta^{13}C$ and PO_4 variations with depth beneath the sea surface. In the photic zone, zooplankton and phytoplankton consumes phosphate and light carbon, which results in high values of $\delta^{13}C$, and low values of PO_4. When these organisms die and sink down into the deeper ocean they dissolve, thereby releasing phosphate and light carbon. Hence nutrient levels increase with depth while carbon isotopes become lighter.

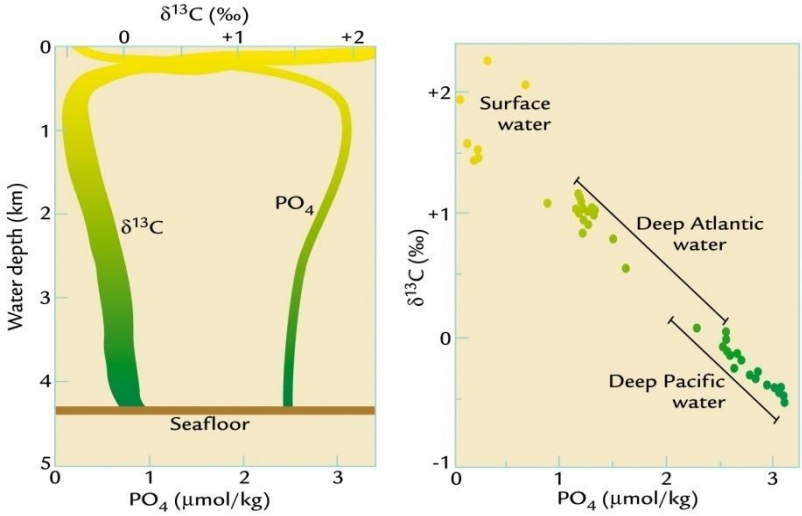

Fig. 3.5: Left: The plot shows the $\delta^{13}C$ and PO_4 variations with depth beneath the sea surface. Modified after Kroopnick (1985). **Right:** A plot showing how $\delta^{13}C$ and PO_4 varies along the flow path of deep water from North Atlantic to the North Pacific. Adapted from Boyle (1986).

The oceans are stratified; thus, communication between the surface waters and the deepwater is very slow, except the few places where deepwater is produced (Duplessy et al., 1988). Because of the intense mixing occurring when deepwater travels from the surface to the abyss, any temporal change in the $\delta^{13}C$, happens almost simultaneously in the entire water column (Duplessy et al. 1988). Thus, the high $\delta^{13}C$ produced in the surface waters, is brought down to the abyss by the sinking water almost without changing its character. Conversely, in areas where deepwater formation is absent, the surface and deepwater has very different $\delta^{13}C$ values, because the only change in deepwater isotopic composition comes from the slow

process of decomposition, and oxidation of organisms delivered from above (Curry et al., 1988).

Changes in $\delta^{13}C$ in the surface ocean are usually measured from the shells of planktonic foraminifers, while deepwater changes are measured from benthonic foraminifers. Deepwater formation happens today in two main areas; the Weddell Sea in the Southern Ocean at the coast of Antarctica, and the Norwegian and Labrador Seas. North Atlantic Deep Water (NADW) in the Norwegian Sea has high $\delta^{13}C$ values, and is the most nutrient depleted deep water mass forming in the ocean today (Curry et al., 1988). Antarctic Bottom and Deep Water (AABW & AADW) is more nutrient rich, and has low values of $\delta^{13}C$ (Curry et al., 1988). Since these water masses have very distinctive characteristics, it is possible to track the distribution and development of NADW, AABW, and AADW through the world oceans by measuring the $\delta^{13}C$ of benthic foraminifers over glacial-interglacial cycles (Curry et al., 1988; Duplessy et al., 1988).

Thus, mapping of $\delta^{13}C$ gradients from planktonic and benthonic foraminifers across the world oceans is a powerful paleocirculation tool, but as with $\delta^{18}O$, there are several complicating factors which need to be considered. Different species of planktonic and benthonic species have different depth habitat, geographical distribution, and have different responses to vital and ontogenic effects, hence one must be selective concerning the choice of species. These problems will be addressed in chapter 3.4 for the different foraminifer species used in this study.

3.4 Foraminifera

Foraminifera are single-celled, marine, microscopic organisms (zooplankton), which live in either planktonic or benthonic habitats. They consist of a soft inner tissue, called the cytoplasm, which is protected by a harder shell (test) that encloses it (Armstrong & Brasier, 2005). The tests consists usually of either secreted minerals from the marine waters the organisms live in (calcite, aragonite, opaline silica), or secreted organic matter (membranous, tectinous), but can also consist of agglutinated particles (Culver 1993). The test is built up by one or more chambers which are connected to each other by an opening called a foramen. A test with more than one opening it is called foramina (Armstrong & Brasier, 2005). Thus, the name for this animal class is derived from its characteristic chamber connection.

Foraminifers first occurred in the geological record during Early Cambrian, and have been present ever since (Armstrong & Brasier, 2005). They are abundant throughout the world's oceans, from the polar the equatorial regions. During sedimentation the soft protoplasm is dissolved, but the harder shell, which usually consists of secreted calcite, is preserved. Their abundances in sediment samples may therefore reach tens of thousands per square meter, and in tropical regions, a sample of 300 individuals can contain 60-70 different species (Culver 1993). It is estimated that there are about 5000 small benthic foraminifera species (e.g. *Cibicides wuellerstorfi*), and 100 planktonic foraminifera species living in the oceans today (Armstrong & Brasier, 2005). The study of fossil foraminifers is widely used in paleoclimatology and paleoceanography because the animals incorporate oxygen and carbonate isotopes into their carbonate shells, which can be used to reconstruct climate and ocean hydrography. For the stable isotope reconstructions in this study three planktonic foraminifera species are used, and one benthonic.

3.4.1 Planktonic foraminifera

Planktonic foraminifer's lives in the upper 1000 meters of the surface ocean, while most of them live above 200 meters water depth. Based on foraminiferal distribution worldwide, 9 foraminifer provinces are recognized: Arctic, Subarctic, Transitional, north subtropical, south subtropical, transitional, sub-Antarctic, and Antarctic (Armstrong & Brasier, 2005). Planktonic foraminifers are free floaters and feed on what they encounter, thus their food sources are very variable, but involves protists, metazoans, and also organic detritus (Culver 1993).

Globigerina bulloides (d'Orbigny 1826)

This species is non-symbiotic (Darling et al., 2006), and has a trochospiral ($CaCO_3$) test with four chambers that increases as added (Fig. 3.6). *G. bulloides* has a wide geographic distribution stretching from the subtropical to the subpolar, and lives in a temperature range of 2.1-23.3°C, while the maximum abundances are found between 9-11°C in the subpolar to transitional waters, and at salinity levels of 34.40-36.63 ‰, with a optimum between 34.40-35.87 ‰(Tolderlund & Bé, 1972).

Because of its wide distribution in the world's oceans, *G. bulloides* is extensively used for paleoclimatic and paleoceanographic reconstructions, but unfortunately it has a very complicated behavior.

Fig. 3.6: S.E.M. image of the planktonic foraminifera *G. bulloides*. Modified after Peeters (2007).

The assumption has been that it dwells in the surface of the ocean, and therefore can be used for SST reconstructions. However, recent studies has shown that it does not have a constant depth of maximum abundance (Gnassen & Kroon, 2000; Mortyn & Charles, 2003; Field 2004; Keigwin et al., 2005). According to Sautter & Thunell (1991), *G. bulloides* ascends from well below the thermocline to the surface during upwelling events when production increases due to supply of nutrient from below. Mortyn & Charles (2003) found that *G. bulloides* track phytoplankton blooms, and is mostly found at mid depths, which is in agreement with the Field (2004), were he found that the species highest abundance was within the mixed layer. Relatively high abundances were also found in the entire pycnocline depth, and below, sometimes even below the thermocline. *G. bulloides* is presumed to calcify in the summer, but as mentioned above, the species seems to track phytoplankton blooms, thus, it varies from region to region. According to studied done by Gnassen & Kroon (2000) from the North-east Atlantic, calcification occur in February-March in the south, and May-June north of 57°N, thereby reflecting the northwards migration of the spring bloom. Thus, in the region of this study, *G. bulloides* seems to record spring temperatures, even though as deep as 200 m below the surface (Gnassen & Kroon, 2000). Clearly, the use of *G. bulloides* as a surface proxy is more complicated than earlier presumed.

However, some sources of error can be avoided, such as ontogenic effects. Carbon and oxygen isotopic values of *G. bulloides* taken from the Arabian Sea showed that both isotopic signals were higher in individuals with bigger shells. The ontogenic influence was also greater in $\delta^{13}C$ than $\delta^{18}O$ (Naidu & Niitsuma, 2004). This result is in agreement with Keigwin et al. (2005), and with experimental data from Spero & Lea (1996), where it was suggested that the observed ontogenic trend may be due to incorporation of metabolic light CO_2 during calcification. In this study, ontogenic effect was avoided by picking individuals of *G. bulloides* from the 350-250 μm fraction only.

G. bulloides is known to suffer from vital effects. Experimental studies of *G. bulloides* by Spero & Lea (1996) showed that their $\delta^{18}O$ value co-varied in the same manner as the theoretical paleotemperatures, but was offset from equilibrium. Concerning $\delta^{13}C$ values, Naidu & Niitsuma (2004) noticed that the *G. bulloides* values was 1‰ lower than the benthic

species *Uvigerina exellens*, which could not be explained by other than vital effects. Thus, it seems clear that vital effects are a problem with *G. bulloides*, but if the disequilibrium value is known, it can be corrected for.

Neogloboquadrina pachyderma (Ehrenberg 1861)

This species is non-symbiotic, has a calcium carbonate ($CaCO_3$) test with usually 4 chambers in the final state (Dahl 2007). *Neogloboquadrina pachyderma* is a trochospiral arranged planktonic foraminifer species with two different coiling directions, and its distribution is largely controlled by temperature (Dahl 2007). The left coiling individuals is called *N. pachyderma* sinistral [hereinafter *N. pachyderma* (s)], and thrives in the cold polar to subpolar waters, while the right coiling individuals is called *N. pachyderma* dextral, and thrives in the warmer subtropical to subpolar waters (Dahl 2007). However, even in extreme Polar Regions, a small percentage of *N. pachyderma* (d) still exist (Bauch et al., 2003). Hence, it is not completely restricted to temperate regions. Due to its wide distribution around the world oceans, *N. pachyderma* (d) is often used for paleoclimatological and paleoceanographic reconstructions. In the arctic province of the Gardar sediment drift, every individual of *N. pachyderma* was almost exclusively the dextral kind, thus, it is the one investigated in this study (Fig. 3.7).

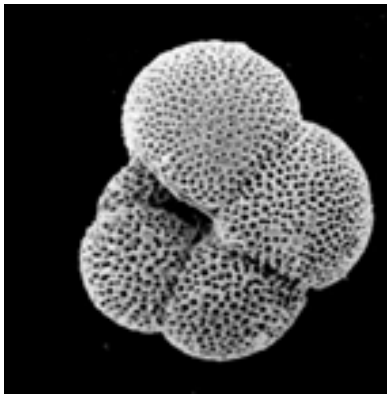

Fig. 3.7: *N. pachyderma* (d) as it normally appeared in the cores collected at the Gardar drift. Modified after Ortlieb et al. (2000).

Earlier it has been assumed that the two types of *N. pachyderma* were genetically similar, but a recent publication by Bauch et al. (2003) has shown that there exist at least 3 genotypically distinct *N. pachyderma* variants. Darling et al. (2006), believes that the genetically distinctions between the right coiling genotypes, and left coiling genotypes, are so large that a new name for the right coiling genotypes is appropriate. They suggest the name *Neogloboquadrina incompta* for the species formally known as *N. pachyderma* (d).

Bauch et al. (2003) found that under polar conditions, above 70 °N, where the abundance of *N. pachyderma* (d) is low (less than 5%), the $\delta^{18}O$ signal for sinistral and dextral are fairly similar, which means that they are the same genotype, *N. pachyderma* (s). Between 70-64 °N

the abundance of *N. pachyderma* increases and all the right coiling individuals are now genotypically *N. pachyderma* (d). However, all left coiling *N. pachyderma* is still genotypically *N. pachyderma* (s). Thus, the two coiling kinds are genetically different in this area, which is noticeable in the $\delta^{18}O$ values, were they can differ as much as 1 ‰. South of 64°N, the abundance of *N. pachyderma* (d) is very high (more than 95%) and all right coiling individuals are *N. pachyderma* (d), while the right coiling individuals are *N. pachyderma* (s).

Since both cores used in this study is collected below 64 °N, and the percentage of left coiling individuals is less than 5%, Bauch et al. (2003) results are in agreement with our findings, and we can be reasonably certain that the right coiling *N. pachyderma* used for the isotopic studies is *N. pachyderma* (d).

N. pachyderma (d) is mainly used as a proxy for sea surface temperature (SST) reconstructions, but studies in the recent years has shown that it does not inhabit a specific depth. A study in the California Current System by Field (2004), found that *N. pachyderma* (d) generally lives within the upper thermocline, but varies considerably in habitat depth, ranging from the mixed layer to the deeper thermocline, which is difficult to attribute to specific environmental factors. Field (2004) also found that at a significant portion of the *N. pachyderma* (d) tests lived below 100 m. However, the highest abundances were found within the mixed layer, and the chlorophyll maximum, which is concurrent with other high latitude studied (Mortyn & Charles, 2003). Mortyn & Charles (2003) studied plankton tows from the Atlantic sector of the Southern Ocean and found that *N. pachyderma* (d) is mostly observed to dwell in the mid-depths, and that the species may be more surface restricted at higher latitudes. Their core top $\delta^{18}O$ curve followed the predicted $\delta^{18}O$ curve over the full range of the dataset. Studies from the San Pedro Basin, Southern California Bight, have measured the $\delta^{13}C$ signal of *N. pachyderma* (d) and found that it records the $\delta^{13}C$ of equilibrium calcite from just below the thermocline (Sautter & Thunell, 1991). Thus, vital effects seem not to affect *N. pachyderma* (d) substantially.[5] With this into consideration, it seems that *N. pachyderma* (d) is a reliable proxy for SST variability at high latitudes.

Ontogenic effects caused by different sizes of *N. pachyderma* (d) with depth, has been tested for by Field (2004), were he found that the seasonal range in $\delta^{18}O$ values is not likely caused by changes in test size. However, since this is only one study, there is still a possibility that

[5] For more on vital effects in *N. pachyderma* (d) and (s) see Appendix H.

ontogenic effects is a problem with *N. pachyderma* (d). Therefore, this species was only picked in the 250-150 μm range in this study.

The blooming period of *N. pachyderma* (d) is not investigated at the study site, but as Tolderlund and Bé (1971) indicated, the absolute abundance of *G. pachyderma* right coiling occurs in the warm fall months in the subpolar region. Even though Tolderlund and Bé (1971) has labeled the species *G. pachyderma,* it is very likely that it is the same species as *N. pachyderma* (d). According to Mortyn & Charles (2003) the blooming season of *N. pachyderma* (d) is in the austral summers of the Southern Ocean. In light of these studies, it is assumed that *N. pachyderma* blooms somewhere between late spring and autumn.

<u>*Globorotalia inflata*</u> (d'Orbigny 1839)

G. inflata is also a non-symbiotic (Cléroux et al., 2007) trochospirally coiled species, with usually three chambers in its final state (Fig. 3.8) The species thrives best in transitional waters at temperatures between 2.2-26.9 °C, with peak concentrations between 10.4-19.9 °C, and salinity ranges between 34.87-36.63 ‰ (Tolderlund & Bé, 1971). The species is also observed in the subtropics in both hemispheres (Pflaumann et al., 1996).

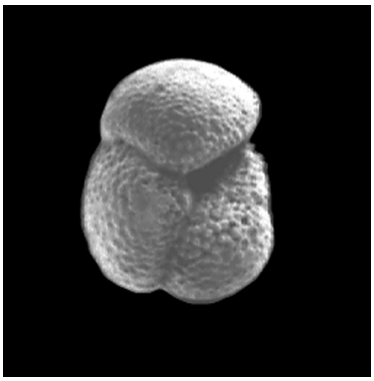

Fig. 3.8: S.E.M. image of *G. inflata*. Slightly modified after Olney (2002).

As the two other planktonic species used in this study, *G. inflata* does not inhabit a specific depth in the water column, but it is known to be a relatively deep dwelling species (Mortyn & Charles, 2003). South of 44°N it is known to track the annual temperatures at depths between 300-400 m, between 44-56 °N at depths between 200-400 m, and north of 57°N, between 100-200 m (Gnassen & Kroon, 2000). This is in agreement with Mortyn & Charles (2003) were *G. inflata* is found to be most abundant between 50-300 m. Newly published data by Cléroux et al. (2007) from the North Atlantic Ocean, indicates that *G.inflata* thrives best at the base of the summer thermocline, if the temperature does not exceed 16°C. If it does exceed 16°C, *G. inflata* moved down to the upper part of the main thermocline. According to Cléroux et al. (2007), the temperatures at the base of the summer thermocline is close to that of winter conditions, therefore they concluded that *G. inflata* lives within the winter mixed layer. Based on these result, this

author is confident that *G. inflata* is a good indicator for winter temperatures at the base of the summer thermocline, or upper main thermocline.

Cléroux et al. (2007) also tested for possible size effects in the $\delta^{18}O$ values of *G. inflata,* and concluded that no apparent size effects were recorded in the oxygen isotopes. However, to be certain that possible ontogenic effects were avoided, *G. inflata* were picked in the 300-250 µm size interval.

Mortyn & Charles (2003) tested for possible vital effects, and found that *G. inflata* trace the values of predicted $\delta^{18}O$ values with no apparent offset. However, according to Niebler et al. (1999), Ganssen (1983) reported an small $\delta^{18}O$ equilibrium offset of ± 0.4 ‰. Thus vital effects are something that needs to be considered when working with *G. inflata.*

3.4.2 Benthonic foraminifera

Benthonic foraminifera can live in the whole depth range of the world oceans, from the photic zone to the abyssal depths, and they have either epifaunal or infaunal habitats. Benthic foraminifers are micro-omnivores which are known to feed on bacteria, invertebrates, and protozoa (Armstrong & Brasier, 2005).

Cibicides wuellerstorfi (Schwager, 1866)

C. wuellerstorfi has a planoconvex test built up by $CaCO_3$, and it lives epifaunal, at water depths between 1000-3000 m, were it attaches itself with its flat side to rocks, or other hard substrates (Dahl 2007). The species is often referred to as *Cibicidoides*, *Cibicides*, or *Planulina wuellerstorfi*, but it is essentially the same species (Wefer & Berger, 1991) (Fig. 3.9).

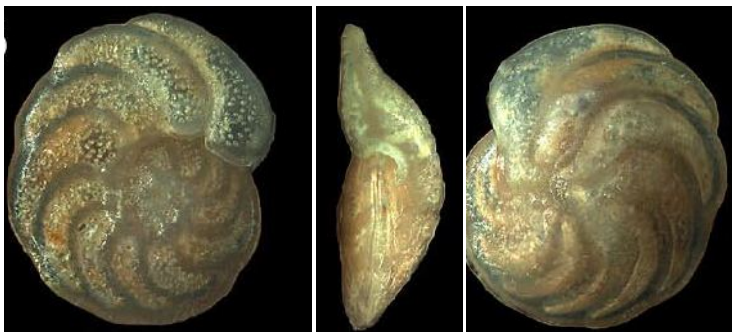

Fig. 3.9: Images of *C. wuellerstorfi*. **Left**: The flat spiral side which it uses to attach itself to a rock or another hard substrate. **Center**: Side view were its planoconvex shape is visible. **Right**: Umbilical view. Modified after Holbourn & Henderson (2002).

According to Wefer & Berger (1991), *C. wuellerstorfi* do not suffer from ontogenic effects. In the two cores used in this study, the availability of *C. wuellerstorfi* were sparse, thus every specimen found were used in the isotopic studies, unless they were too small to be measured by the mass spectrometer (< 6 μm).

Duplessy et al. (1970) was the first to report about vital effects in *P. wuellerstorfi*. They recorded the $\delta^{18}O$ values of various benthic species, *Pyrgo sp.*, and *P. wuellerstorfi*, sampled at the same depth, and found that they were basically parallel, but offset by 1 ‰ or more. This is in agreement with Grossman (1987) were he found that *P. wuellerstorfi* deviated about -1.5 ‰ from equilibrium. A study by Graham et al. (1981) showed that, even though *P. wuellerstorfi* precipitated oxygen isotopes in disequilibrium with the ambient seawater, the species showed no difference in $\delta^{18}O$ disequilibrium between the Atlantic, Pacific, or Indian Ocean (Graham et al., 1981). Thus, the disequilibrium factor is the same in all three oceans, and can be corrected for. Concerning disequilibrium in $\delta^{13}C$, Graham et al. (1981) found that *P. wuellerstorfi* deviated from equilibrium with about - 1‰, which is very close to $\delta^{13}C$ of bottom water TCO_2. The finding of Graham et al. is in agreement with Grossman (1987). Grossman found that the $\delta^{13}C$ values of *P. wuellerstorfi* faithfully reflect the isotopic composition of dissolved inorganic carbon that resides in the bottom water.

3.4 Mean sortable silt

The sortable silt mean grain-size paleocurrent proxy arises from the sedimentary behavior of fine sediments in the deep-sea. Fine sediments, delivered to the sea floor as pelagic flux, has such a slow settling velocity that most of the particles would not reach the sea floor, had they not flocculated together into aggregates consisting of terrigenous and biogenic particles (McCave 2005). In the absence of deep-water currents, these aggregates would plummet to the sea-floor intact (McCave 2005). Sedimentary drifts like the Gardar drift, arises from sediment focusing caused by the movement of deep-water currents, which also sorts the sediments.

Sorting of fine sediments in areas with deep-water currents happens principally during deposition, or resuspension, when aggregates break up and is sorted by size, due to different stress and settling velocities (McCave et al., 1995). When the aggregates break up, particles between 63-10 μm behave non-cohesively, and are sorted by selective deposition based on size differences, while particles below ~ 10 μm behave cohesively, partly due to adhering of

clay particles with unbalanced electrical charges, but also because of van der Waals forces (McCave et al., 1995). Larger particles like foraminifers are generally not moved at deep-water current speed, unless the flow reaches 20-25 cm s^{-1} (McCave & Hall, 2006). Thus, silt particles in the 10-63 μm size fraction is sorted by currents, and can be used as a paleocurrent proxy (McCave et al., 1995).

The idea of using the sortable part of the silt fraction as a paleocurrent proxy was introduced by Ledbetter & Johnson (1976; Blaeser & Ledbetter, 1982; Ledbetter 1986) in studies from the Vema channel in the southwest Atlantic. Ledbetter (1986) used the 4-63 μm of the silt fraction for his study, but subsequent evidence has shown that the fraction between 4-10 μm should be avoided because of its cohesive behavior (McCave et al., 1995; McCave & Hall, 2006), which would reduce the parameters responsiveness to grain size differences. McCave et al. (1995) concluded that the best parameter to infer paleocurrent from is the mean size of the 10-63 μm terrigenous fraction which they labeled "sortable silt", or simply $\overline{SS}$. They argued that only the terrigenous fraction should be used, because biogenic materials have size modes that are species characteristics, and can therefore bias the signal. Hence, carbonates and silica should be removed prior to the sortable silt measurements.

There are several instruments that can measure the sortable silt proxy, but presently the Sedigraph and Coulter Counter have shown the most promising results. The Sedigraph uses a sedimentation principle and is based upon the settling velocity of sediments, which is closely related to the transport and depositional processes that sorts sediments (McCave & Hall, 2006). According to McCave & Hall (2006), the Sedigraph is the best choice for sortable silt measurements, but it can also be done satisfactory with a Coulter Counter (Bianchi et al., 1999). The Coulter Counter works with that the silt particles are embedded in an electrolyte solution, which an electric field is passed through. The particles produce a voltage proportional to its volume, which experiments have shown is related to spherical particle volume (Bianchi et al., 1999). Thus, the Coulter Counter measures the average size of the particles embedded in the electrolyte solution. Laser particle sizer should be avoided, because if there are abundant platy particles in the sediment the instrument will overestimate its size, and assign it with a bigger settling velocity than it actual has, hence it will bias the measurements (McCave & Hall, 2006). Our choice for the sortable silt measurements was the Coulter Counter, because it is efficient and gives reliable results (Bianchi et al., 1999).

Like every proxy, mean sortable silt has its limitations and sources of error. The sortable silt paleocurrent proxy measures relative flow speed, and cannot distinguish between changes caused by variations in the mean flow (mean kinetic energy K_M), or the variability of the flow (eddy kinetic energy K_E) (McCave et al., 1995). According to McCave et al. (1995), good settings for sortable silt paleocurrent reconstructions are areas were $K_M > K_E$. The Gardar sediment drift is a good example for that, were sortable silt measurements have shown very promising results (Bianchi & McCave, 1999; Boessenkool et al., 2007a; b).

The Coulter Counter used for the sortable silt measurements on the multicore GS06-144-09 MC-D is a Beckman Coulter Multiziser™ 3, Coulter Counter ®. Prior to the measurements, the instrument was calibrated with latex beans that measured 20 μm in diameter, to assure good accuracy and precision. The Coulter Counter's specialized beaker was filled with isoton solution (electrolyte) up to a certain level, and then 250 ml of the sample, collected using a pipette at a specific depth in the nalgene bottles, was added. To ensure good dispersion of the sediment in the beaker while measuring the sediment sizes, a stirrer was used. The Coulter Counter measured the mean, mode, and median of ~70 000 particles in each run. After completing the run, the beacon was cleaned, new isoton was added, and the process was repeated with the next sample.

4. CHRONOLOGY

4.1 Dating methods

The age model of core GS06-144-09 MC-D is based upon ^{210}Pb dating carried out at the Gamma Dating Center, Institute of Geography, University of Copenhagen, Denmark, and Accelerator Mass Spectrometry (AMS) ^{14}C dating carried out at Leibniz-Laboratory for Radiometric Dating and Stable Isotope Research, Christian-Albrechts-University of Kiel, Germany. Core GS06-144-08 GC is dated, and correlated with the multicore, through the AMS ^{14}C dating carried out at the University of Kiel.

4.1.1 ^{210}Pb dating

The ^{210}Pb isotope is a part of the ^{238}U decay series (Flett 2003). ^{210}Pb is produced in the atmosphere from the decay of ^{222}Rn, and enters the sedimentary record through precipitation and dry fall-out (Bradley 1999). Locked in the sediments, it decays with a half-life of 22.26 years (Appleby & Oldfield, 1983) to the stable ^{206}Pb (Bradley 1999). Assuming that the atmospheric input of ^{210}Pb is constant, the decay rate from ^{210}Pb to ^{206}Pb can be used to calculate the age of the sediments, and the sedimentation rate (Bradley 1999; Flett 2003). There are three models used for calculating the ages of sediments with ^{210}Pb; CF: CS (Constant Flux: Constant Sedimentation), CRS (Constant Rate of Supply) and CIC (Constant Initial Concentration) (Appleby & Oldfield, 1983). A modified version of Appleby's (2001) CRS modeling was used to date the top 7.25 cm of core GS06-144-09 MC-D. The CRS model allows for changes in the sedimentation rates, because it assumes that the flux of ^{210}Pb from the atmosphere is constant, thus, if the supply of sediment increases (decreases) the content of ^{210}Pb increases (decreases) accordingly (Appleby & Oldfield, 1983). However, the model has its limitations (see Appleby & Oldfield, 1983; Appleby 2001, for more information).

Based upon the measurements of ^{210}Pb, it was found that the lead content decreased exponentially down to 7.25 cm, which indicates that there is no apparent change in the sedimentation rate, and that the core is not subjected to bioturbation or mixing (Andersen 2007). In addition to ^{210}Pb, ^{137}Cs were measured. In the top of 4 cm of the core there were found measureable amounts of ^{137}Cs (Andersen 2007). Based on the ^{210}Pb dating, the top 4 cm of the core is younger than 1957 AD, which coincides closely with the timing of the first release of the ^{137}Cs isotope into nature, thus supporting the ^{210}Pb dating (Andersen 2007).

Table 4.1 gives the estimated age of the top 7.25 cm of core GS06-144-09 MC-D based upon ^{210}Pb dating.

Table 4.1: Results of the ^{210}Pb dating on core GS06-144-09 MC-D, using the CRS model. Also shown is the corresponding accumulation rate.

Core depth (cm)	**Calendar year (AD)**	**Accumulation rate (kg/m^2/yr)**
0,00	2006	
0,25	2002	0,12
0,75	1995	0,11
1,25	1989	0,11
1,75	1983	0,12
2,25	1977	0,13
2,75	1970	0,12
3,25	1963	0,12
3,75	1957	0,14
4,25	1950	0,14
4,75	1943	0,14
5,25	1937	0,16
6,25	1925	0,15
6,75	1918	0,13
7,25	1909	0,11

4.1.2 AMS Radiocarbon (^{14}C) dating

^{14}C atoms are produced in the upper atmosphere by collisions with the neutrons of atmospheric nitrogen atoms (Bradley 1999). The produced ^{14}C atoms are quickly oxidized into $^{14}CO_2$, and mixed with the rest of the CO_2 in the atmosphere, thus, the CO_2 interacts with the entire hydrosphere and biosphere (Lowe & Walker, 1997). All organisms absorbs CO_2 while growing, hence all organisms contains some amounts of ^{14}C isotopes (Lowe & Walker, 1997). As long as the organism is alive, the ^{14}C isotopes that decays to stable nitrogen (half-life 5730±30 years, Bradley 1999) is continuously replenished by new ^{14}C isotopes, hence the amount of ^{14}C is broadly in equilibrium with atmospheric CO_2 (Lowe & Walker, 1997). When the organism die the replenishment of ^{14}C stops, and the content of ^{14}C will decrease as ^{14}C decays to nitrogen (Lowe & Walker, 1997). Thus, by measuring the ^{14}C content in dead organic organisms, one can calculate the amount of years passed since it died (Bradley 1999).

Three samples of *N. pachyderma* (d) from core GS06-144-09 MC-D was AMS radiocarbon dated, while 5 samples of *N. pachyderma* (d) from core GS06-144-08 GC. Calibration from

radiocarbon years to calendar years was achieved by using the calibration program Calib Rev 5.0.1 (Stuiver & Reimer, 1993) with the calibration data set marine04.14c (Hughen et al., 2004), which assumes a global ocean reservoir correction of 400 years. Table 4.2 & 4.3 gives the ^{14}C dates for core GS06-144-09 MC-D and GS06-144-08 GC, respectively.

Table 4.2: Samples dated with ^{14}C AMS method in core GS06-144-09 MC-D. [a)] 0 BP= 1950 AD.

Laboratory number	**Core depth (cm)**	**^{14}C AMS Age (yr BP)[a] ± 1σ error**	**Calibrated age (AD)**	**Age range ± 1σ**	**Comments**
KIA 34242	0	75 ± 20	> 1950		Bomb ^{14}C
KIA 34243	11,5	530 ± 20	1768	1719-1817	
KIA 34244	30	750 ± 20	1551	1511-1591	

Table 4.3: Samples dated with ^{14}C method in core GS06-144-08 GC. [a)] 0 BP= 1950 AD.

Laboratory number	**Core depth (cm)**	**^{14}C AMS Age (yr BP)[a] ± 1σ error**	**Calibrated age (AD)**	**Age range ± 1σ**	**Comments**
KIA 34245	0	720 ± 25	1545	1504-1585	
KIA 34246	0	755 ± 20	1589	1547-1631	
KIA 34247	40	1350 ± 25	1050	1016-1083	
KIA 34248	40	1400 ± 25	1010	981-1039	
KIA 34249	80	1980 ± 25	409	369-449	

4.2 Age models

4.2.1 Age model for core GS06-144-09 MC-D

Figure 4.1 shows the age model for the multicore. The age model for the first 7.25 cm of the core is constructed by linear interpolation between the ^{210}Pb dates, while the age model between 11.5 and 44.5 cm is constructed by linear interpolation between the two ^{14}C dates. To construct a complete age model, the ages from the two dating methods is combined using a simple linear fit (7.25-11-5 cm). The AMS ^{14}C date from 0 cm contained bomb radiocarbon, which, together with the presence of ^{137}Cs in the top 4 cm from the lead dates, confirms that the top is younger than ~1950. Furthermore, since the multicore had a clear sediment-water interface, it is assumed that the top (0 cm) dates from 2006 when the core was collected. This age model is based upon a conservative approach, thus, the age offset between the lead and the radiocarbon ages is not necessarily as big as figure 4.1 indicates. Within the 1σ

uncertainty of the ^{14}C dates the age model can be moved up, which would make the age offset less.

Based upon the age model the sedimentation rate is ~74.7 cm/1000 years, ~30.1 cm/1000 years, and ~83.6 cm/1000 years for the intervals from 0-7.25 cm, 7.25-11.5 cm, and 11.5-44 cm, respectively. On average the sedimentation rate is ~71.5 cm/1000 years.

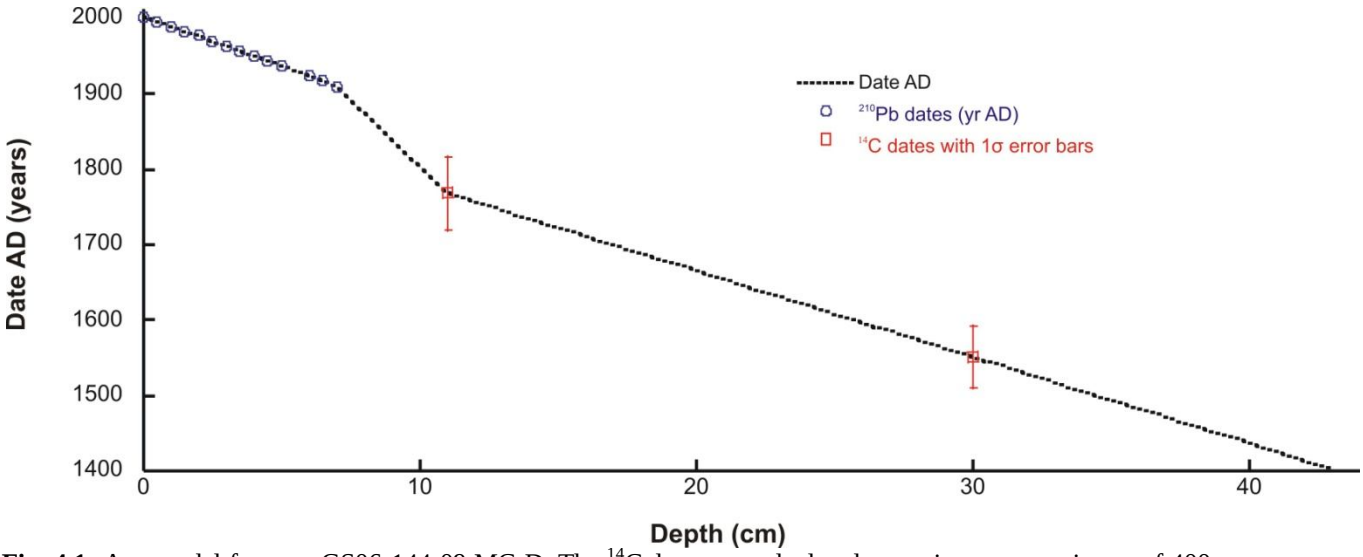

Fig. 4.1: Age model for core GS06-144-09 MC-D. The ^{14}C dates are calculated assuming a reservoir age of 400 years.

4.2.2 Combined age model for core GS06-144-09 MC-D and GS06-144 08 GC

On core GS06-144-08 GC two AMS ^{14}C dates were measured for 0 and 40 cm depths (Table 4.3). To construct a combined age model for the two cores only dating KIA 34246 from 0 cm in the gravity core were used, because it is closest to the dating from the multicore (KIA 34244, table 4.3). For the 40 cm interval the two dates were averaged:

^{14}C AMS age (1350 + 1400)/2 = 1375 ± 25 BP, which when calibrated using the calibration program Calib Rev 5.0.1 (Stuiver & Reimer, 1993), with the calibration data set marine04.14c (Hughen et al., 2004), yields 1026 ± 28 AD. Thus, the ^{14}C age constraint points for the gravity core used in the combined age model is 1589 ± 42 AD, 1026 ± 28 AD, and 409 ± 40 AD. The gravity core has a ~15 cm overlap with the multicore. The combined age model is constructed by comparing peaks in the *N. pachyderma* (d) curve from the multicore with peaks in the *N. pachyderma* (d) from the gravity core in the overlapping areas between the two cores (Fig. 4.2). Outside the overlapping area the combined age model for the two cores is based upon the previously described age model for the multicore, and linear interpolation between the age

constraint points from the gravity core. Average sedimentation rate for the gravity core is ~65.6 cm/1000 years, while the average sedimentation rate for the two cores combined is ~68 cm/1000 years.

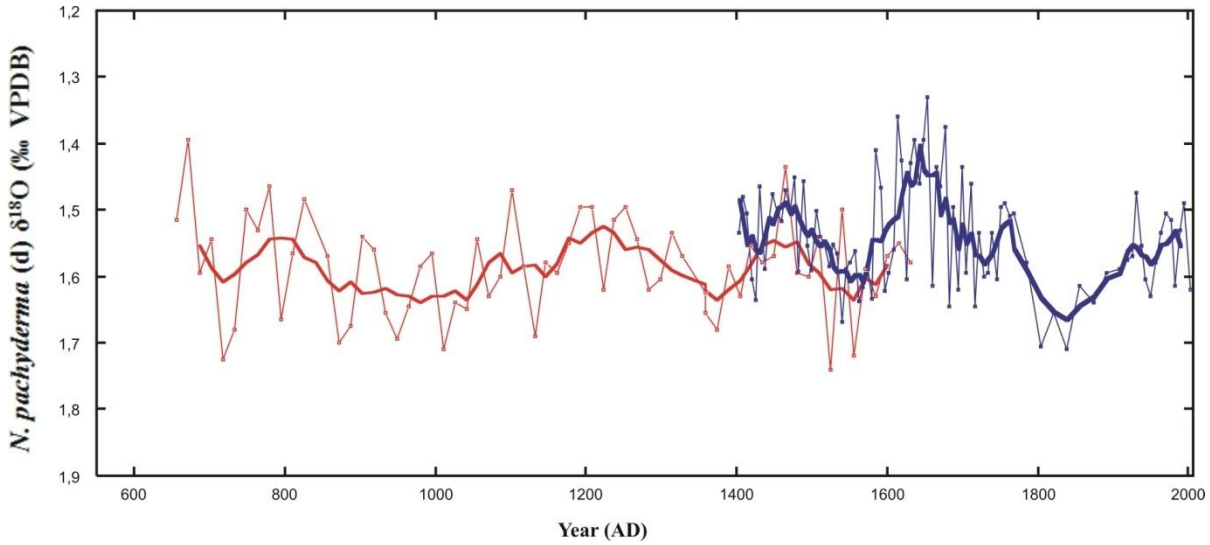

Fig. 4.2: Combined age model for core GS06-144-09 MC-D and GS06-144-08 GC. The thick blue (red) curve is a 5 point running average of *N. pachyderma* (d) measurements from the multicore (gravity core), while the thin blue (red) curve is the average of two measurements from the multicore (gravity core). The multicore has a ~15 cm overlap with the gravity core, thus, the combined age model for the two cores is constructed by comparing peaks and troughs in the curve of *N. pachyderma* (d) from both cores. Outside the overlapping area, the combined age model is based upon the previously described age model for the multicore, and linear interpolation between the age constraint points from the gravity core.

5. RESULTS

5.1 Sortable silt mean grain-size results

As outlined in chapter 4.5 the variability of near bottom flow vigor can be inferred from measurements of the "sortable silt" mean size terrigenous fraction (10-63 μm) from fine sediments. The sortable silt proxy used on core GS06-144-09 MC-D measures the relative flow speed variability of ISOW, hence increasing mean grain-size corresponds to increasing flow speed, and vice versa. Although not strictly quantitative, no calibration to absolute velocity exists, the proxy provides valuable information about relative velocity changes in ISOW through time.

All samples from core GS06-144-09 MC-D were analyzed by the mean sortable silt method using the Coulter Counter. The full sample set was analyzed in triplicate. The first run was used for training in order to acquire a consistent sampling method (results are not included here). The final two runs reproduced well, and are used here. Figure 5.1 shows the sortable silt mean grain-size results plotted against core depth to illustrate down-core variability. The red data points (circles) are the averages of two measurements, while the thick red curve connects the points. Error bars are attached to the measurements which denotes the standard error of the mean at all depths down-core. The standard deviation for the two replicates is ± 0.44μm, while the average standard error of the mean is ± 0.31 μm (Appendix F). The range of grain-size variability throughout the core is ~ 2.5 μm, far exceeding the error of each measurement. The analytical precision of the Coulter Multisizer III is measured to be less than 4 % (Hall et al., 2004). Assuming a grain-size variability throughout the core of 2.5 μm this amounts to a deviation from the mean of ± 0.1 μm. Thus, the precision of the instrument accounts for about 30 % of the standard error at all depths down-core.

Throughout the record the grain-size variability between adjacent data points are normally not more than ~0.4 μm, however, there are exceptions (e.g. 5.5-6 cm, 8.5-9 cm, 17-18 cm, 24-25 cm, and 32.5-33.5 cm). Superimposed on these small variations there are larger, more persistent, grain-size oscillations.

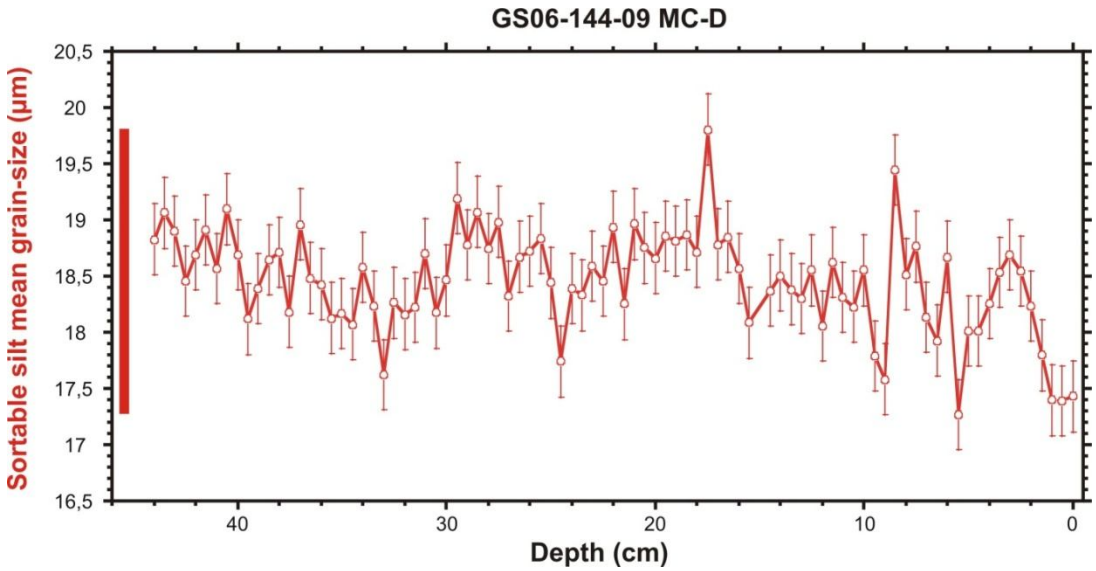

Fig. 5.1: Sortable silt mean grain-size variability down-core. The red circles are the averages of two measurements, and the thick red curve connects the points. The error bars denotes is the standard error of the mean, which is ± 0.31 µm. The thick red bar shows the range of the variability.

At least 5 persistent grain-size oscillations are visible, each lasting between ~ 3.5-9 cm. Each oscillation has roughly the same range of grain-size variability; there are oscillations from 1-5.5 cm, 5.5-9 cm, 9-15.5 cm, 15.5-24.5 cm, and 24.5-33 cm. These oscillations are intercepted, and sometimes constrained (5.5-6 cm & 8.5-9 cm) by relatively large, simple point grain-size variations. The results show that the ISOW flow vigor not only varied on longer timescales (oscillations) but also is experienced relatively abrupt excursions. In order to better quantify the significance and scale of the high frequency variations, more replicates should be analyzed over the intervals with the largest grain-size changes. However, despite potential sources of error (pipette sampling depth, processing for de-silication etc.), the grain-size variability from one data point to the next is usually relatively small (except those already discussed), and the major oscillations lasts several centimeters, hence it is likely that the oscillations reflect real and persistent changes in the ISOW vigor.

Figure 5.2 shows the averages of the two replicates (thin red curve) with a 3 point running mean (thick red curve). Smoothing of the signal removes some of the uncertainty associated with each measurement, and emphasizes lower frequency variability. Most of the pattern described in figure 5.1 is still apparent in the smoothed record. The two first oscillations each last 4.5 cm [0.5-5 cm (I) and 5-9.5 cm (II)] and have a grain-size range of ~1.1 µm (1.2 µm and 1.1 µm), while the third lasts 5.5 cm (9.5-15 cm) and has a grain-size range of ~ 0.4 µm. The fourth oscillation lasts 9 cm (15-24 cm), and has a grain-size range of ~ 1 µm, while the fifth oscillation lasts 8.5 cm (24-32.5 cm) and has a grain-size range of ~ 1 µm. Thus, except

for oscillation 3, the oscillations have very similar ranges of grain-size variability. Down-core from oscillation 5 the grain-size steadily increases towards the bottom of the core, only interrupted by a few minor perturbations.

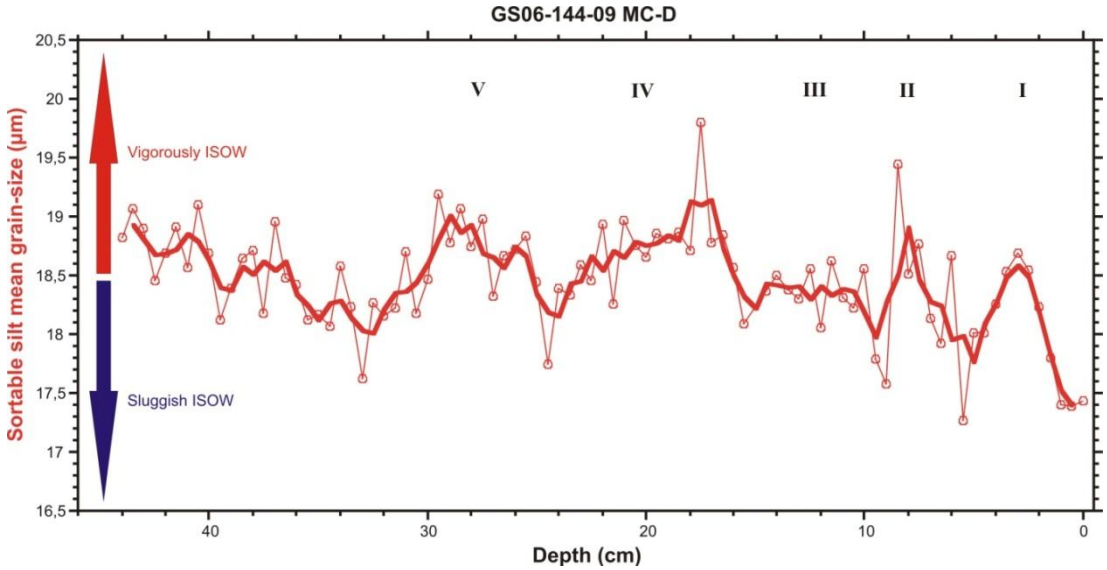

Fig. 5.2: Sortable silt mean grain-size variability down-core. The thin red curve shows the average of two replicas, which is the same curve shown in figure 5.1. The thick red curve is the 3 point smoothed average of the replicates. The numbers denotes the different grain-size oscillations.

Figure 5.1 & 5.2 has both shown that there are multiple changes in the mean grain-size of the sortable silt fraction throughout the core. There are small scale variations (0.5-1 cm), and superimposed on these, larger scale oscillations.

Plotting mean grain-size variations against depth is a good way to visualize down-core variability, but does not supply information about when specific grain-size changes occurred. Hence, the sortable silt record must be plotted against the constructed age model for core GS06-144-09 MC-D. Plotting the results against age not only gives information about the rate and duration of the flow speed changes, but also allows the changes in ISOW to be compared with results from other sources. The age model for the multicore is composed of two different dating methods (subchapter 4.2.1), which separates the age model into three segments with different sedimentation rates. Based upon the age model it takes on average ~14 years to accumulate 1 cm.

Figure 5.3 shows the average of the two replicates in conjugation with the 3 point running average (~21 years) plotted against age. The smoothed record spans the last ~600 years and shows multidecadal-centennial variability in the ISOW vigor. According to the smoothed record, the ISOW near bottom relative flow speed steadily decreases from ~1400-1520 AD,

interrupted only by a few smaller perturbations. Around 1520 AD the oldest of the flow speed oscillations begins (V). The oscillation last ~ 97 years (1521-1618 AD) and begins and ends at roughly the same relative flow speed. The next oscillations last ~ 103 years [1618-1721 AD (IV)], ~ 99 years [1721-1820 AD (III)], ~117 years [1820-1937 AD (II)], and ~59 years [1937-1996 AD (I)]. Thus, except for oscillation I, the oscillations have duration of about 100 years based upon the age model. The grain-size variations during oscillation III is rather small, thus, it is more appropriate to characterize the grain-size variations in this period as a period with slowly decreasing grain-size values.

Also shown in figure 5.3 is a thin blue dotted line which is a linear curve fit to the smoothed record (R= ~0.43), indicating that there is a long term trend towards slower ISOW flow over the core site during the last ~600 years. This long term trend cannot be caused by an analytical drift in the Coulter Counter because the samples were sampled randomly. This suggests a long term trend toward less intense ISOW flow over the last ~600 years.

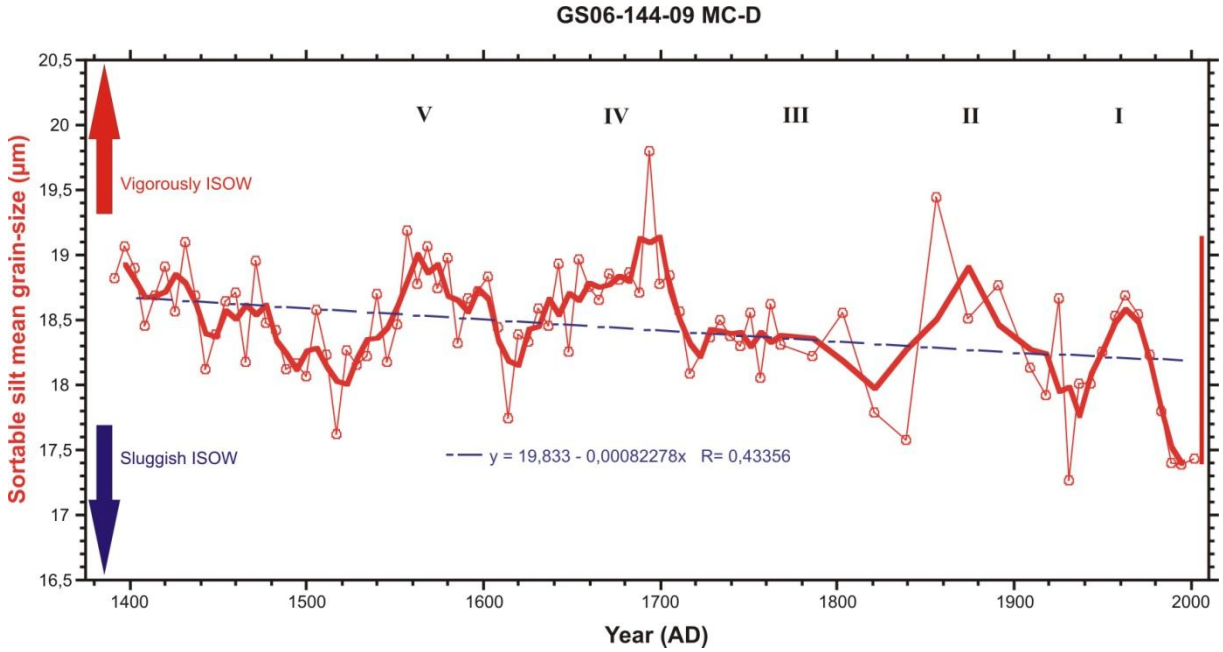

Fig. 5.3: Sortable silt mean grain-size variability over the last ~600 years. The thin red curve with data points is the averages of two replicates, while the thick red curve is the 3 point smoothed average of the thin red curve (corresponding a ~20 years running average). The thin blue dotted line is the linear curve fit constructed from the smoothed record, while the red bar on the right hand side shows the range of variability of the smoothed record. The numbers denotes the different flow speed oscillations.

Evidence supporting the hypothesis that our flow speed proxy reflects real changes in the ISOW vigor comes from a comparison with the flow speed measurements from Boessenkool et al. (2007b), on a high resolution box core collected deeper, and further south on the Gardar

drift (Fig. 5.4). Figure 5.4 shows that the variations in the two flow speed proxies are strongly similar, despite the higher resolution and deeper location of the box-core. Thus, multidecadal changes in ISOW vigor is recorded, and reproduced, using different sediment cores, under different settings.

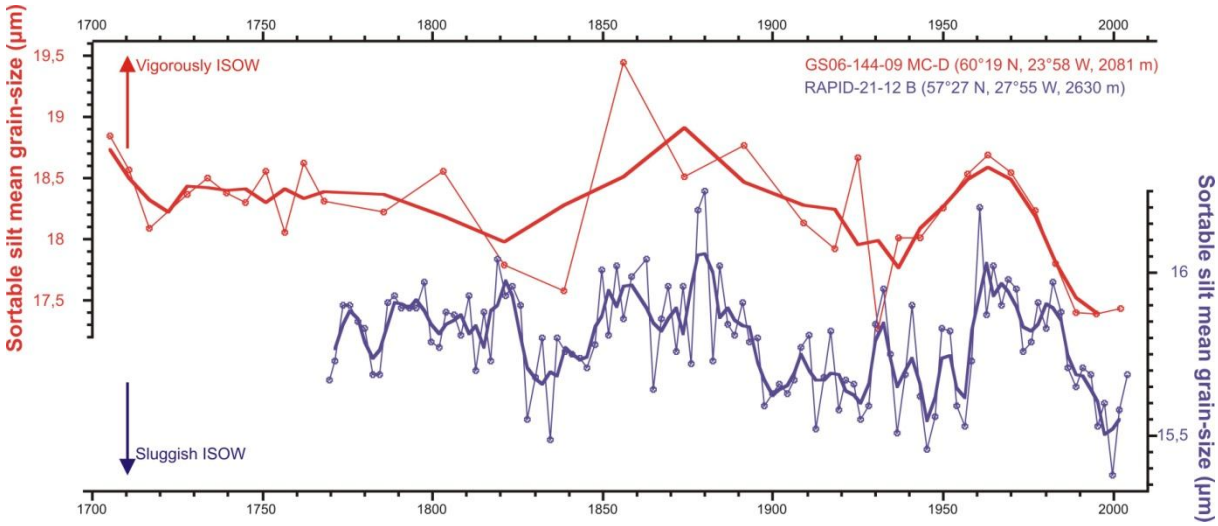

Fig. 5.4: Comparison between our proxy for ISOW vigor and Boessenkool et al. (2007) proxy for ISOW vigor. The sortable silt mean grain-size data from core GS06-144-09 MC-D is plotted in the same manner as Fig. 5.3. Each data point from the box-core (and connecting blue, thin lines) represents ~ 2 years, while the thick blue curve is a 3 point smoothed average, representing a ~6 year running average.

To summarize, the sortable silt record has shown that the ISOW vigor vary on inter-decadal timescales (variability between adjacent data points) the last ~600 years, and superimposed on these, there are multidecadal-centennial flow speed oscillations. Furthermore, the record indicates a trend over last ~600 years toward a less vigorous ISOW.

5.2 Oxygen isotope results

5.2.1 Summer near surface temperature/salinity

Figure 5.5 shows the $\delta^{18}O$ variability of *N. pachyderma* (d) in the multicore plotted against age. The figure shows the average of two replicates at each depth, in conjugation with a 5 point smooth, equivalent to a ~35 year running average. *N. pachyderma* (d) $\delta^{18}O$ variability is assumed to reflect near surface water changes (subchapter 3.4.1). Each *N. pachyderma* (d) sample was analyzed in duplicates, and reproduced well, with a standard deviation for the whole dataset of only ± 0.1 ‰, and an average standard error of ± 0.07 ‰ (2 replicates) (Appendix F). The precision of the mass spectrometer is ± 0.08 ‰; hence, the main source of uncertainty in the measurements is analytical, as opposed to environmental. Thus, individual foraminifer measurements closely represent environmental averages.

The unsmoothed record shows that there are multiple abrupt changes in $\delta^{18}O$ values throughout the record (as much as 0.29 ‰ between adjacent data points). However, from the smoothed record it is evident that superimposed on these abrupt $\delta^{18}O$ changes there are long term $\delta^{18}O$ oscillations on multidecadal to centennial timescales. From the smoothed record a trend is visible towards increasing $\delta^{18}O$ values from ~1460-1570 AD, decreasing values from ~1570-1643, increasing values from ~1643-1839 AD (interrupted by a relatively small decrease in $\delta^{18}O$ from ~1729-1763 AD), and slowly decreasing values from ~1840 AD towards modern times.

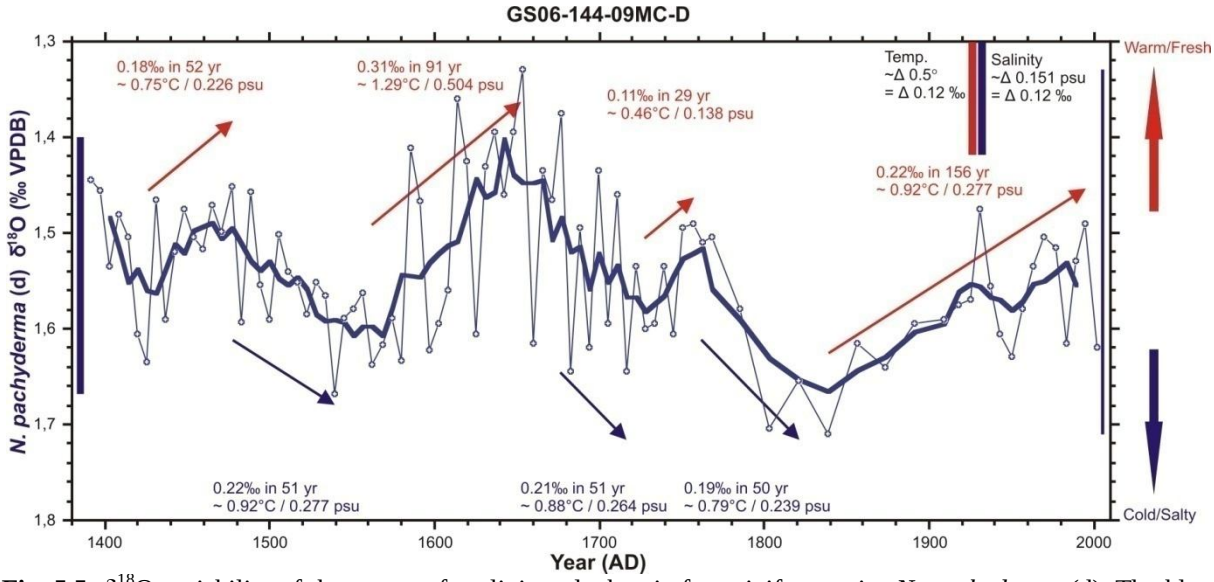

Fig. 5.5: $\delta^{18}O$ variability of the near surface living planktonic foraminifer species *N. pachyderma* (d). The blue data points are the average of two replicates, while the thin blue line connects the points. The thick blue curve is the 5 point smoothed average of the two replicates (amounts to a ~ 35 year running average). The thin blue bar on the right hand side of the curve denotes the total $\delta^{18}O$ variability of the two replicates, while the thick blue bar on left hand side denotes the total variability in the smoothed record. On the top right side of the figure there is a red and blue bar illustrating how much a $\delta^{18}O$ change of 0.12 ‰ corresponds to in temperature (equation 3.7) and salinity (Schmidt et al., 1999). The red (blue) arrows and corresponding textbox, denotes periods with decreasing (increasing) $\delta^{18}O$ values.

Changes in the $\delta^{18}O$ of foraminifers are related to changes in the temperature and salinity of the near surface water. In order to reconstruct past changes in sea-surface temperatures, paleotemperature equations have been determined. However, in order to use paleotemperature equations the $\delta^{18}O$ value of the ocean must be known, which is not a problem in modern times, but cannot be expected to be constant through time. During the last glacial maximum (LGM) the build-up of large continental ice-sheets caused the global sea-level to drop about 120 m, which caused the oceans $\delta^{18}O$ value to increase by ~1.32 ‰ (1 m drop in sea-level increases the $\delta^{18}O$ value of the ocean by ~0.011 ‰) (Fairbanks 1989). Nevertheless, the cores used in this study spans only the last ~1350 years, which is a period with relatively minor

changes in sea level. Thus, we can be fairly certain that the reconstructed $\delta^{18}O$ variability from the planktonic foraminifers used in this study is not caused by changes in sea level. Salinity changes in the near surface waters occur due to differences in precipitation and evaporation, input of freshwater from continental rivers and glaciers, and the formation of sea ice. Craig & Gordon (1965) plotted the $\delta^{18}O$ of surface water in the North Atlantic Ocean and NADW against salinity, and found a relationship where an increase of 1 psu corresponds to an increase in $\delta^{18}O$ of 0.61 ‰ (VSMOW). The study area is mainly influenced by the different branches of the relative warm and saline North Atlantic Current (Faroe Current and Irminger Current) (subchapter 2.2.1), and is located far from continental margins, hence it lacks local sources of isotopically depleted freshwater from rivers and melting glacial ice. In addition, the study area is not influenced by the fresh and cold polar waters transported by the East Greenland Current. Thus, the regional mixing line will probably be somewhat different from the North Atlantic Ocean mixing line created by Craig & Gordon (1965). Salinity and $\delta^{18}O_w$ data gathered from Schmidt et al. (1999) indicate a more appropriate regional mixing line in the study area of 0.79 ‰/psu (Appendix G). Based upon the paleotemperature equation given in subchapter 3.3.1 (Equation 3.7), and the salinity relationship, a 1 ‰ decrease in $\delta^{18}O_c$ from the different planktonic foraminifers is assumed to correspond to a warming of 4.2 °C, or a decrease in salinity of 1.26 psu.

From the start of the record (~1391 AD) the $\delta^{18}O$ values increases until ~1430 AD (Fig. 5.5). Thereafter, the values decrease towards the previously $\delta^{18}O$ minimum in only 52 years. In terms of absolute numbers, this corresponds to a $\delta^{18}O$ decrease of 0.18 ‰, which is equivalent to a warming of 0.75 °C (if solely reflecting temperature). Subsequently, the $\delta^{18}O$ values increase again, and reach a new maximum (in 51 years) at ~1540 AD, suggesting a cooling/increasing salinity of ~0.92°C/ 0.277 psu, respectively. The $\delta^{18}O$ values once again decreases, and reach the lightest values in the whole record around 1650 AD. This warming/freshening happens in only 91 years, and amounts to ~1.29°C warming if the change is caused solely by temperature. Between ~1650 AD and ~1716 AD there is an increase in the $\delta^{18}O$ values, which terminates in a period of increasing values from ~1728-1757 AD. The period from ~1760 AD to ~1840 AD, the last period with increasing $\delta^{18}O$ values in the record, is terminated by the maximum $\delta^{18}O$ values in the core at ~1840 AD. After 1840 AD, and towards modern times, the $\delta^{18}O$ values slowly decreases, interrupted only by a few minor perturbations.

G. bulloides is believed to bloom somewhere between spring and autumn, and is here considered to be a proxy for summer near surface temperature/salinity variability (subchapter 3.4.1). Similar to *N. pachyderma* (d), *G. bulloides* was analyzed in duplicates, and reproduced almost as well. The standard deviation for the whole dataset is ± 0.15 ‰, and the standard error for two replicates is ± 0.11 ‰, which is significantly higher than for *N. pachyderma* (d) (Appendix F). In addition, a recent study from the Eirik Drift measured *G. bulloides* with four replicates, and found a poor reproducibility (Johansen 2008). Thus, based on the measured low reproducibility, and the difficulties found in other studies, the *G. bulloides* record is expected to be noisier than the *N. pachyderma* (d) record.

Figure 5.6 shows the average of two replicates in conjugation with the 5 point smoothed average of the two replicates for *N. pachyderma* (d) (blue), and *G. bulloides* (grey), plotted against age. *G. bulloides* has a higher degree of variability in $\delta^{18}O$ than *N. pachyderma* (d), especially for the unsmoothed record [up to 0.48 ‰ between adjacent data points for *G. bulloides*, compared with 0.29 ‰ for *N. pachyderma* (d)], but also for the smoothed record. Even though the *G. bulloides* data has a lower reproducibility than *N. pachyderma* (d), most of the trends seen in the *N. pachyderma* (d) smoothed $\delta^{18}O$ record is visible in the *G. bulloides* smoothed record. With the exception of a $\delta^{18}O$ increase centered around ~1450 AD in the *G. bulloides* record, not apparent in the *N. pachyderma* (d) record, the two records are roughly in phase. The $\delta^{18}O$ changes in the *G. bulloides* record are, as mentioned, typically larger than similar changes in the *N. pachyderma* (d) record, perhaps due to a shallower depth habitat for *G. bulloides*, or that the species grows in a more climatologically variable season. For example, from ~1665-1730 AD the *N. pachyderma* (d) record (Fig. 5.5) describes a $\delta^{18}O$ increase of ~ 0.26 ‰, which corresponds to a increase of ~0.35‰ in the *G. bulloides* record (cooling/increasing salinity = 1.46 °C/0.440 psu).

From ~1760- 2002 AD the two records are in phase, but there are some differences. Both smoothed records show a cooling (increasing salinity) until ~1839 AD, where the *N. pachyderma* (d) starts the slow warming (freshening) toward modern times, while the *G. bulloides* record remains almost unchanged until ~1890 AD. Only after 1890 AD does the *G. bulloides* values decrease. This warming (freshening) period happens more rapidly, and has higher variability than the *N. pachyderma* (d) record (e.g. from 1937-2002 AD there is a decrease in $\delta^{18}O$ of 0.43 ‰, which amounts to a warming of 1.79 °C or a freshening of 0.540 psu). To summarize, the records of *N. pachyderma* (d) and *G. bulloides* has shown a remarkable good correlation in $\delta^{18}O$ variability over the last ~600 years, thus strengthening

the case that the measured variability reflects real changes in the physical properties of the near surface waters in the study area.

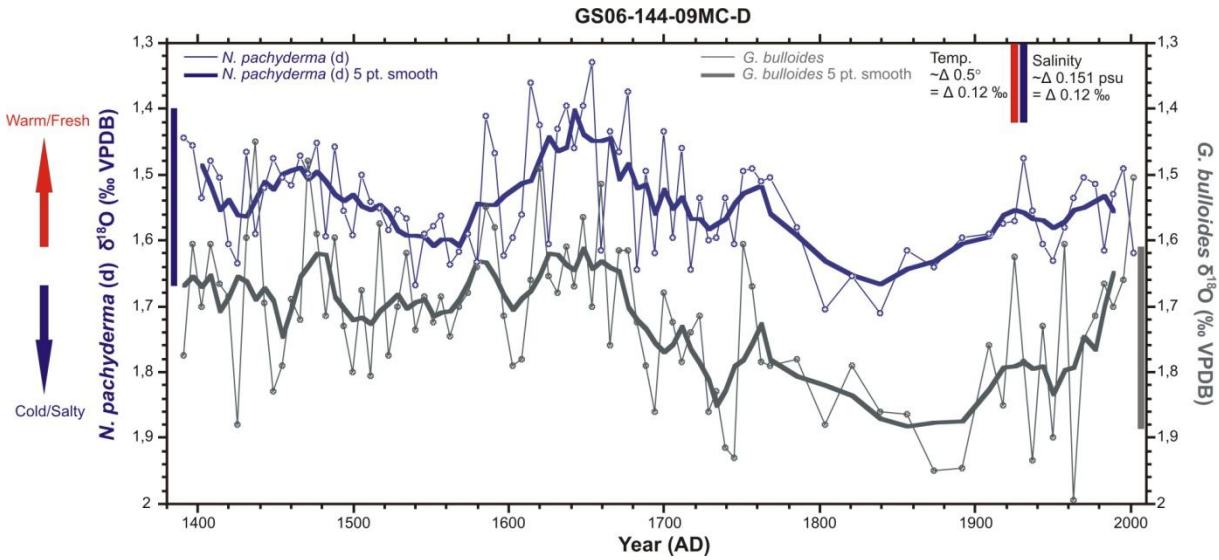

Fig. 5.6: *N. pachyderma* (d) (blue) and *G. bulloides* (grey) plotted against age. The thick grey bar at the right hand side denotes the $\delta^{18}O$ variability of the 5 point smoothed average from *G. bulloides* data points, while the blue bar on the left hand side denotes the $\delta^{18}O$ variability of the 5 point smoothed average from the *N. pachyderma* (d) data points.

5.2.2 Winter/subsurface temperature/salinity

G. inflata lives deeper than the two previously planktonic foraminifer species, and is here used as an indicator for winter/subsurface water properties (subchapter 3.4.1). As with the two previously species, *G. inflata* was analyzed in duplicates at each sample depth. The *G. inflata* $\delta^{18}O$ values reproduced well, with a standard deviation for the whole dataset of ± 0.10 ‰, resulting in an average standard error of ± 0.07 ‰ (Appendix F).

The $\delta^{18}O$ variability of *G. inflata* is plotted against age in figure 5.7. The record shows a high degree of $\delta^{18}O$ variability on short timescales; in fact, it has the highest variability between adjacent data points of the three planktonic foraminifer records (0.44 ‰). From the smoothed record it becomes evident that relatively large $\delta^{18}O$ changes have also happened on multidecadal to centennial timescales throughout the record.

From the beginning of the record and until ~1436 AD, only minor $\delta^{18}O$ changes occur. Between ~1436 AD and ~1500 AD the most rapid $\delta^{18}O$ changes in the whole core occur. First, the $\delta^{18}O$ values quickly increase from 1436-1471 AD, which amounts to a cooling (increasing salinity) of ~1.08 °C (~0.327 psu), secondly, the value rebounds to its previous value in only 23 years (1477-1500 AD), which amounts to a striking warming (freshening) of ~ 1.83°C (0.553 psu). This $\delta^{18}O$ change is actually bigger than any of the changes registered

from the *N. pachyderma* (d) record (Fig. 5.5). From 1500 AD to ~1550 AD the $\delta^{18}O$ values increase again, wherefrom the values slowly decrease until ~1630 AD (interrupted by a few minor perturbations), when the next cycle of rapid $\delta^{18}O$ changes begins. First, there is a rapid warming (freshening) period of ~1.04 °C (~0.314 psu) from ~1631-1648 AD, secondly, a rapid cooling (increasing salinity) period of ~0.50°C (~0.151 psu) from 1654-1682 AD, and thirdly, another rapid warming (freshening) period of ~0.96°C ~ (0.289 psu) from 1694-1722 AD. After 1722 AD and towards modern times, the $\delta^{18}O$ values first increase relatively rapidly until ~1751 AD, thereafter the values increase at a slower rate until ~1890 AD. From ~1890 AD to 2002 AD the record shows some minor perturbations in the values, but the mean of the signal remains practically unchanged.

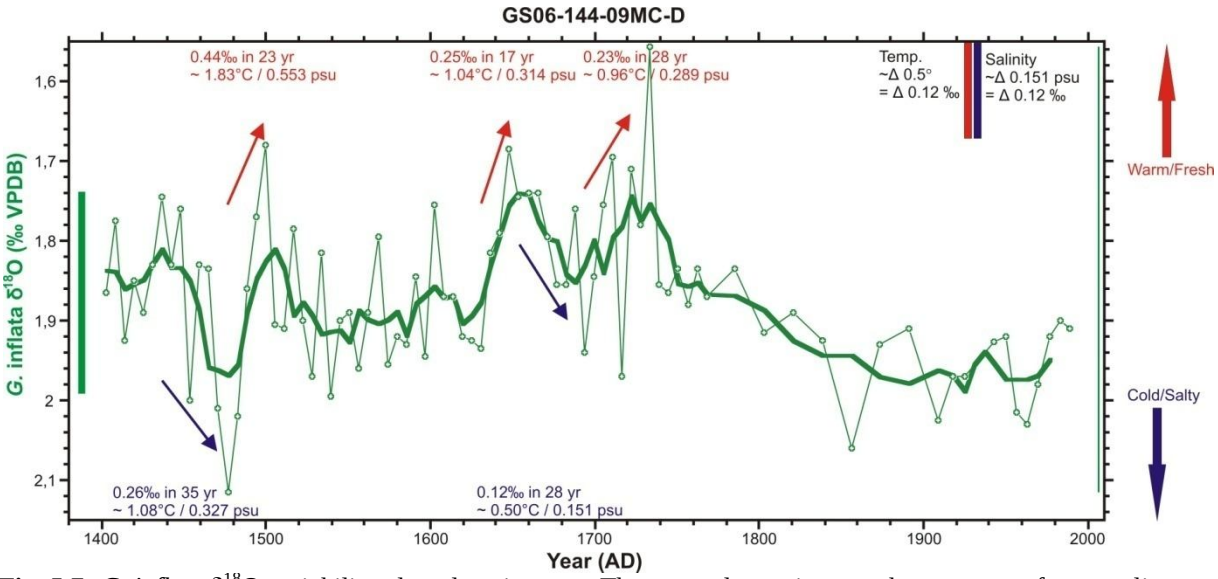

Fig. 5.7: *G. inflata* $\delta^{18}O$ variability plotted against age. The green data points are the averages of two replicates, and the thin green curve connects the points, while the thick green curve is the 5 point smoothed average of the green data points. The thin green bar at the right hand side denotes the $\delta^{18}O$ variability of the unsmoothed record, while the thick green bar at the left hand side denotes the $\delta^{18}O$ variability of the smoothed record. The red arrows denotes periods with rapidly decreasing $\delta^{18}O$ values (warming/freshening), while the blue arrows denotes period with rapidly increasing $\delta^{18}O$ values (cooling/increasing salinity).

5.2.3 Comparison between near surface temperature/salinity records

Figure 5.8 shows the records of $\delta^{18}O$ for *N. pachyderma* (d), *G. bulloides*, and *G. inflata* plotted against age. The *N. pachyderma* (d) and *G. bulloides* records have already been compared (subchapter 5.2.1), and will now be compared with the deeper dwelling *G. inflata*. The *N. pachyderma* (d) and *G. inflata* records are out of phase almost throughout the core. However, there are some in phase relationships. Both smoothed records show increasing $\delta^{18}O$ values from ~1505-1570 AD and both have the $\delta^{18}O$ core minimum situated in the 17th century. Furthermore, both records show increasing $\delta^{18}O$ values from ~1760-1840 AD. After

~1840 AD, and throughout the record, *N. pachyderma* (d) and *G. inflata* are almost completely anti-phased (light pink boxes in Fig. 5.7). The *G. bulloides* and *G. inflata* records are also out of phase for the most part of the core. In fact they are sometimes in complete anti-phase (yellow boxes in Fig. 5.8). In phase relationships occurs from ~1760-1860 AD. All three planktonic foraminifer records are actually in phase in the period from ~1760 AD to ~1840 AD. In summary, the shallow living foraminifers [*G. bulloides* and *N. pachyderma* (d)] and the deeper dwelling foraminifers (*G. inflata*) show evidence of somewhat decoupled variability, suggesting both periods of uniform water column changes and shorter episodes indicating dramatic changes in surface stratification.

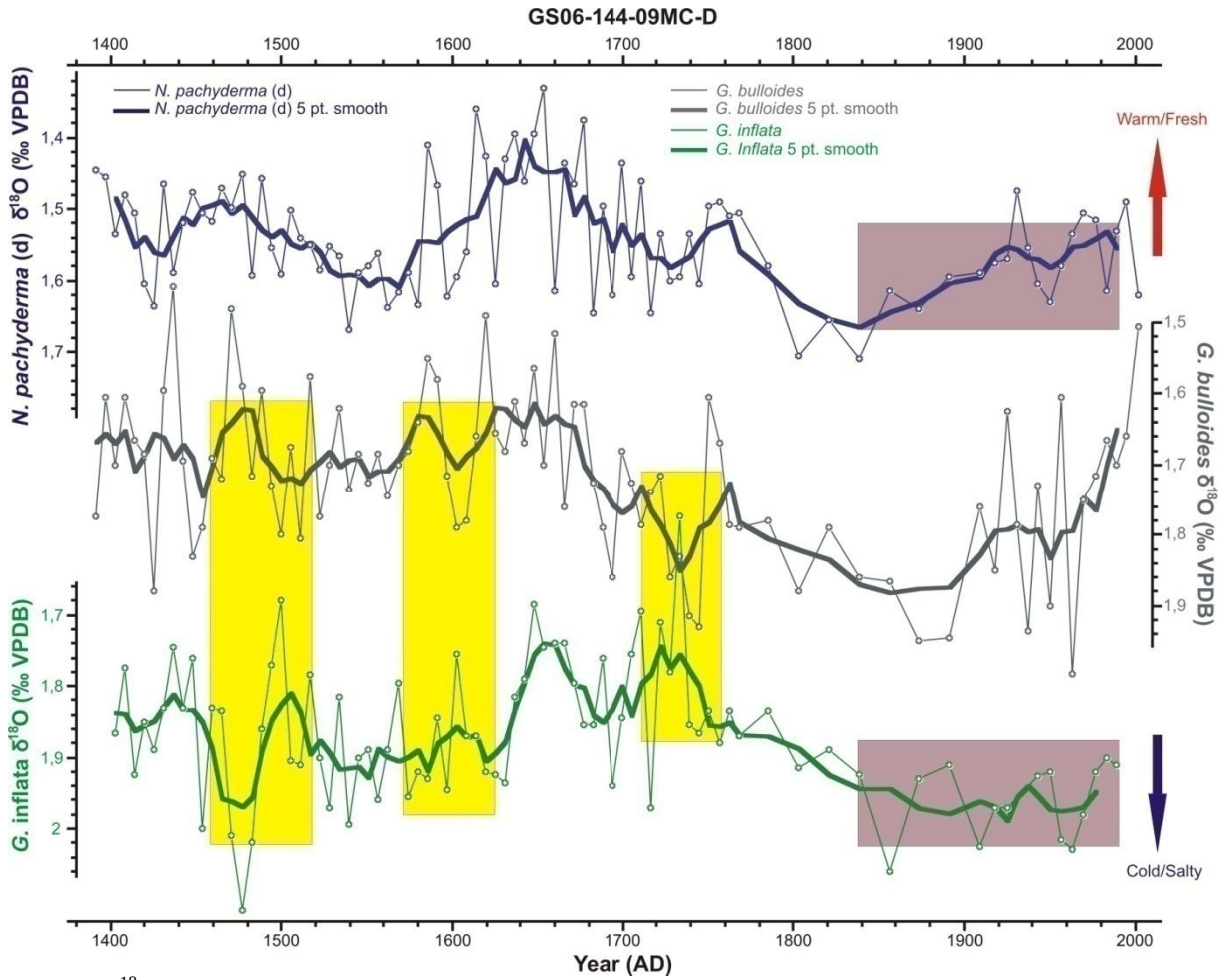

Fig. 5.8: $\delta^{18}O$ variability for the three planktonic records plotted against age. The yellow boxes denote periods where the *G. bulloides* and *G. inflata* smoothed records are clearly anti-phased. The light pink boxes denote periods when the *N. pachyderma* (d) and *G. inflata* smoothed records are mostly anti-phased.

5.2.4 Summer temperature/salinity variability from the gravity core

We extend the record of surface ocean property changes beyond 1400 AD using $\delta^{18}O$ record of *N. pachyderma* (d) from the gravity core GS06-144-08 GC. Figure 5.9 shows the $\delta^{18}O$ variability of *N. pachyderma* (d) from the multicore and the gravity core plotted against the combined age model for the two cores (subchapter 4.2.2). The combined *N. pachyderma* (d) record spans from ~660 to 2002 AD. The standard deviation for the *N. pachyderma* (d) gravity core replicates is ± 0.12 ‰ and the average standard error is ± 0.085 ‰ (2 replicates), which is a little more than for the multicore (Appendix F). Similar to the multicore, this record show relatively large $\delta^{18}O$ variability between adjacent data points (0.36 ‰ maximum for the gravity core and 0.38 ‰ for the multicore). On the other hand, the down core variability from the smoothed record is less compared with the *N. pachyderma* (d) record from the multicore (0.12 ‰ for the gravity core and 0.26 ‰ for the multicore). This is probably caused by the fact that the gravity core is sampled at every cm (the multicore is sampled at every 0.5 cm), hence when constructing a 5 point smooth, twice the amount of time is smoothed compared with the multicore core, which results in a lower variability. The smoothed (~75 year running average) record of $\delta^{18}O$ shows an oscillatory pattern between ~660 AD and ~870 AD, while during the following 170 years (~870-1040 AD), the $\delta^{18}O$ values remains relatively stable. During the next 330 years (~1040-1370 AD), there is a trend of decreasing $\delta^{18}O$ values from ~1042-1237 AD (~0.54°C/0.164 psu), followed by increasing values from ~1253-1358 AD (~0.67°C/0.201 psu). Thereafter, the $\delta^{18}O$ values once again decrease, and in only 92 years (~1373-1465 AD) the values drop 0.26 ‰, which amounts to a warming of ~1.04°C if the change is caused solely by temperature. After ~1400 AD, the gravity core record overlaps with the multicore. Despite a lower resolution of near surface hydrography changes in the gravity core, the multidecadal hydrographic cycles observed in the multicore is reproduced using a separate sediment sequence with its own age model. This provides a strong verification of both our near surface proxy records, and our age models. The brief decoupling of $\delta^{18}O$ records at the bottom of the multicore (~1400-1420 AD) may be due to coring problems (e.g. re-coring/disturbance/bioturbation of the base of the multicore), or that the event was not captured in the lower resolution gravity core record.

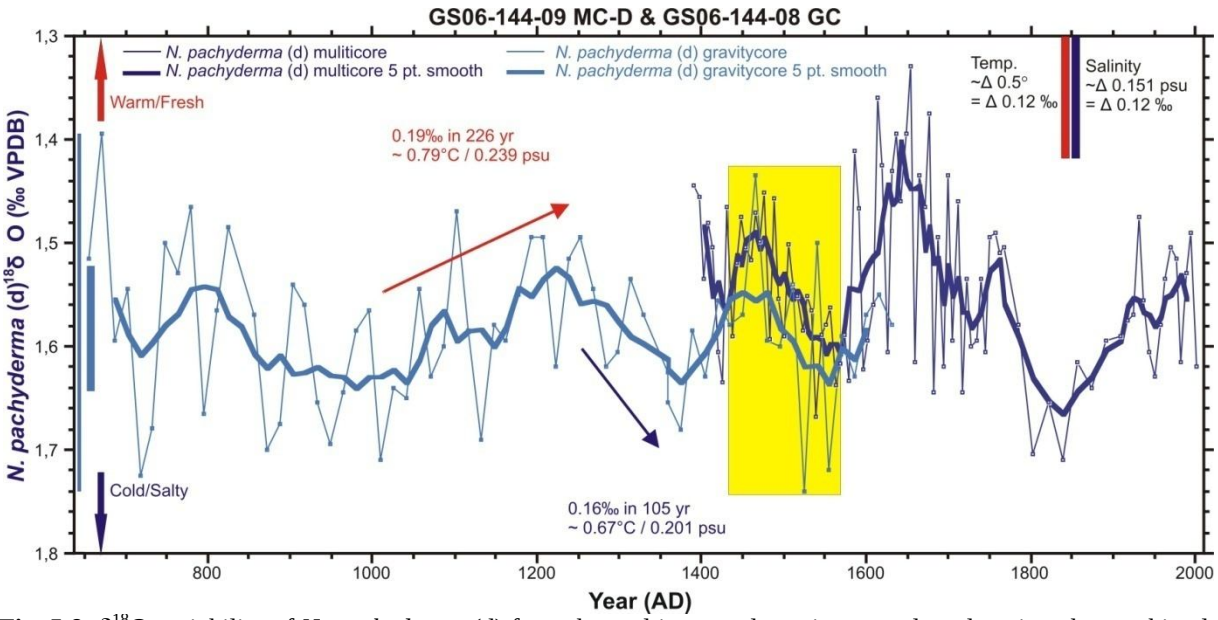

Fig. 5.9: $\delta^{18}O$ variability of *N. pachyderma* (d) from the multicore and gravity core plotted against the combined age model. The dark blue curves are the average of two replicates from the multicore (thin dark blue) in conjugation with the 5 point smoothed average of the replicates (thick dark blue), while the light blue curves are the average of two replicates from the gravity core (thin light blue) in conjugation with the 5 point smoothed average of the replicates (thick light blue). The thin and thick light blue bars on the left hand side denote the variability in the gravity core of the unsmoothed and smoothed record, respectively. Red arrows denotes periods with increasing $\delta^{18}O$ values, while blue arrows denotes periods with decreasing $\delta^{18}O$ values. The yellow box highlights the overlap between the two cores.

5.2.5 Deep water masses

Oxygen isotopic reconstructions from benthonic foraminifers provide information about temperature and salinity changes in the deep ocean. The cores used in this study, collected at 2081 m water depth at the Gardar Drift, are ideally situated to study physical and chemical changes in the ISOW. Oxygen and carbon isotopic reconstructions have been measured from the benthonic foraminifer species *C. wuellerstorfi*. Unfortunately, specimens of *C. wuellerstorfi* was almost absent from the multicore, hence the results from that core will not be used in this study. Fortunately, benthonic specimens where more abundant in the gravity core, and it was possible complete a nearly continuous isotope record of the core (top 62 cm of core GS06-144-08 GC). The standard deviation for *C. wuellerstorfi* replicates is ± 0.1 ‰ and the standard error for intervals with two replicates is ± 0.07 ‰ (Appendix F).

Figure 5.10 shows the $\delta^{18}O$ variability for *C. wuellerstorfi* in the gravity core plotted against age. Due to the scarcity of *C. wuellerstorfi* specimens, there are some depth intervals in the core between ~687-779 AD and ~1160-1630 AD without any measurements, hence the smoothed record in these intervals represents longer periods than the rest of the core. This applies especially for the interval ~702-779 AD, ~1359-1419 AD, ~1465-1510 AD, and

~1570-1631 AD. Furthermore, because we do not have a complete data set for *C. wuellerstorfi* the smoothed record is here represented by a 3 point smoothing.

The total $\delta^{18}O$ variability of both the unsmoothed (0.53 ‰) and smoothed (0.36 ‰) record is higher than the similar record of *N. pachyderma* (d), which is 0.36 ‰ and 0.12 ‰, respectively. The record appears noisier than previously presented records, nevertheless trends are apparent. From the smoothed record the values increase between ~750AD and ~810 AD, and decrease between ~810 AD and ~890 AD. Between ~890 AD and ~1010 AD the smoothed record indicates fairly constant values, while some abrupt, relatively minor $\delta^{18}O$ changes occur between ~1010 and 1130 AD. Thereafter, the smoothed record indicates abrupt changes from 1130 ~AD to ~1180 AD. If these changes are real, it would amount to a temperature change of ~ 1.8°C and/or 0.54 psu. From ~1180 AD to ~1330 AD there is a trend in the smoothed record of relatively slowly decreasing values, followed by a more abrupt increase back to the previous $\delta^{18}O$ values. During the following ~100 years the values slowly decrease, while from ~1430 AD and throughout the record there is a trend towards slowly increasing values.

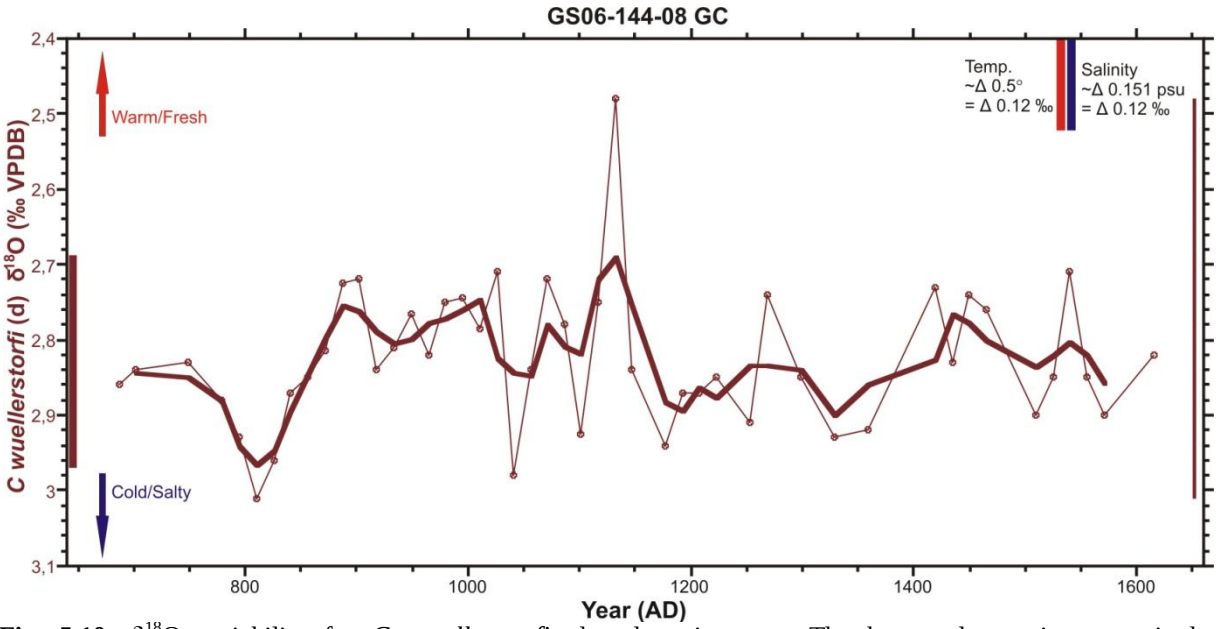

Fig. 5.10: $\delta^{18}O$ variability for *C. wuellerstorfi* plotted against age. The brown data points are single measurements, or the average of two replicates when enough specimens where available. The thin brown line connects the points, while the thick brown curve is the 3 point smoothed average of the data points (~43 year running average). The thin brown bar on the right hand side denotes the variability between adjacent data points, while the thick brown bar on the left hand side denotes the variability of the smoothed record.

5.2.6 Planktonic versus benthonic oxygen isotope record from the gravity core

Figure 5.11 shows the $\delta^{18}O$ record of *N. pachyderma* (d) (light blue) and *C. wuellerstorfi* (brown) from the gravity core plotted against age. The variability in the benthonic record is higher than in the planktonic. Throughout the records no clear, or systematic, relationship exists between surface and deepwater records. This suggests that local deepwater physical property changes are not systematically coupled to local changes in surface hydrography. The deepwater that flows over the core site was produced in the Nordic Seas, thus it is not unexpected that the two records do not co-vary. Interestingly, the fact that the deepwater record shows a higher variability than near surface record, indicates that large physical property changes has occurred in the deepwater formation sites, or due to mixing and entrainment, during the period from ~690 AD to ~1615 AD.

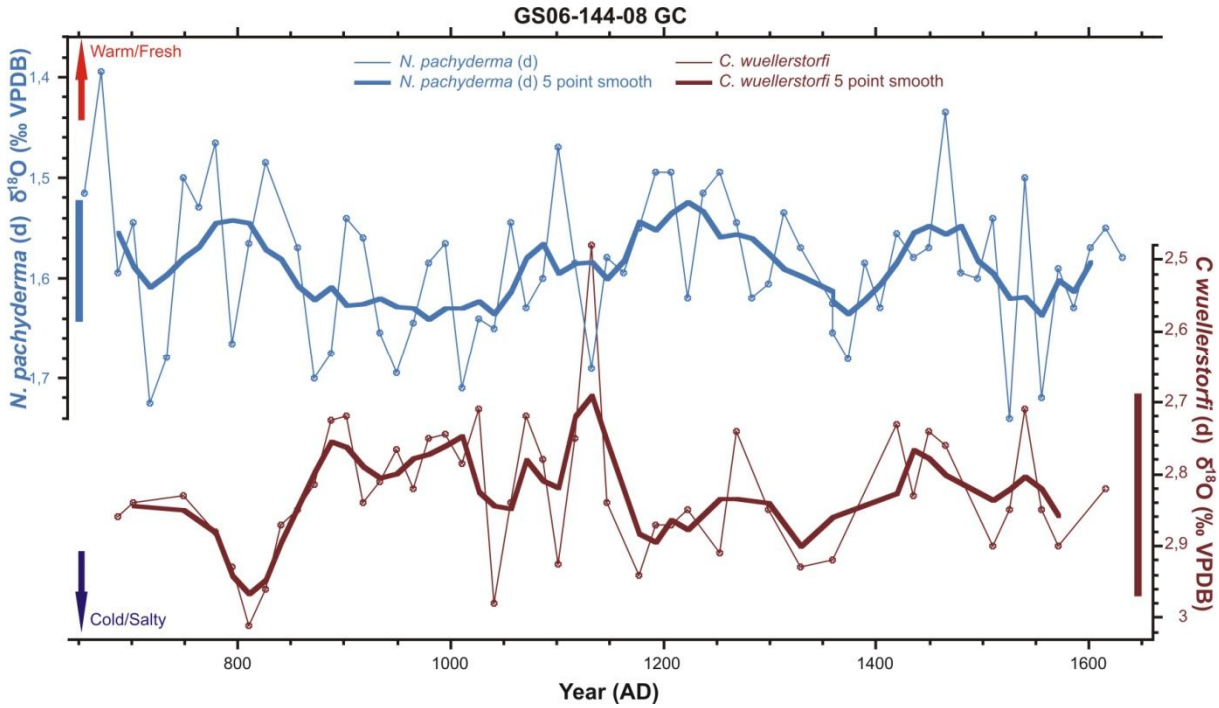

Fig. 5.11: Planktonic versus benthonic oxygen isotope record from the gravity core. The light blue bar on the left hand side denotes the $\delta^{18}O$ variability of *N. pachyderma* (d) for the smoothed record, while the brown bar on the right hand side denotes the $\delta^{18}O$ variability of *C. wuellerstorfi* for the smoothed record. Note the different scales between the two records.

5.3 Carbon isotope results

Down core changes in the carbon isotope content ($\delta^{13}C$) of benthonic foraminifera are extensively used for paleoceanography and paleoproductivity studies (Cooke & Rohling, 2001, and references therein) (subchapter 3.3.2). From both cores, all specimens of the benthonic species *C. wuellerstorfi* were picked in order to reconstruct past changes in $\delta^{13}C$. Unfortunately, as outlined in subchapter 5.2.5, the multicore contained very few specimens of

C. wuellerstorfi. Hence, the $\delta^{13}C$ data set for the multicore is considered to be uncertain, and is not used in this study. The $\delta^{18}O$ variability of *C. wuellerstorfi* from the gravity core has already been shown (subchapter 5.2.5), and the same dataset are used to reconstruct $\delta^{13}C$ variability. *C. wuellerstorfi* is known to build its test in near equilibrium with dissolved inorganic carbon (DIC) of the bottom waters, thus it is a good indicator for measuring past changes in $\delta^{13}C_{DIC}$ (Graham et al., 1981; Grossman 1987; Wefer & Berger, 1991) (subchapter 3.4.2). Pre-anthropogenic values of $\delta^{13}C$ in the bottom water at the study area are ~1.2 ‰ (pers. comm. U. S. Ninnemann).

5.3.1 Benthonic carbon isotope results from the gravity core

Figure 5.12 shows the $\delta^{13}C$ variability from the gravity core. Most of the data points represent single measurements, while some represents the average of two replicates. Increasing $\delta^{13}C$ values indicate a stronger influence of ISOW over the core site, and low nutrient values (subchapter 3.3.2), while decreasing $\delta^{13}C$ values indicates a stronger influence of deepwater from the Southern Ocean (AABW), and higher nutrient levels. Throughout the record there are multiple abrupt, relatively large, $\delta^{13}C$ fluctuations, with variations as much as 0.62 ‰ between adjacent data points (~1115-1131 AD). Thus indicating that rapidly changes in the chemical properties of the deepwater flowing over the core site has occurred repeatedly throughout the record. Despite the rapid fluctuations, the $\delta^{13}C$ values exceed the modern NADW values only occasionally.

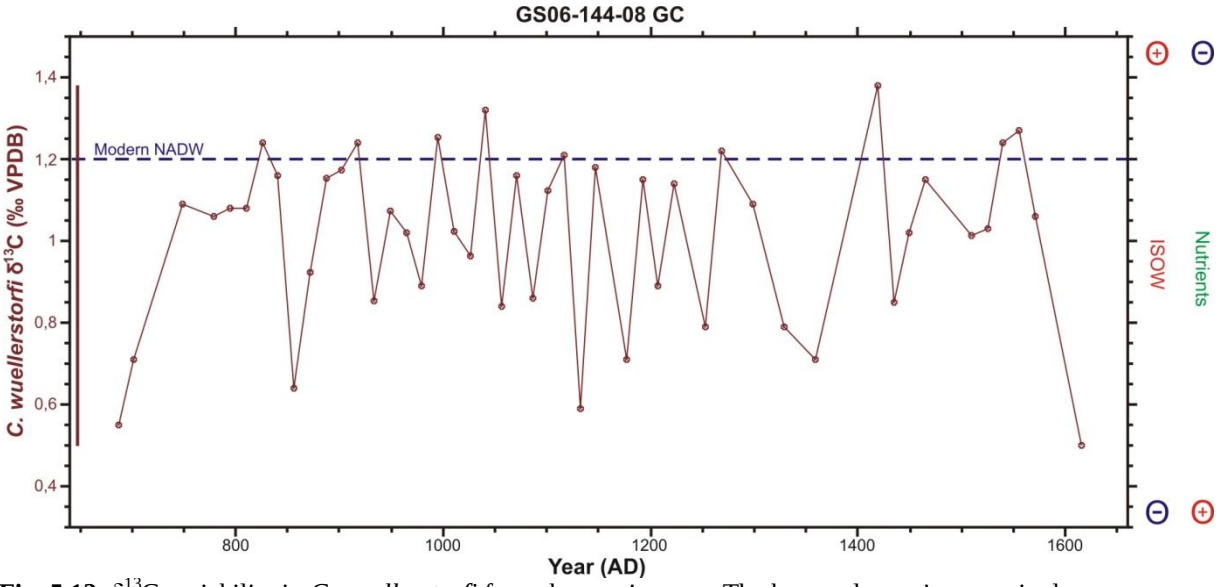

Fig. 5.12: $\delta^{13}C$ variability in *C. wuellerstorfi* from the gravity core. The brown data points are single measurements, or the average of two replicates when enough specimens where available, and the thin brown line connects the data points. The brown bar on the left hand side denotes the variability of the record, while the red stippled line indicates modern NADW values.

6. DISCUSSION

6.1 Evaluation of the sortable silt mean grain-size results

The sortable silt paleocurrent record from the multicore show that the mean flow speed over the core site has varied on multidecadal to centennial timescales over the last ~600 years. During this period the sortable silt record shows a remarkable covariance with the tree ring based AMO (Atlantic Multidecadal Oscillation) reconstructions from Gray et al. (2004), on both multidecadal and centennial timescales (Fig. 6.1). Except from 1567 AD to ~1620 AD, and ~1910-1990 AD, the two records are in close agreement. This close covariance between variations in the eastern Nordic Seas overflow and basin-wise climate (SST) strongly suggests that variations in deep circulation and AMO are tightly linked on multidecadal time scales, with increases in basin wide temperature associated with periods of vigorous ISOW.

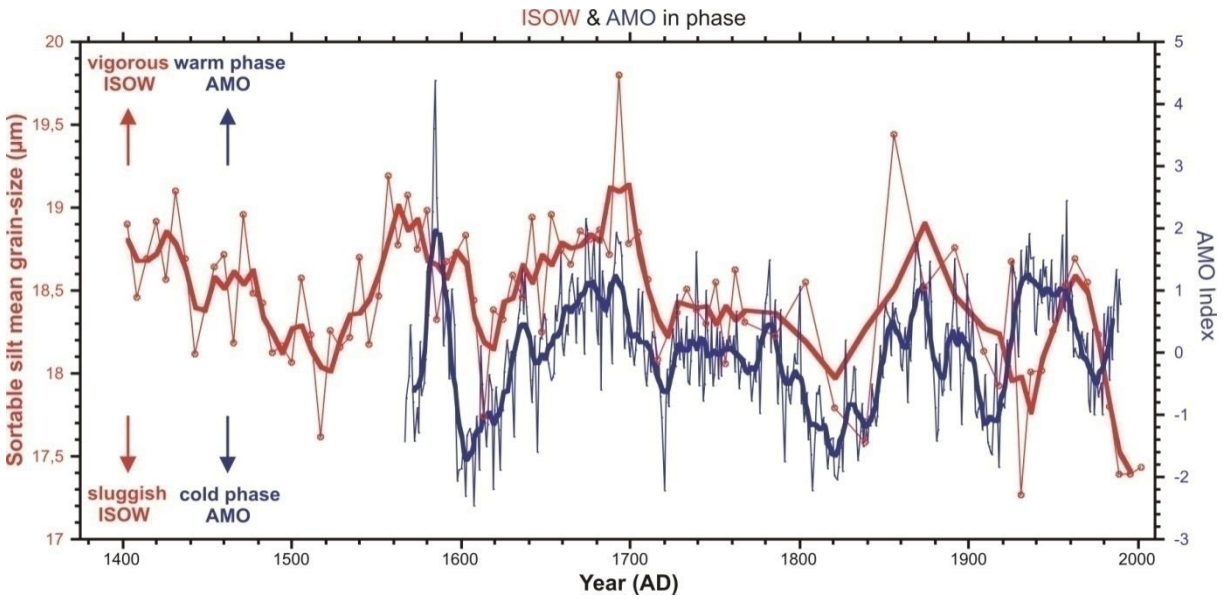

Fig. 6.1: Sortable silt mean grain-size variability in phase with AMO reconstructions. The thin red curve, and corresponding red data points, are the average of two replicates, while the thick red curve is the 3 point smoothed average of the two replicates. The thin blue curve is annual sea surface temperature (SST) anomalies, while the thick red curve is a 10 year running mean of the SST anomalies. A positive AMO value infers warmer SST than average, and vice versa. The AMO data are from Gray et al. (2004).

In the simplest sense, this ocean-climate coupling supports the hypothesis that AMO involves, and is potentially driven by, variations in the AMOC. However, this conclusion depends on both the specific nature and general representativeness of the deep circulation changes: Do changes in the ISOW vigor, or position, relative to our core site represent changes in AMOC? One possibility is that the reconstructed grain-size variations reflects vertical migrations in the

ISOW flow due to climate related shifts in subpolar hydrography (i.e. subpolar dynamics). McCave and Hall (2006), found that today the ISOW flow is constrained between 2000-2600 m water depth, and that there was no indication that LSW interacted with the sediments on the upper Gardar drift where out cores are located (2081 m). Even with significant changes in the core density and/or flux of ISOW, at 2000 m depth, the core of ISOW is unlikely to migrate significantly upslope or off the bottom topography, which constrains and guides its downslope path, at least until it approaches equilibrium densities (i.e. ~2600 m). For instance, the close coupling between our flow speed variability and Boessenkool et al. (2007) flow speed variability from the more southerly and deeper (~2600 m water depth) site on the Gardar drift, suggests that the core of the sediment laden ISOW does not migrate significantly. The persistently high sedimentation rates at our site provide further evidence that the site was located near the core of the sediment laden ISOW throughout the last ~1500 years. Typical pelagic sedimentation rates in regions without sediment focusing by currents is on the order of a few centimeters per thousand years (Pinet 2006). In the region close to our site, Bianchi & McCave (2000) measured a sedimentation rate of 21 cm/yr^{-1} during the Holocene period due to sediment focusing by the ISOW, while we estimated a sedimentation rate of ~68 cm/yr^{-1} based on the combined age model for the two cores (subchapter 4.2.2). The consistently high sedimentation rates at our site indicate that the core of the sediment laden ISOW remained close to the core site throughout the last 1500 years. Indeed, the persistently high sedimentation rates across the Gardar drift over glacial-interglacial cycles (Jansen et al., 1996), suggests that the ISOW does not migrate significantly over much larger climate cycles. Furthermore, as outlined in chapter 4.5, drift sites are locations where the measured paleocurrent are likely to reflect changes in the mean flow, rather than the variability of it. Thus, the measured paleocurrent variability most likely indicates real changes in the mean flow of the eastern branch of the Nordic Seas overflows (ISOW).

The close coupling between ISOW and basin-wide climate (SST) demonstrates clearly that the AMO involves, and is linked to variability in the circulation of the deep limb of the AMOC. This is consistent with the hypothesis that AMOC drives the AMO (Kerr 2000; Kerr 2005), provided that the ISOW variations are representative of total AMOC. If the ISOW variability represents the total AMOC, increasing (decreasing) AMOC would increase (decrease) the northward heat transport in the near surface waters, which would cause a warming (cooling) of the North Atlantic region. This relationship is identical to that seen in the close match between ISOW and AMO. However, ISOW is only one branch of the deep

overturning, and ISOW variability may be offset by compensating changes in the other branches of the NADW. For instance, increasing production of ISOW could be balanced by decreasing production of DSOW or LSW, resulting in no net change in the AMOC production. This possibility could be assessed by mean sortable silt reconstruction from the western branch of the Nordic Seas overflows (DSOW).[6] Conversely, the ISOW flow speed changes could be driven by the AMO. However, this is not the relationship we see. With increasing northward heat transport the Nordic Seas would become warmer, which would decrease the density in the surface waters, and reduce deepwater formation. Thus, if the AMO was controlling the intensity of the eastern branch of the Nordic Seas overflows via thermally driven density changes, one would expect high basin-wide SST to correspond to a weak overflow. Thus, given the observed ISOW-AMO relationship, an ocean driven climate signal is most consistent with the data. The in phase relationship between ISOW and AMO for the most part of the record, without any significant lag, is also in agreement with a ocean driven climate signal. The oceans has a long response time to changes, thus with a climate driven overturning, one would expect the overturning to lag the basin-wide climate changes several years, or even decades.

In the youngest part of the core the AMO-ISOW coupling appears to break down (Fig. 6.1). The structure of variability is strongly similar in both records, but the tight phasing apparent in the rest of the record is absent from the top. Although the phase offset could mean that ISOW changes began to lag AMO variability in the 20th century, age model uncertainty is the most likely reason for the phase offset at the top of the core. Both cores used in this study show traces of bioturbation (subchapter 3.1.2), which could potentially affect the age model. From figure 6.1 it is evident that the two records are out of phase from 1910-1990 AD. Our age model in this interval is based upon ^{210}Pb dating, and the correlation between the lead dates and the AMS ^{14}C dates are not ideal (subchapter 4.2.1). Recently, lead dates from the complementary study in the Eirik drift (Johansen 2008) were disregarded because of poor correlation between the ^{210}Pb and ^{14}C dates, and the possibility for downcore transport of unsupported lead due to bioturbation. The lead dates from the multicore used in this study could potentially suffer from similar problems. From the radiocarbon dates we know that the top of the multicore is younger than ~1950 AD (i.e. bomb ^{14}C). However, we do not know how much younger, thus, there is a possibility that the mean age of the core top is older than

[6] While measurements of DSOW flow speed changes are not yet available, δ^{13}C reconstructions are, and a comparison will be shown in chapter 6.2.

the assumed age of 2002 AD. If so, this would explain why the AMO reconstructions and the ISOW flow speed are out of phase from ~1910-1990 AD. For instance, an alternative top age of ~1980 AD (~midway between 1950 and 2002, our bracketing possibilities) gives a much better phase match (Fig. 6.2).

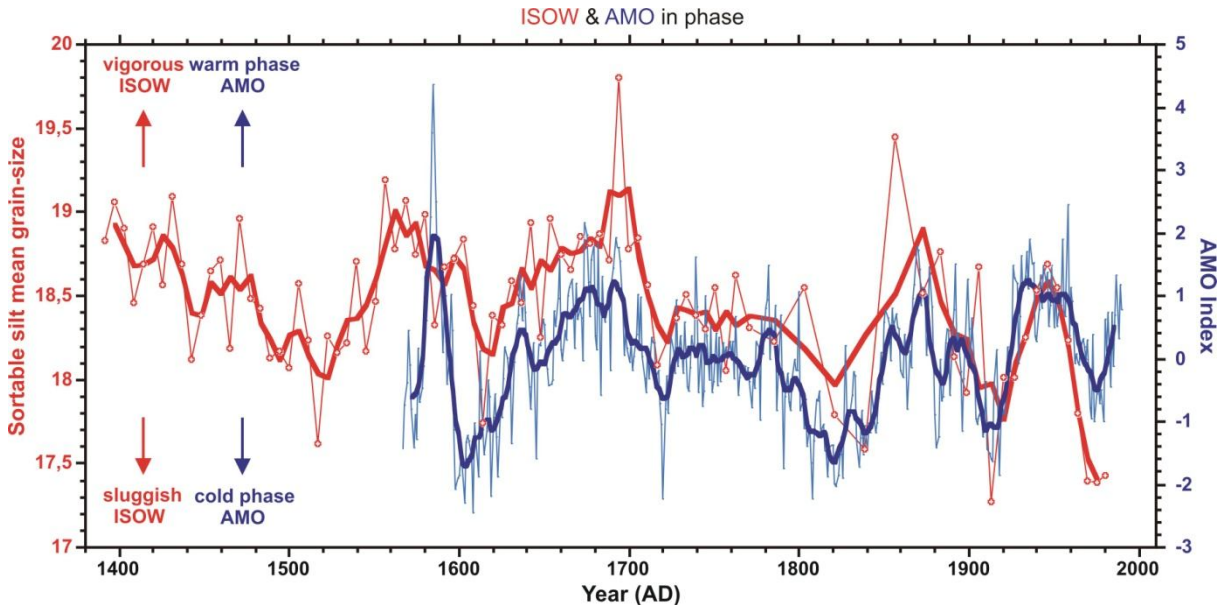

Fig. 6.2: Sortable silt mean grain-size variability in phase with AMO reconstructions. The thin red curve, and corresponding red data points, are the average of two replicates, while the thick red curve is the 3 point smoothed average of the two replicates. The thin blue curve is annual sea surface temperature (SST) anomalies, while the thick red curve is a 10 year running mean of the SST anomalies. In this figure the core top is assumed to be ~1980 AD. The AMO data are from Gray et al. (2004).

Figure 6.2 states clearly that with an alternative core top age of ~1980 AD, the in phase relationship between ISOW and AMO is apparent even in the youngest part of the record, thus strongly suggesting that our core top is younger than assumed. The in-phase relationship between ISOW and AMO is also confirmed from spectral analysis (pers. comm. U. S. Ninnemann) (Appendix K).

6.2 Comparison between kinetic and chemical deepwater changes

The benthonic carbon isotope record provides an additional, and independent, line of evidence that the deep circulation changed in phase with the AMO. Figure 6.3 shows the sortable silt mean grain-size variability and the $\delta^{13}C$ variability of *C. wuellerstorfi* from the gravity core, plotted against age. Despite using two different cores with their own age models, the measured flow speed variations from the multicore covaries with reconstructed $\delta^{13}C$ values from the gravity core. As outlined in subchapter 5.3.1, high values of $\delta^{13}C$ indicates a strong influence of low nutrient Nordic Seas overflow water (ISOW) at the core site, and are associated with strong near bottom flow speeds, while lower values of $\delta^{13}C$ indicate a stronger

presence of deepwater from a southerly origin (LDW, containing relative high amounts of AABW, subchapter 2.2.2), consistent with lower near bottom flow speed, due to reduced influence (flux) of ISOW. Thus, since the reconstructed variations in ISOW flow vigor from the multicore is supported in the $\delta^{13}C$ paleocirculation proxy from the gravity core, it supports the hypothesis that these changes represent real changes in the bottom water circulation. Throughout the gravity core record the $\delta^{13}C$ proxy shows multiple abrupt fluctuations in the values, but only occasionally do they exceed the pre-anthropogenic NADW $\delta^{13}C$ values close to the core site. About 50 % of the measurements are within ± 0.3 ‰ from the modern values (pre-anthropogenic), while all of the values deviating more than 0.3 ‰ are lower than modern $\delta^{13}C$ values. This indicates that the $\delta^{13}C$ values of modern NADW are near their long-term maximum over the length of the record, implying that the influence of eastern Nordic Seas overflows are as strong as they have been during the past ~1350 years. However, the trend observed in the paleocirculation proxy towards lower flow speeds over the past ~600 years contradicts these finding. This could mean that it is not possible to infer a one-to-one relationship between the two proxies. To evaluate the relationship between the sortable silt mean grain-size proxy, $\delta^{13}C$, and ISOW further, and validate that the measured variability in $\delta^{13}C$ represents real changes in the properties of ISOW, flow speed measurements should be undertaken for the gravity core. To summarize, figure 6.3 has shown that both the intensity and chemical properties of ISOW has varied on multidecadal to centennial timescale over the last ~1300 years.

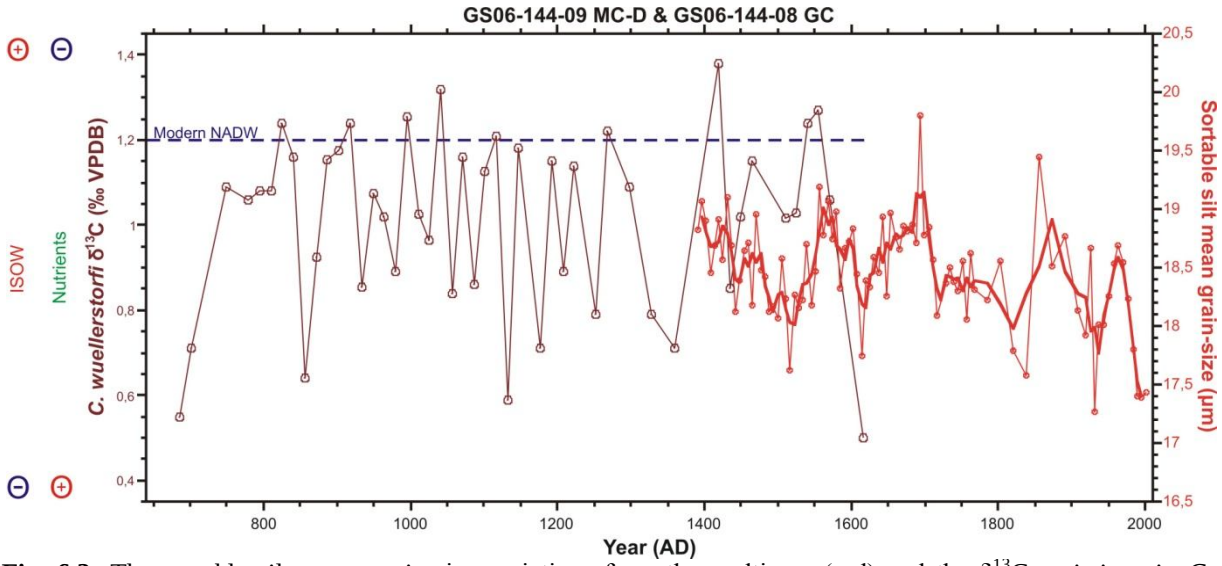

Fig. 6.3: The sortable silt mean grain-size variations from the multicore (red) and the $\delta^{13}C$ variations in *C. wuellerstorfi* from the gravity core (brown) plotted against age. Shown in red is the average of two sortable silt replicates (thin line with corresponding data points) and a 3 point smooth (thick line), while the brown data points are $\delta^{13}C$ measurements of single foraminifera (or the average of two measurements when enough specimens where available).

In chapter 6.1 a question was posed: Do the changes in the properties of the ISOW represent changes in the total AMOC? Flow speed variability from the eastern branch of the Nordic Seas overflow water (DSOW) is not yet available, but previously the chemical properties of the combined overflows (DWBC) was reconstructed from a core collected at the Eirik drift south of Greenland (Johansen 2008). Figure 6.4 shows a comparison between the changes in the properties of the ISOW (this study) and the DWBC, plotted together with the Northern Hemisphere temperature anomaly reconstructions of Mann & Jones (2002; 2003). Although the age model uncertainties preclude decisive core to core comparison, there are periods indicating coeval changes in both branches of the Nordic Seas overflows. There are periods with strong overflow (high influence of Nordic Seas overflow water over the core sites) at ~750 AD, ~960-1120 AD, ~1270-1300 AD, ~1390-1420 AD, and ~1850-1880 AD, and periods with slower overflow (low influence of Nordic Seas overflow water at the core sites) at ~680-700 AD, ~900-930 AD, ~1330-1360 AD, and ~1450-1480 AD. This suggests that the eastern branch of the Nordic Seas overflows was for the most part decoupled from the western branch over the past ~1300 years, while some the largest episodes with high (low) ISOW flow speed and/or strong (weak) influence of ISOW over the core site involved both overflowing branches.

From figure 6.4 it is evident that the AMOC, here represented by the Nordic Seas overflows, have varied on multidecadal to centennial timescales over the last ~1300 years. During this period, there are two climatic events proposed to be affected by changes in the AMOC, the Medieval Warm Period (MWP) and the Little Ice Age (LIA) (subchapter 1.2.1).

Mann & Jones (2003) ascribe the MWP to the moderately warm interval in the Northern Hemisphere between 800 and 1400 AD. In figure 6.4, the period from 960-1120 AD, where both overflowing branches indicate vigorously overflow, the SST anomaly reconstructions indicate the occurrence of one of the warmest period during the last ~1350 years. Thus, for this particular period, it is plausible that the strong AMOC at that time contributed to the observed warming.

Lund et al. (2006) measured decreased transport in the Gulf Stream during the LIA (~1250-1850 AD), consistent with several paleoclimatic records showing temperature minima's during this period. Lund et al. (2006) speculated that the reduced transport in the Gulf Stream during the LIA could indicate a reduced AMOC at that time. Based on the SST anomaly of

Mann & Jones (2002; 2003), the LIA correspond to three cooling periods occurring from ~1450-1530 AD, ~1575-1700 AD, and ~1820-1850 AD (Fig. 6.4).

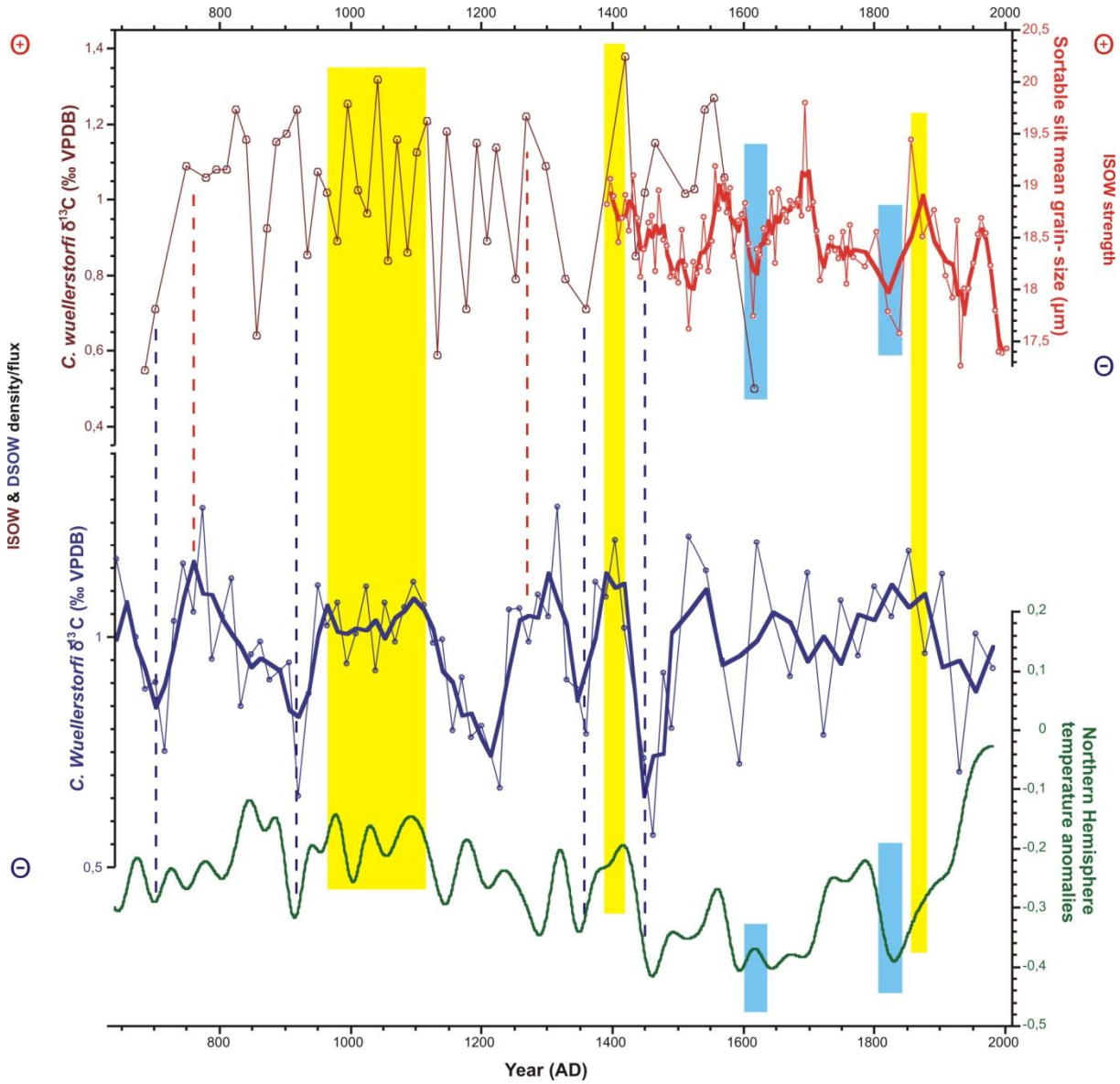

Fig. 6.4: Comparison between ISOW variability (top), DWBC variability (middle), and Northern Hemisphere temperature anomalies over the last ~1350 years. Shown at the top are the proxies for ISOW paleocurrent (red) and paleocirculation (brown) as shown in figure 6.3. In the middle are the paleocirculation variability in DWBC from the Eirik Drift (Johansen 2008). Blue data points, and corresponding lines, shows the averages of the replicates, while the thick blue line is a 3 point running average. The bottom plot shows a 40 year smooth (lowpass filter) of the Northern Hemisphere temperature anomaly reconstructions from Mann & Jones (2002). The temperature dataset represent temperature deviations from the 1961-1990 instrumental reference period. The blue stippled line indicates reduced Nordic Seas overflow in both branches, corresponding to a cooling period in the SST reconstructions, while the red stippled lines indicate periods with strong overflows in both branches, which do not correspond to a warming in the SST reconstructions. Yellow boxes indicate period with strong overflow in both branches corresponding to a warming in the SST reconstructions, while blue boxes indicate reduced ISOW vigor corresponding to cooling periods in the SST reconstructions.

The first of these cooling periods coincides with a reduced overflow in both branches, thus indicating that the reduced AMOC during that period could be responsible for some of the

cooling. While the western overflow indicates a rapid recovery back to strong overflow, the ISOW paleocurrent proxy indicates reduced flow during this entire cooling period. Furthermore, the ISOW paleocurrent proxy indicate a reduced flow during the start of the second cooling period, and during the entire third cooling period (blue boxes in Fig. 6.4). The fact that the western overflow does not show particularly low $\delta^{13}C$ values during the second and third cooling periods, indicate that the AMOC cannot explain all of the observed cooling. Previous to the three LIA cooling periods, there is a short period (1330-1360 AD) indicating relatively cool conditions, which also coincides with reduced overflow in both branches. These findings suggest that during some parts of the LIA the AMOC was reduced. The observation that both overflowing branches show relatively large variations in the production of Nordic Seas overflow waters in this period, are also in agreement with the finding that the LIA was not a continuously cold period (Bradley & Jones, 1992; 1993; Matthews & Briffa, 2005; Nesje et al., 2005). Even though it is not possible to draw firm conclusions from the comparison of the two overflowing branches, these findings suggests that a reduced overflow could explain some of the cooling associated with the LIA. To further investigate this hypothesis, flow speed reconstructions from the gravity core used in this study, and the western branch of the Nordic Seas overflows, should be undertaken.

The warming associated with the MWP-and cooling associated with the LIA, is known to be affected by external forcing mechanisms like solar and volcanic forcing (Mann 2002a; Mann 2002b; Nesje & Dahl, 2003; Jansen et al., 2007; Nesje et al., 2007, and references therein). Some of the minima in the ISOW flow speed proxy and $\delta^{13}C$ proxy occur during periods of low solar insolation coupled with high volcanic activity (Fig. L.1, Appendix L). However, during several other occasions the ISOW vigor and chemical properties show no response, or vary in exactly the opposite sense to external forcings. This suggests the presence of significant internal variability in ocean circulation, and that the circulation is not responding in a simple way to solar or volcanic forcing.

In the recent years, volume flux estimates of the overflow through the Faroe-Bank Channel has shown a decrease since 1950 AD (Hansen et al., 2001), which they ascribe to a reduction of total AMOC, since comparable estimates from the Denmark Strait did not show an increase in overflow to compensate for the reduction of the eastern overflow (Dickson et al., 1999). However, the findings of Hansen et al. (2001) has recently been challenged by Olsen et al. (2008), where it was found that the overflows over the Greenland-Scotland had not changed significantly over the past ~50 years. We find a decrease in ISOW vigor since ~ 1960 AD;

however, this decrease is only one of several oscillations in ISOW vigor over the past ~600 years, and is not significant in the broader context. More importantly, we see a trend of decreasing ISOW flow vigor over the last ~600 years, which could be a part of a longer term trend in the AMOC evolution. For instance, Bianchi & McCave (1999) found a 1500 years quasi-periodic variability in ISOW vigor. To assess this possibility, reconstructions further back in time are needed. This has implications for the future evolvement of the AMOC, since it is projected that the AMOC will decrease in the 21th century due to the continued release of greenhouse gases (Clark et al., 2008).

6.3 Comparison between the oxygen isotope results and sortable silt mean grain-size results from the multicore

The planktonic $\delta^{18}O$ records from our core location provide insight into how local surface water hydrography and climate varied in relationship to basin wide climate (AMO) and deep overturning changes (ISOW). The three different planktonic foraminifer records from the multicore all show $\delta^{18}O$ variations on multidecadal to centennial timescales related to changes in temperature and/or salinity. Figure 6.5 shows the three planktonic foraminifer records, and the sortable silt mean grain-size variations plotted against age.

Changes in the $\delta^{18}O$ from planktonic foraminifers are a proxy for changes in temperature and salinity. Temperature (Locarnini et al., 2006) and salinity (Antonov et al., 2006) data from the World Ocean Atlas 2005 (Appendix H), indicate that the temperature and salinity difference between summer and winter at the surface in the study area is ~3.4°C and ~0.02 psu, respectively. Based upon the temperature and salinity relationship outlined in Appendix H, this corresponds to a $\delta^{18}O_c$ difference of 0.82 ‰ and 0.016 ‰ related to temperature and salinity, respectively. Thus, our planktonic foraminifers are much more sensitive to temperature changes than salinity. Considering the small salinity difference between the warmest and coldest seasons at the surface in the study area, the measured $\delta^{18}O_c$ variability in the different planktonic foraminifer species are interpret to be caused primarily by temperature changes. Based upon the calculated $\delta^{18}O_{eq}$ of the top 250 m in the study area (Appendix H), *G. bulloides* and *N. pachyderma* (d) are used to reconstruct summer near surface (0-50 m and 50-75 m, respectively) temperature changes, while *G. inflata* are used to reconstruct winter/ subsurface (75-200 m) temperature changes.

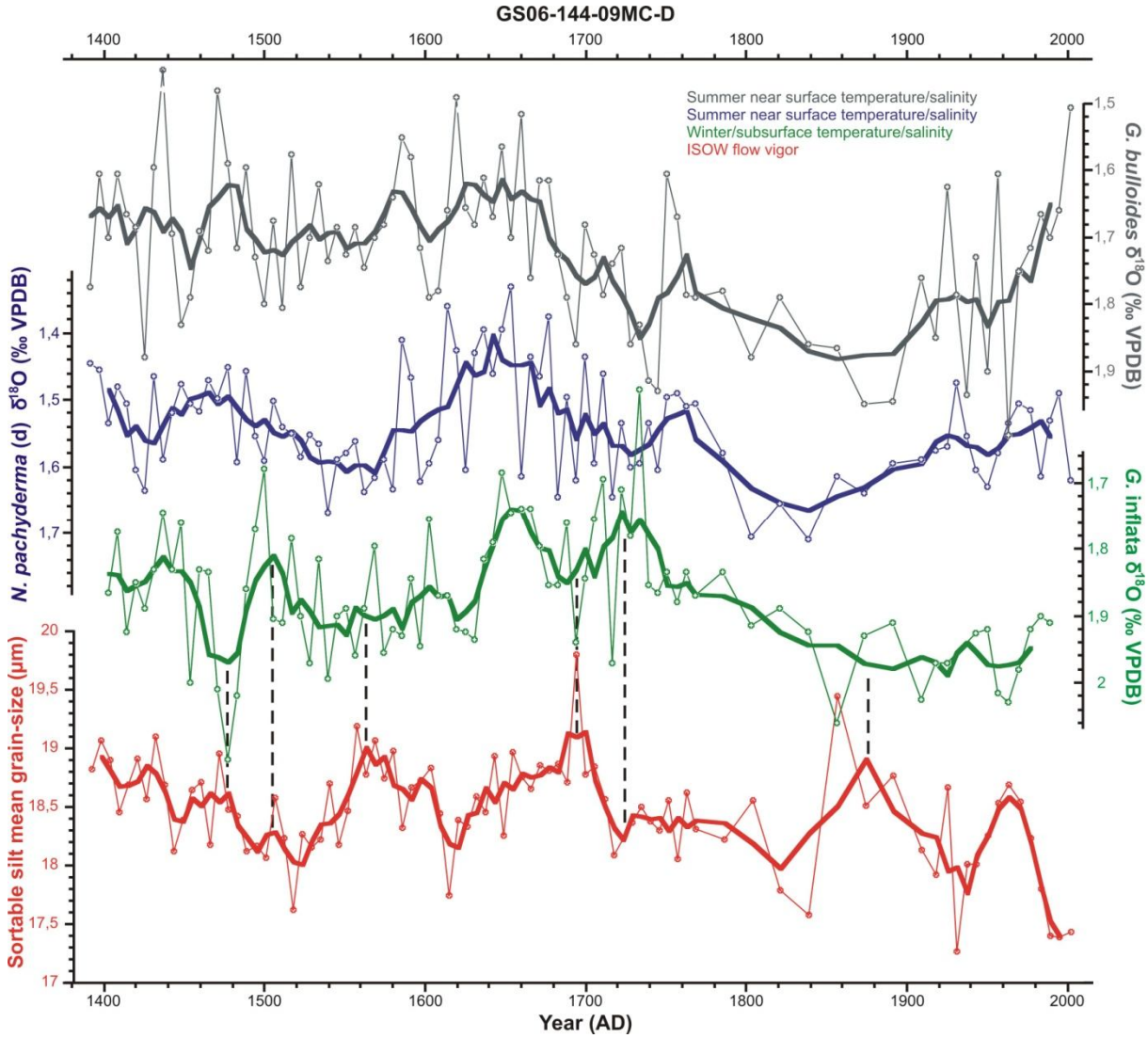

Fig. 6.5: Comparison between the three planktonic foraminifer records and the sortable silt mean grain-size paleocurrent record. The planktonic records shows the average of two replicates (thin lines) in conjugation with the 5 point smoothed of the two replicates, while the sortable silt mean grain-size is plotted in the same manner, but with a 3 point smoothing of the two replicates. The black stippled line illustrates the antiphasing between *G. inflata* and the sortable silt record.

Our two records for near surface temperature variability are roughly in phase throughout the record, with the exception of a relatively small cooling period centered around ~1450 AD in the *G. bulloides* record not apparent in the *N. pachyderma* (d) record (Fig. 6.5). The close coupling between the two near surface records indicates that temperature has varied on multidecadal to centennial timescales during the last ~600 years. The warmest (lowest $\delta^{18}O$) period in both near surface water temperature records is in the 17th century, while the coolest (highest $\delta^{18}O$) period in both record are between ~1640-1840 AD. This cooling period is within the time range of the Little Ice Age (LIA) (Grove 1988; Bradley & Jones, 1992; 1993; Matthews & Briffa, 2005; Nesje et al., 2005). However, it is evident from these two near

surface temperature records that the LIA at this location was not a continuous cold period, since the warmest period in the records occurs in the 17th century. From ~1840 AD the *N. pachyderma* (d) record shows a slow warming toward modern times, while the warming in the *G. bulloides* record does not start until ~1890 AD. Neither of the two records shows the abrupt warming seen in other record the last 150 years (e.g. Mann & Jones, 2003). This could be caused by bioturbative smoothing, but since there is such clear variability in the paleocurrent record that matches well to the AMO, it is more likely, as postulated in chapter 6.1, that the top of the core is younger than assumed, which would explain why none of the near surface records register the abrupt warming over the last decades. The lack of coherence with our mean sortable silt record indicates that the variability in the local near surface hydrography is not in phase with deepwater circulation changes, or basin wide temperatures (AMO). This suggests that the mechanisms that govern the temperature in the Iceland Basin are complex.

G. inflata, our record for winter (thermocline) subsurface waters, shows similar scale variability, but is out of phase with the near surface temperature records. The *G. inflata* record suggests that particularly cool conditions occurred at the end of the 15th century, while a warming event is indicated by the *G. bulloides* record. Conditions were generally cool in the 16th and the beginning of the 17th century, warm until the middle of the 18th century, and cool for the remainder of the record. Interestingly, the coldest period in the record occurred in the last ~150 years. This indicates that near surface summer temperature variability in the Iceland Basin over the last ~600 years was not closely coupled to winter temperature. The only exception is a period during the 17th century, which shows pronounced warming in both near surface summer proxies, and in the winter/subsurface proxy. This indicates that this particularly warm event involved higher year-around temperatures, which extended even to subsurface waters down to 200 m depth.

Although noisy, the winter/subsurface temperature proxy appears antiphased with ISOW flow during some of the largest anomalies in both records. This relationship, cool subsurface/winter temperatures when ISOW is strong, is in agreement with preliminary modeling result which shows that the winter temperature south of Iceland is intermittently anticorrelated with the AMO (Pers. comm. O. H. Otterå) (recall that our record of ISOW vigor showed a close coupling with AMO). One possibility that could explain this relationship is related to a shift in the position of the North Atlantic Current (NAC), due to an expansion (retraction) of the North Atlantic subpolar gyre.

The North Atlantic subpolar gyre (SPG) consists of cold and relatively fresh waters (Hátún et al., 2009), and is constrained to the east by Modified Atlantic Intermediate Water (MNAIW) (Hansen & Østerhus, 2000), which is water mass composed of water from the NAC and the warmer and more saline Eastern North Atlantic Water (ENAW) [7] (Holliday 2003; Hátún et al., 2009) (Fig. 6.6). According to Hátún et al. (2009), the surface hydrography in the Iceland Basin is affected by the SPG in two ways. When the SPG weakens, the cold and fresh sub-arctic waters retracts from the Iceland Basin, and is replaced by the warmer and more saline MNAW (Fig. 6.6 b). At the same time, the retracing gyre allows the warmer ENAW to expand, which warms and increases the salinity of the MNAW. Conversely, a strengthening of the SPG baths the Iceland Basin with cold, fresh sub-arctic waters (Fig. 6.6 a). As illustrated in figure 6. 6, our core is located in a part of the Iceland Basin that is sensitive to fluctuations in the SPG. Clearly, the SPG plays an important part in modulating the surface hydrography in the Iceland Basin, and there is evidence indicating that it has done so throughout the Holocene period (Thornalley et al., 2009).

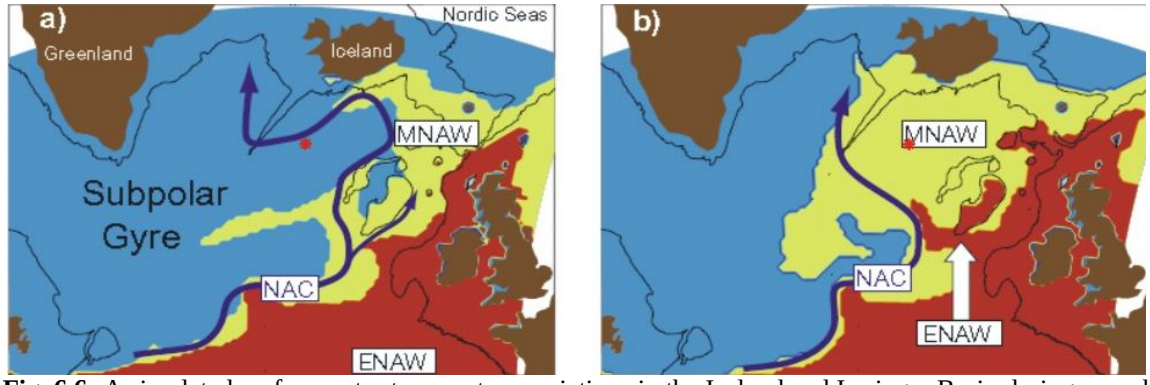

Fig. 6.6: A simulated surface water temperature variations in the Iceland and Irminger Basin during a weak SPG **a)** (1993) and a strong SPG **b)** (1998). Red colors indicate temperatures above 9°C and blue below 7°C, while yellow colors indicate intermediate temperatures, and is illustrating the distribution MNAW. The red star indicates approximately the core location. Modified after Hátún et al. (2005; 2009).

Figure 6.7 shows a hydrographic section of salinity and temperature that crosses the core site. Today the site sits in the transition zone between the SPG and MNAW (middle foraminifer calcification depth distribution), resulting in a relatively strong vertical temperature gradient in the near surface waters. The temperature section indicates that both *G. bulloides* and *N. pachyderma* (d) is today situated in relatively uniform water masses associated with MNAW, while *G. inflata* is bathed by colder water from the SPG. Yet, the salinity section indicates that all three planktonic foraminifers are currently bathed by low salinity SPG water. Even so, the range of salinities in the region of the core site is relatively small compared to the

[7] This water mass contains waters from the Continental Slope Current and Mediterranean waters (see subchapter 2.2.1).

temperature differences, and is unlikely to drive significant $\delta^{18}O$ variability. From figure 6.5 it was shown that the winter/subsurface temperature variability was out of phase with summer near surface temperature variability. This out of phase relationship can be explained with variations in the position of the MNAW and the SPG (illustrated in figure 6.7), while uniform cold periods can be explained by the most northwestern plot of the calcification depths, where all the foraminifers is bathed by the relatively cold SPG (e.g. 16th century in *N. pachyderma* (d) and *G. inflata*), and uniform warm periods by the southeastern plot of the calcification depth associated with a weak SPG (e.g. in the 17th century for all the planktonic foraminifer species).

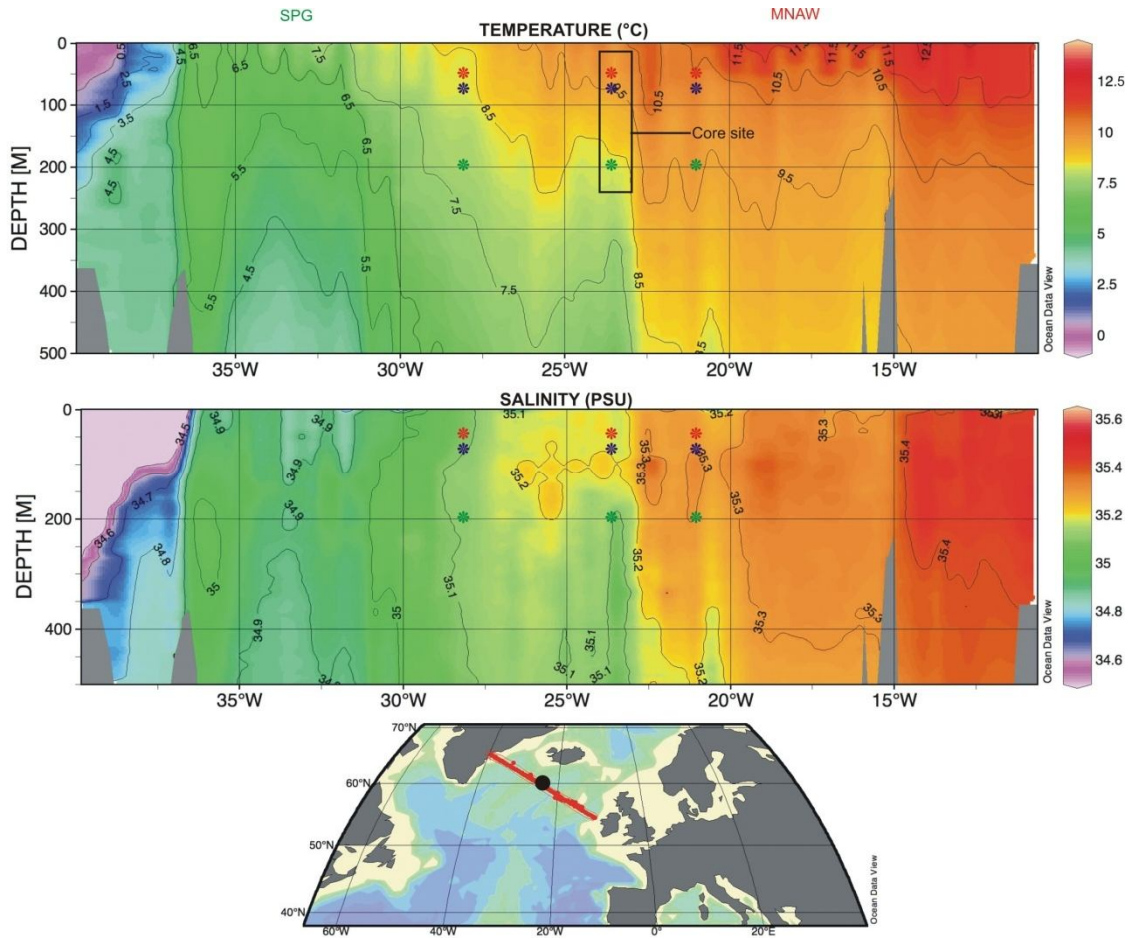

Fig. 6.7: Hydrographic section crossing the core site showing temperature (top) and salinity (middle). At the bottom of the figure there is a map showing where the cross-section is taken (core location marked with black dot), which is the WOCE hydrographic section A24N. Plotted as stars in the temperature and salinity sections are the maximum calcification depths of *G. bulloides* (red), *N. pachyderma* (d) (blue), and *G. inflata* (green). The middle of the three calcification depth plots illustrates the hydrography above the core location, while the northwestern and southeastern calcification depth plots illustrates the hydrography associated with a strong and weak SPG, respectively. The data is gathered from Schlitzer (2000) and plotted with Ocean Data View (Schlitzer 2009).

The relationship between the strength of the SPG and the hydrographic properties of the North Atlantic Ocean has been associated with the atmospheric pattern called the North Atlantic Oscillation (NAO). During a shift from a positive NAO index (strong westerlies) in 1995, to a negative NAO index (weak westerlies) in 1996-1997, the SPG, which at that time filled the Iceland Basin, weakened and contracted, and within 2 years the Iceland Basin was filled with the relatively warm and saline MNAW (Bersch 2002; Bersch et al., 2007; Hátún et al., 2009). Thus, during a positive NAO phase where Norway and most of Northern Europe experience mild and humid winters (Nesje & Dahl, 2003; Nesje et al., 2007), the climate in the Iceland Basin becomes colder. A recent modeling study indicates that under a persistent positive NAO forcing the SPG intensifies during the first decade, but thereafter slows down (Lohmann et al., 2009). This occurs because the cooling of the surface water in the SPG increases the formation of deepwater (LSW) in the subpolar basins. The increased production of LSW intensifies the AMOC, which results in increased transport of warm water from the North Atlantic subtropical gyre into the SPG. On the other hand, Lohmann et al. (2009) found that under a persistent negative NAO forcing the SPG weakens and warms, without an oceanic feedback to counteract it. In summary, while models predict that the NAO, SPG, and AMOC could be dynamically linked, the sign and strength of this connection is both complex and temporally variable.

Figure 6.8 shows 30-year smooth of the NAO winter (December-March) index (inverted) together with *G. bulloides* and *N. pachyderma* (d) $\delta^{18}O$ records. There is a relative good correlation between the inverted NAO index and *G. bulloides* from ~1560 to ~1860 AD, and between the inverted NAO index and *N. pachyderma* (d) from ~1620 AD to ~1840 AD. Similar to the AMO-ISOW comparison, our two near surface temperature records are out of phase with NAO in the youngest part of the record (chapter 6.1). Although the correlation between our near surface water temperature proxies and NAO is not as good as the correlation between our paleocurrent proxy and AMO, the apparent connection at some intervals suggests that the NAO may influence the hydrography in the Iceland Basin-perhaps-through interactions with the SPG. The fact that the NAO alone cannot explain the observed temperature variations at our core site, further demonstrate the complexity of the hydrography in the Iceland Basin.

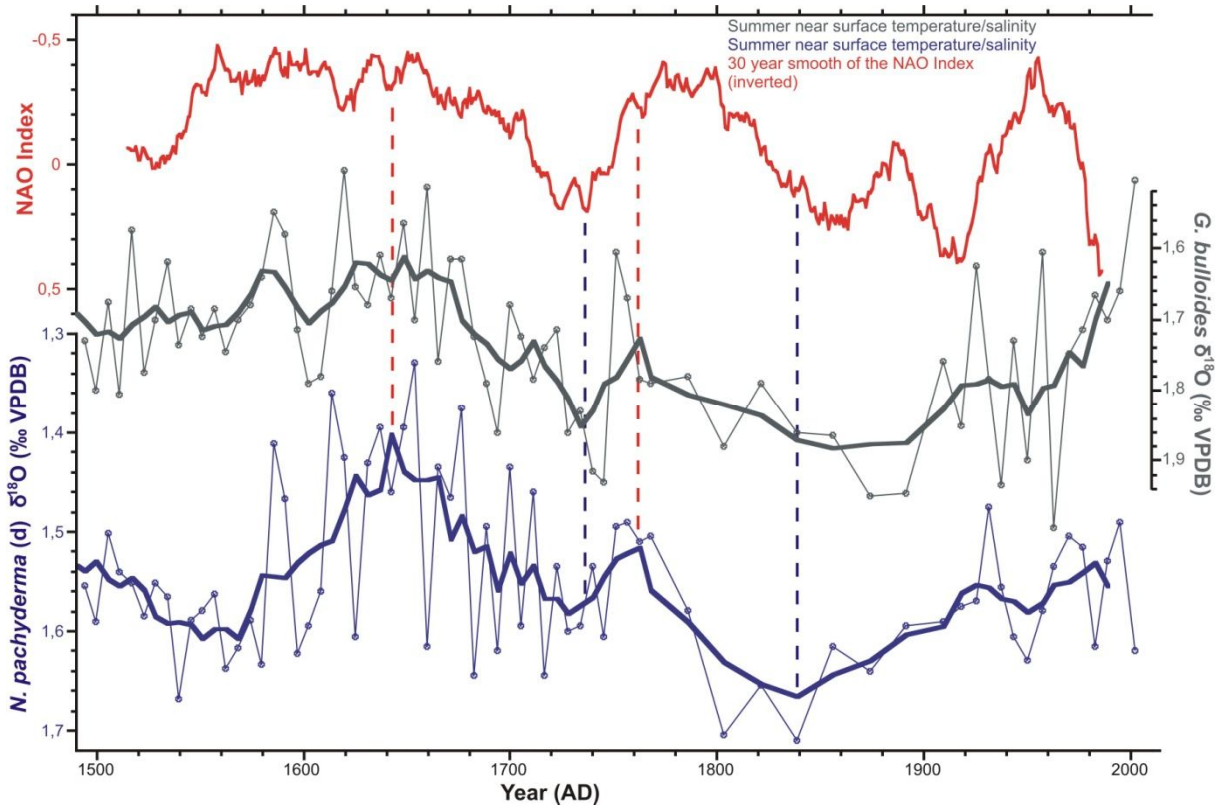

Fig. 6.8: The NAO winter index (inverted), and our proxies for near surface temperature variability plotted against depth. Both planktonic records show the average of two replicates (thin lines and corresponding data points) in conjugation with a 5 point smooth of the replicates. The blue (cool periods) and red (warm periods) stippled lines indicates in phase relationship. The NAO data set was gathered from Luterbacher et al. (1999; 2002).

The lack of coherence between our ISOW flow speed record and local near surface hydrography in the Iceland Basin, as well as the close coupling between basin wide SST (AMO) and ISOW flow vigor, strongly suggests that ISOW vigor cannot be explained or driven in a simple way by changes in the SPG-otherwise-the mean sortable silt record would be closely in phase with the planktonic $\delta^{18}O$ records.

6.4 Summary and perspective

In this study we set out to investigate the hypothesis that the ocean overturning circulation was involved in Atlantic low frequency (multidecadal-centennial) modes of climate variability, such as the AMO. This study provides the first evidence that AMOC variability is tightly coupled to low frequency variations in basin-wide climate. In particular, that the eastern branch of the Nordic Seas overflows (ISOW), an important branch of the lower limb of the AMOC, has varied closely in phase with AMO over the past ~350 years. In addition, the close correlation between ISOW vigor and deepwater chemical properties ($\delta^{13}C$) suggests that similar variability in ISOW characterized the last ~1300 years. The close coupling

between ISOW and AMO (warm Atlantic when ISOW is strong), and the lack of any significant lag between ISOW and climate, is consistent with the hypothesis that the AMO is driven by the AMOC. One obvious next step for confirming this hypothesis is to investigate if changes in the western branch of the Nordic Seas overflows (i.e. total AMOC) are in phase with ISOW. The benthonic $\delta^{13}C$ record monitoring the integrated overflows at the Eirik drift (DWBC) provides intriguing evidence that some of the more prominent changes in the ISOW vigor have counterparts in the western overflows (DSOW). However, firm conclusions cannot be drawn until we have comparable sortable silt mean grain-size records of DSOW vigor from the integrated overflows.

Our results have potential relevance for understanding current and future climate behavior. The "natural variability" in basin-wide climate (AMO) appears tightly coupled to-and positively in phase with-ISOW vigor over the past ~350 years. By contrast, there is no clear increase in ISOW vigor associated with hemispheric and global warming trends in the recent decades. This suggests that the recent climate warming has a fundamentally different relationship to ocean circulation than that observed over the past ~350 years. This is in agreement with the hypothesis that the recent climate warming is caused predominantly by anthropogenic forcing rather than "natural" climate-ocean interactions (Solomon et al., 2007). However, our results also highlight the importance of understanding natural variability in ocean circulation for climate predictability on multidecadal timescales, since every multidecadal oscillation in ISOW vigor over the past few centuries involved (and potentially drove) a synchronous change in Atlantic-wide climate.

7 REFERENCES

Andersen, B. G., Mangerud, J., Sørensen, R., Reite, A., Sveian, H., Thoresen, M., and Bergström, B. (1995). "Younger Dryas ice-marginal deposits in Norway." Quaternary International **28**: 147-169.

Andersen, T. J. (2007). Dating of core GS06-144-09MCD, Gamma Dating Center Copenhagen, Institute of Geography, University of Copenhagen, Denmark.

Andersson, C., Risebrobakken, B., Jansen, E., and Dahl, S. O. (2003). "Late Holocene surface ocean conditions of the Norwegian Sea (Vøring Plateau)." Paleoceanography **18**(2): 1044, doi: 10.1029/2001PA000654.

Antonov, J. I., Locarnini, R. A., Boyer, T. P., Mishonov, A. V., and Garcia, H. E. (2006). Volume 2: Salinity. World Ocean Atlas 2005. S. Levitus, NOAA Atlas NESDIS 62, U. S. Goverment Printing Office, Washington, D. C.**:** 182 pp.

Appleby, P. G. (2001). Chronostratigraphic Techniques in Recent Sediments. Tracking Environmental Change Using Lake Sediments, Part III. W. M. Last, J. P. Smol, and H. J. B. Birks, Springer Netherlands. **1 (4):** 171-203, 532pp.

Appleby, P. G., and Oldfield, F. (1983). "The assessment of ^{210}Pb data from sites with varying sediment accumulation rates." Hydrobiologia **103**(1): 29-35.

Armstrong, H. A., Brasier, M. D. (2005). Microfossils, second edition. Ch. 15: Foraminifera, Blackwell Publishing**:** 142-187.

Bauch, D., Carstens, J., and Wefer, G. (1997). "Oxygen isotope composition of living *Neogloboquadrina pachyderma* (sin.) in the Arctic Ocean." Earth and Planetary Science Letters **146**(1-2): 47-58.

Bauch, D., Darling, K., Simstich, J., Bauch, H. A., Erlenkeuser, H., and Kroon, D. (2003). "Palaeoceanographic implications of genetic variation in living North Atlantic *Neogloboquadrina pachyderma*." Nature **424**(6946): 299-302.

Bemis, B. E., Spero, H. J., Bijma, J., and Lea, D. W. (1998). "Reevaluation of the Oxygen Isotopic Composition of Planktonic Foraminifera: Experimental Results and Revised Paleotemperature Equations." Paleoceanography **13**(2): 150-160.

Bersch, M. (2002). "North Atlantic Oscillation-induced changes of the upper layer circulation in the northern North Atlantic Ocean." Journal of Geophysical Research **107**(C10): 3156, doi: 10.1029/2001JC000901.

Bersch, M., Yashayaev, I., and Koltermann, K. (2007). "Recent changes of the thermohaline circulation in the subpolar North Atlantic." Ocean Dynamics **57**(3): 223-235.

Bianchi, G. G., and McCave, I. N. (1999). "Holocene periodicity in North Atlantic climate and deep-ocean flow south of Iceland." Nature **397**(6719): 515-517.

Bianchi, G. G., and McCave, I. N. (2000). "Hydrography and sedimentation under the deep western boundary current on Björn and Gardar Drifts, Iceland Basin." Marine Geology **165**(1-4): 137-169.

Bianchi, G. G., Hall I. R., McCave I. N., and Joseph L. (1999). "Measurement of the sortable silt current speed proxy using the Sedigraph 5100 and Coulter Multisizer IIe: precision and accuracy." Sedimentology **46**(6): 1001-1014.

Blaeser, C. R. and M. T. Ledbetter (1982). "Deep-sea bottom-currents differentiated from texture of underlying sediment." JOURNAL OF SEDIMENTARY RESEARCH **52**(3): 755-768.

Boessenkool, K. P., Hall, I. R., Elderfield, H., and Yashayaev I. (2007). "Reykjanes Ridge Sub-decadal Mean Grain Size Data." IGBP PAGES/World Data Center for

Paleoclimatology, #2007-095, NOAA/NGDC Paleoclimatology Program, Boulder CO, USA.

Boessenkool, K. P., Hall, I. R., Elderfield, H., and Yashayaev I. (2007a). "Deep-ocean flow-speed changes linked to the NAO through Labrador Sea convection " PAGES News **16**(1).

Boessenkool, K. P., Hall, I. R., Elderfield, H., and Yashayaev I. (2007b). "North Atlantic climate and deep-ocean flow speed changes during the last 230 years." Geophysical Research Letters **34**: L13614, doi:10.1029/2007GL030285.

Boyle, E. A. (1986). "Paired carbon isotope and cadmium data from benthic foraminifera: Implications for changes in oceanic phosphorus, oceanic circulation, and atmospheric carbon dioxide." Geochimica et Cosmochimica Acta **50**(2): 265-276.

Bradley, R. S. (1999). Paleoclimatology: Reconstructing Climates of the Quaternary, Second Edition. R. Dmowska, and J. R. Holten, INTERNATIONAL GEOPHYSICS SERIES,Elsvier Academic press. **68:** 614 pp.

Bradley, R. S., and Jones, P.D. (1992). When was the "Little Ice Age" ? Proceedings of the International Symposium on the Little Ice Age Climate. T. Mikami, Department of Geography, Tokyo Metropolitan University**:** 1-5.

Bradley, R. S., and Jones, P.D. (1993). "'Little Ice Age'summer temperature variations: their nature and relevance to recent global warming trends." The Holocene **3**(4): 367-376.

Broecker, W. S., and Peng T. H. (1982). Chapter 6: WHAT KEEPS THE SYSTEM IN WHACK? Control Mechanism Operating in the Sea. Tracers in the Sea, A Publication of the Lamont-Doherty Geological Observatory, Columbia University, Palisades, New York.

Broecker, W. S., Kennett, J. P., Flower, B. P., Teller, J. T., Trumbore, S., Bonani, G., and Wolfli, W. (1989). "Routing of meltwater from the Laurentide Ice Sheet during the Younger Dryas cold episode." Nature **341**(6240): 318-321.

Clark, I. D., and Fritz P. (1997). CHAPTER 1: THE ENVIRONMENTAL ISOTOPES. Environmental Isotopes in Hydrogeology, Lewis Publishers, Boca Raton, New York.

Clark, P. U., Weaver, A. J., Brook, E., Cook, E. R., Delworth, T. L., and Steffen, K. (2008). "Executive Summary." In: Abrupt Climate Change. A report by the U. S. Climate Change Science Program and the Subcommittee on Global Change Research, U. S., Geological Survey, Reston, VA: 7-18.

Clarke, G., Leverington, D., Teller, J., Dyke, A. (2003). "PALEOCLIMATE: Enhanced: Superlakes, Megafloods, and Abrupt Climate Change." Science **301**(5635): 922-923.

Cléroux, C., Cortijo, E., Duplessy, J. C., and Zahn, R. (2007). "Deep-dwelling foraminifera as thermocline temperature recorders." Geochemistry Geophysics Geosystems. **8**: Q04N11, doi:10.1029/2006GC001474.

Cooke, S., and Rohling E. J. (2001). "Stable Isotopes in Foraminiferal Carbonate." Southhampton Oceanography Centre Internal Document **72**: 56pp.

Coplen, T. B., Kendall, C., and Hopple, J. (1983). "Comparison of stable isotope reference samples." Nature **302**(5905): 236-238.

Craig, H. (1965). Measurement of oxygen isotope paleotemperatures. Stable Isotopes in Oceanographic Studies and Paleotemperatures. E. Tongiorgi, Cons. Naz. Delle Ric, Spoleto, Italy**:** 161-182, 337 pp.

Craig, H., and Gordon, L. I. (1965). Isotopic Oceanography: Deuterium and oxygen 18 variations in the ocean and the marine atmosphere. Stable Isotopes un Oceanographic Studies and Paleotemperatures. E. Tongiorgi. Cons. Naz. di Rech, Spoleto, Italy.

Culver, S. J. (1993). Chapter 12: Foraminifera **In:** Foraminifera from Fossil Prokaryotes and Protists. E. b. J. H. Lipps, Blackwell Scientific Publications**:** 203-247.

Curry, R., and Mauritzen, C. (2005). "Dilution of the Northern North Atlantic Ocean in Recent Decades." Science **308**(5729): 1772-1774.

Curry, W. B., Duplessy, J. C., Labeyrie, L. D., and Shackleton, N. J. (1988). "Changes in the Distribution of $\delta^{13}C$ of Deep Water $\sum CO_2$ Between the Last Glaciation and the Holocene." Paleoceanography **3**(3): 317-341.

Dahl, C. A. (2007). GEOL 202, Benthic foraminifers, North Atlantic/Norwegian Sea. Compendium in Geol 202, Marin micropalaeontologi, University of Bergen/Bjerknes Centre for Climate Research, Norway.

Darling, K. F., Kucera, M., Kroon, D., Wade, C. M. (2006). "A resolution for the coiling direction paradox in *Neogloboquadrina pachyderma*." Paleoceanography **21**: PA2011, doi:10.1029/2005PA001189.

Delworth, T. L., Clark, P. U., Holland, M., Johns, W. E., Kuhlbrodt, T., Lynch-Stieglitz, J., Morrill, C., Seager R., Weaver, A. J., and Zhang, R. (2008). "The potential for abrupt change in the Atlantic Meridional Overturning Circulation." In: *Abrupt Climate Change*. A report by the U. S. Climate Change Science Program and the Subcommittee on Global Change Research, U. S., Geological Survey, Reston, VA: 258-259.

Delworth, T. L., Zhang, R., and Mann, M. E. (2007). Decadal to Centennial Variability of the Atlantic From Observations and Models. ***in*** Ocean Circulation: Mechanisms and Impacts, Section 4. Decadal to Centennial Variability. A. Schmittner, J. Chiang, S. Hemmings, Geophysical Monograph Series, AGU. **173:** 131-147, 392pp.

Denton, G. H., and Broecker, W. S. (2008). "Wobbly ocean conveyor circulation during the Holocene?" Quaternary Science Reviews **27**(21-22): 1939-1950.

Dickson, B., Meincke, J., Vassie, I., Jungclaus, J., and Østerhus, Svein (1999). "Possible predictability in overflow from the Denmark Strait." Nature **397**(6716): 243-246.

Dickson, B., Yashayaev, I., Meincke, J., Turrell, B., Dye, S., and Holfort, J. (2002). "Rapid freshening of the deep North Atlantic Ocean over the past four decades." Nature **416**(6883): 832-837.

Dickson, R. R., and Brown, J. (1994). "The production of North Atlantic Deep Water: Sources, rates, and pathways." Journal of Geophysical Research **99**(C6): 12319-12341.

Dickson, R. R., Osborn, T. J., Hurrell, J. W., Meincke, J., Blindheim, J., Adlandsvik, B., Vinje, T., Alekseev, G., and Maslowski, W. (2000). "The Arctic Ocean Response to the North Atlantic Oscillation." Journal of Climate **13**(15): 2671-2696.

Duplessy, J. C., Lalou, C., and Vinot, A. C. (1970). "Differential Isotopic Fractionation in Benthic Foraminifera and Paleotemperatures Reassessed." Science **168**(3928): 250-251.

Duplessy, J. C., Shackleton, N. J., Fairbanks, R. G., Labeyrie, L., Oppo, D., and Kallel, N. (1988). "Deepwater Source Variations During the Last Climatic Cycle and Their Impact on the Global Deepwater Circulation." Paleoceanography **3**(3): 343-360.

Ellison, C. R. W., Chapman, M. R., and Hall, I. R. (2006). "Surface and Deep Ocean Interactions During the Cold Climate Event 8200 Years Ago." Science **312**(5782): 1929-1932.

Emiliani, C. (1955). "Pleistocene temperatures." The journal of geology **63**(6): 538-576.

Enfield, D. B., Mestas-Nuñez, A. M., and Trimble, P. J. (2001). "The Atlantic Multidecadal Oscillation and its relation to rainfall and river flows in the continental U.S." Geophysical Research Letters **28**(10): 2077-2080.

Epstein, S., Buchsbaum R., Lowenstam H., and Urey H. C. (1951). "Carbonate-water isotopic temperature scale." Geological Society of America bulletin **62**(4): 417-426.

Epstein, S., Buchsbaum R., Lowenstam H., and Urey H. C. (1953). "Revised carbonate-water isotopic temperature scale." Bulletin of the Geological Society of America **64**: 1315-1326.

Fairbanks, R. (1989). "A 17,000-year glacio-eustatic sea level record: influence of glacial melting rates on the Younger Dryas event and deep-ocean circulation " Nature **342**(6250): 637-642.

Faugères, J. C., Mézerais, M. L., and Stow, D. A. V. (1993). "Contourite drift types and their distribution in the North and South Atlantic Ocean basins." Sedimentary Geology **82**(1-4): 189-203.

Faugères, J. C., Stow, D. A. V., Imbert, P., and Viana, A. (1999). "Seismic features diagnostic of contourite drifts." Marine Geology **162**(1): 1-38.

Field, D. B. (2004). "Variability in vertical distributions of planktonic foraminifera in the California Current: Relationships to vertical ocean structure." Paleoceanography **19**(2).

Flett, R. F. (2003). "Understanding the Pb-210 Method." Flett Research Ltd., Winnipeg, Manitoba, Canada Retrieved 03.04, 2009, from http://www.flettresearch.ca/Webdoc4.htm.

Fratantoni, D. M. (2001). "North Atlantic surface circulation during the 1990's observed with satellite-tracked drifters." Journal of Geophysical Research **106**(C10): 22067-22093.

Ganachaud, A. and C. Wunsch (2000). "Improved estimates of global ocean circulation, heat transport and mixing from hydrographic data." Nature **408**(6811): 453-457.

Ganssen, G. (1983). "Dokumentation von küstennahem Auftrieb anhand stabiler Isotope in rezenten Foraminiferen vor Nordwest-Afrika." "Meteor" Forsch Ergebn **C37**: 1-46.

Ganssen, G. M., and Kroon, D. (2000). "The isotopic signature of planktonic foraminifera from NE Atlantic surface sediments: implications for the reconstruction of past oceanic conditions." Journal of the Geological Society **157**(3): 693-699.

Goldenberg, S. B., Landsea, C. W., Mestas-Nuñez, A. M., and Gray, W. M. (2001). "The Recent Increase in Atlantic Hurricane Activity: Causes and Implications." Science **293**(5529): 474-479.

González-Rouco, F., von Storch, H., and Zorita, E. (2003). "Deep soil temperature as proxy for surface air-temperature in a coupled model simulation of the last thousand years." Geophysical Research Letters **30**(21): 2116, doi: 10.1029/2003GL018264.

Graham, D. W., Corliss B. H., Bender, M. L., and Keigwin L. D. (1981). "Carbon and oxygen isotopic disequilibria of recent deep-sea benthic foraminifera." Marine Micropaleontology **6**: 483-497.

Gray, S. T., Graumlich, L. J., Betancourt, J. L., and Pederson, G. T. (2004). "Atlantic Multidecadal Oscillation (AMO) Index Resolution." IGBP PAGES/World Data Center for Paleoclimatology, #2004-062, NOAA/NGDC Paleoclimatology Program, Boulder CO, USA.

Gray, S. T., Graumlich, L. J., Betancourt, J. L., and Pederson, G. T. (2004). "A tree-ring based reconstruction of the Atlantic Multidecadal Oscillation since 1567 A.D." Geophysical Research Letters **31**: L12205, doi:10.1029/2004GLO19932.

Grossman, E. L. (1987). "Stable isotopes in modern benthic foraminifera; a study of vital effect." Journal of foraminiferal research **17**(1): 48-61.

Grove, J. M. (1988). The Little Ice Age, Methuen, London,: 498 pp.

Hall, I. R., Bianchi, G. G., and Evans, J. R. (2004). "Centennial to millennial scale Holocene climate-deep water linkage in the North Atlantic." Quaternary Science Reviews **23**(14-15): 1529-1536.

Hansen, B., and Østerhus, S. (2000). "North Atlantic-Nordic Seas exchanges." Progress In Oceanography **45**(2): 109-208.

Hansen, B., Turrell, W. R., and Østerhus, S. (2001). "Decreasing overflow from the Nordic seas into the Atlantic Ocean through the Faroe Bank channel since 1950." Nature **411**(6840): 927-930.

Hátún, H., Payne, M. R., Beaugrand, G., Reid, P. C., Sandø, A. B., Drange, H., Hansen, B., Jacobsen, J. A., and Bloch, D. (2009). "Large bio-geographical shifts in the north-eastern Atlantic Ocean: From the subpolar gyre, via plankton, to blue whiting and pilot whales." Progress In Oceanography **80**(3-4): 149-162.

Hátún, H., Sando, A. B., Drange, H., Hansen, B., and Valdimarsson, H. (2005). "Influence of the Atlantic Subpolar Gyre on the Thermohaline Circulation." Science **309**(5742): 1841-1844.

Holbourn, A. E., Henderson, A. S. (2002). "Re-illustration and Revised Taxonomy for Selected Deep-sea Benthic Foraminifers." Palaeontological Electronica **4**(2): 34pp., 628KB, http://paleo-electronica.org/paleo/2001_2/foram/issue2_01.htm.

Holliday, N. P. (2003). "Air-sea interaction and circulation changes in the northeast Atlantic." Journal of Geophysical Research **108**(C8): 3259, doi:10.1029/2002JC001344.

Hughen, K., Baille, M., Bard, E., Beck, J., Bertrand, C., Blackwell, P., Buck, C., Burr, G., Cutler, K., Damon, P., Edwards, R., Fairbanks, R., Friedrich, M., Guilderson, T., Kromer, B., McCormac, F., Manning, S., Bronk-Ramsey, C., Reimer, P., Reimer, R., Remmele, S., Southon, J., Stuiver, M., Talamo, S., Taylor, F., der Plicht, J. v., Weyhenmeyer, C. (2004). "Marine04 Marine radiocarbon age calibration, 26-0 ka BP." Radiocarbon **46**(3): 37p.

Hunter, S., Wilkinson, D., Louarn, E., McCave, N. I., Rohling, E., Stow, D. A. V., and Bacon, S. (2007a). "Deep western boundary current dynamics and associated sedimentation on the Eirik Drift, Southern Greenland Margin." Deep Sea Research Part I: Oceanographic Research Papers **54**(12): 2036-2066.

Hunter, S. E., Wilkinson, D., Stanford, J., Stow, D. A. V., Bacon, S., Akhmetzhanov, A. M., and Kenyon, N. H. (2007b). "The Eirik Drift: a long-term barometer of North Atlantic deepwater flux south of Cape Farewell, Greenland." Geological Society, London, Special Publications **276**(1): 245-263.

Hurrell, J. W. (1995). "Decadal Trends in the North Atlantic Oscillation: Regional Temperatures and Precipitation." Science **269**(5224): 676-679.

Hurrell, J. W. (2008). The North Atlantic Oscillation: Climatic significance and environmental impact. Catastrophe Modeling Forum: Changing Climatic Dynamics and Catastrophe Model Projections, 11-12 June 2008. P. Epstein. New York, USA**:** 8 pp.

Hurrell, J. W., and van Loon, H. (1997). "Decadal Variations in Climate Associated with the North Atlantic Oscillation." Climatic Change **36**(3): 301-326.

Hurrell, J. W., Kushnir, Y., Ottersen, G., and Visbeck, M (2003). An Overview of the North Atlantic Oscillation. The North Atlantic Oscillation: Climate Significance and Environmental Impact. J. W. Hurrell, Y. Kushnir, G. Ottersen, and M. Visbeck, Geophysical Monograph Series Volume 134, American Geophysical Union, Washington, DC**:** 1-36, 279 pp.

Hut, G. (1987). "Stable isotope refrence samples for geochemical and hydrological investigations." Consultants Group Meeting IAEA, Vienna, 16-18.09.1985. Report to the Director General, Int At En Ag, Wien 1-42.

Isachsen, P. E., Mauritzen, C., and Svendsen, H. (2007). "Dense water formation in the Nordic Seas diagnosed from sea surface buoyancy fluxes." Deep Sea Research Part I: Oceanographic Research Papers **54**(1): 22-41.

Jakobsen, P. K., Ribergaard, M. H., Quadfasel, D., Schmith, T., and Hughes, C. W. (2003). "Near-surface circulation in the northern North Atlantic as inferred from Lagrangian

drifters: Variability from the mesoscale to interannual." Journal of Geophysical Research **108**(C8): 3251.

Jansen, E., Overpeck, J., Briffa, K. R., Duplessy, J.-C., Joos, F., Masson-Delmotte, V., Olago, D., Otto-Bliesner, B., Peltier, W. R., Rahmstorf, S., Ramesh, R., Raynaud, D., Rind, D., Solomnia, O., Villalba, R., and Zhang, D. (2007). Paleoclimate. Climate Change 2007: The Physical Science Basis. Contribution of Working Group 1 to the Fourth Assessment Report of the Intergovermental Panel on Climate Change. S. Solomon, D. Quin, M. Manning, Z. Chen, M. Marquis, K. B. Averyt, M. Tignor, and H. L. Miller, Cambridge University Press, Cambridge, United Kingdom and New York, NY, USA.

Jansen, E., Raymo, M. E., Blum, P., et al. (1996). Shipboard Scientific Party, Leg 162, Chapter 5, Site 983. Proc. ODP, Init. Repts., 162, College Station, TX (Ocean Drilling Program). E. Jansen, Raymo, M. E., Blum, P., and Herbert, T.**:** 139-167.

Johansen, I. V. (2008). Atlantic Meridional Overturning Circulation since 600 AD and its link to surface climate variability. Department of Earth Science, University of Bergen. **Master thesis in Geology**.

Johnson, G. L., Schneider, E. D. (1969). "Depositional Ridges in the North Atlantic." Earth and Planetary Science Letters **6**: 416-422.

Keigwin, L., Bice, M., and Copley, N. (2005). "Seasonality and stable isotopes in planktonic foraminifera off Cape Cod, Massachusetts." Paleoceanography **20**: PA4011, doi:1029/2005PA001150.

Kerr, R. A. (2000). "A North Atlantic Climate Pacemaker for the Centuries." Science **288**(5473): 1984-1985.

Kerr, R. A. (2005). "CLIMATE CHANGE: Atlantic Climate Pacemaker for Millennia Past, Decades Hence?" Science **309**(5731): 41-43.

Kidd, R. B., and Hill, P. R. (1987). Sedimentation on Feni and Gardar sediment drifts. Initial Reports of the Deep Sea Drilling Project. **94:** 1217-1244.

Kleiven, H. F., Kissel, C., Laj, C., Ninnemann, U. S., Richter, T. O., and Cortijo, E. (2008). "Reduced North Atlantic Deep Water Coeval with the Glacial Lake Agassiz Freshwater Outburst." Science **319**(5859): 60-64.

Knight, J. R., Allan, R. J., Folland, C. K., Vellinga, M., and Mann, M. E. (2005). "A signature of persistent natural thermohaline circulation cycles in observed climate." Geophysical Research Letters **32**: L20708, doi:10.1029/2005GL02433.

Knight, J. R., Folland, C. K., and Scaife, A. A. (2006). "Climate impacts of the Atlantic Multidecadal Oscillation." Geophysical Research Letters **33**: L17706, doi: 10.1029/2006GL26242.

Kohfeld, K. E., Fairbanks, R. G., Smith, S. L., and Walsh, I. D. (1996). "*Neogloboquadrina Pachyderma* (sinistral coiling) as Paleoceanographic Tracers in Polar Oceans: Evidence from Northeast Water Polynya Plankton Tows, Sediment Traps, and Surface Sediments." Paleoceanography **11**(6): 679-699.

Kroopnick, P. M. (1985). "The distrubution of $\delta^{13}C$ of $\sum CO_2$ in the world oceans." Deep Sea Research, Part A: Oceanographic Research Papers **32**(1): 57-84.

Kuhlbrodt, T., Griesel, A., Montoya, M., Levermann, A., Hofmann, M., and Rahmstorf, S. (2007). "On the driving processes of the Atlantic meridional overturning circulation." Reviews of Geophysics **45**: RG2001, doi:10.1029/2004RG000166.

Ledbetter, M. T. (1986). "A Late Pleistocene time-series of bottom-current speed in the Vema Channel." Palaeogeography, palaeoclimatology, palaeoecology **53**(1): 97-105.

Ledbetter, M. T. and D. A. Johnson (1976). "Increased Transport of Antarctic Bottom Water in the Vema Channel During the Last Ice Age." Science **194**(4267): 837-839.

Locarnini, R., Mishonov, A. V., Antonov, J. I., Boyer, T. P., and Garcia, H. E. (2006). Volume 1: Temperature. World Ocean Atlas 2005. S. Levitus, NOAA Atlas NESDIS 61, U. S. Goverment Printing Office, Washington, D. C.**:** 182 pp.

Lohmann, K., Drange, H., and Bentsen, M. (2009). "Response of the North Atlantic subpolar gyre to persistent North Atlantic oscillation like forcing." Climate dynamics **32**(2): 273-285.

Lowe, J. J., and Walker, M. J. C. (1997). Reconstructing Quaternary Environments, Second Edition, Addison Weasly Longman, Edinburgh, UK, xxii + 446 pp.

Lu, J., and Greatbatch, R. J. (2002). "The changing relationship between the NAO and northern hemisphere climate variability." Geophysical Research Letters **29**(7): 1148, doi:10.1029/2001GL014052.

Lund, D. C., Lynch-Stieglitz, J., and Curry W. B. (2006). "Gulf Stream density structure and transport during the past millennium." Nature **444**(7119): 601-604.

Luterbacher, J., Schmutz, C., Gyalistras, D., Xoplaki, E., and Wanner, H. (1999). "Reconstruction of Monthly NAO and EU Indices Back to AD 1675." Geophysical Research Letters **26**(17): 2745-2748.

Luterbacher, J., Xoplaki, E., Dietrich, D., Jones, P. D., Davies, T. D., Portis, D., Gonzalez-Rouco, J. F., von Storch, H., Gyalistras, D., Casty, C. and Wanner, H. (2002). "Extending North Atlantic Oscillation Reconstructions Back to 1500." Atmospheric Science Letters **2**(1-4): 114-124.

Mann, M. E. (2002a). Little Ice Age, ***in*** Volume 1, The Earth system: physical and chemical dimensions of global environmental change. Encyclopedia of Global Environmental Change. M. C. MacCracken, and J. S. Perry, John Wiley & Sons, Ltd, Chichester. **1:** 504-509.

Mann, M. E. (2002b). Medieval Climatic Optimum, ***in*** Volume 1, The Earth system: physical and chemical dimensions of global environmental change. Encyclopedia of Global Environmental Change. M. C. MacCracken, and J. S. Perry, John Wiley & Sons, Ltd, Chichester. **1:** 514-516.

Mann, M. E., and Jones, P. D. (2002). "2,000 Year Hemispheric Multi-proxy Temperaure Reconstructions." IGBP PAGES/World Data Center for Paleoclimatology, #2003-051, NOAA/NGDC Paleoclimatology Program, Boulder CO, USA.

Mann, M. E., and Jones, P. D. (2003). "Global surface temperatures over the past two millennia." Geophysical Research Letters **30**(15): 1820-1823.

Matthews, J. A., and Briffa, K. R. (2005). "THE 'LITTLE ICE AGE': RE-EVALUATION OF AN EVOLVING CONCEPT." Geografiska Annaler **87**(1): 17-36.

McCartney, M. S. (1992). "Recirculating components to the deep boundary current of the northern North Atlantic." Progress In Oceanography **29**: 283-383.

McCartney, M. S., and Talley, L. D. (1982). "The Subpolar Mode Water of the North Atlantic Ocean." Journal of Physical Oceanography **12**(11): 1169-1188.

McCave, I. N. (2005). 8: Sedimentary processes: Deposition from Suspension, in Encyclopedia of Geology, Elsevier Academic Press, Oxford, UK.

McCave, I. N., and Hall, I. R. (2006). "Size sorting in marine muds: Processes, pitfalls, and prospects for paleoflow-speed proxies." Geochemistry Geophysics Geosystems. **7**(10): Q10N05, doi:10.1029/2006GC001284.

McCave, I. N., Manighetti, B., and Robinson, S. G. (1995). "Sortable Silt and Fine Sediment Size/Composition Slicing: Parameters for Palaeocurrent Speed and Palaeoceanography." Paleoceanography **10**(3): 593-610.

McCrea, J. M. (1950). "On the Isotopic Chemistry of Carbonates and a Paleotemperature Scale." The Journal of Chemical Physics **18**(6): 849-857.

McManus, J. F., Francois, R., Gherardi, J. M., Keigwin, L. D., and Brown-Leger, S. (2004). "Collapse and rapid resumption of Atlantic meridional circulation linked to deglacial climate changes." Nature **428**(6985): 834-837.

Miller, K. G., and Tucholke, B. E. (1983). Development of Cenozoic abyssal circulation south of the Greenland-Scotland Ridge, in *Marine Sciences, Structure and Development of the Greenland-Scotland Ridge*: *New Methods and Concepts*. NATO Confernece Series, Marine Sciences, vol IV. M. H. P. Bott, et al. New York. **8:** 549-589.

Mortyn, P. G., and Charles, C. D. (2003). "Planktonic foraminiferal depth habitat and $\delta^{18}O$ calibrations: Plankton tow results from the Atlantic sector of the Southern Ocean." Paleoceanography **18**(2): 1037, doi:10.1029/2001PA000637.

Naidu, P. D. and N. Niitsuma (2004). "Atypical $\delta^{13}C$ signature in *Globigerina bulloides* at the ODP site 723A (Arabian Sea): implications of environmental changes caused by upwelling." Marine Micropaleontology **53**(1-2): 1-10.

Nesje, A., and Dahl S. O. (2003). "The'Little Ice Age'-only temperature?" The Holocene **13**(1): 139-145.

Nesje, A., Dahl, S., Thun, T., and Nordli, Ø (2007). "The 'Little Ice Age' glacial expansion in western Scandinavia: summer temperature or winter precipitation?" Climate dynamics **30**(7): 789-801.

Nesje, A., Jansen, E., Birks, H. J. B., Bjune, A. E., Bakke, J., Anderson, D. C., Dahl, S. O., Klitgaard-Kristensen, D., Lauritzen, S.-E., Lie, Ø., Risebrobakken, B., and Svendsen J. I. (2005). Holocene climate variability in the Northern North Atlantic region: a review of marine and terrestrial evidence. In: The Nordic Seas: An Integrated Perspective. H. Drange, Dokken, T. M., Furevik, T., Gerdes, R., and Berger, W., AGU Monograph 158, American Geophysical Union, Washington DC 289-321.

Niebler, H.-S., Hubberten, H.-W. and Gersonde, R. (1999). Oxygen Isotope Values of Planktic Foraminifera: A Tool for the Reconstruction of Surface Water Stratification. Use of Proxies in Paleoceanography: Examples from the South Atlantic. G. Fischer, and Wefer G., Springer-Verlag, Berlin, Heidelberg**:** 165-189, 735 pp.

Ninnemann, U., Dokken, T., Berge, H., Bryan, S., Tiessen, S., Euler, C., Lobegeier, M., Monsen, S., Pedersen, S., Peeters, F., Strømsø, J., and Yu, J. (2006). Cruise Report R/V *G.O. Sars*. UiB Cruise No: GS06-144, Leg 1, Department of Earth Science & Bjerknes Centre for Climate Research, University of Bergen, Norway.

Nyland, B. F., Jansen, E., Elderfield, H., and Andersson, C. (2006). "*Neogloboquadrina pachyderma* (dex. and sin.) Mg/Ca and $\delta^{18}O$ records from the Norwegian Sea." Geochemistry Geophysics Geosystems **7**: Q10P17, doi:10.1029/2005GC001055.

Olney, M. (2002). " Foraminifera." Micropalaeontology Unit, An insight into micropalaeontology: MIRACLE - Microfossil Image Recovery And Circulation and Education Retrieved 22.01, 2009, from http://images.google.no/imgres?imgurl=http://www.ucl.ac.uk/GeolSci/micropal/images/fora/fora007.gif&imgrefurl=http://www.ucl.ac.uk/GeolSci/micropal/foram.html&usg=__3zw-WP6N60g-ZCT1g_Egv1guNd0=&h=457&w=450&sz=60&hl=no&start=2&um=1&tbnid=h52qJ_L_pAN6RM:&tbnh=128&tbnw=126&prev=/images%3Fq%3Dgloborotalia%2Binflata%26um%3D1%26hl%3Dno%26client%3Dfirefox-a%26rls%3Dorg.mozilla:nb-NO:official%26sa%3DN.

Olsen, S. M., Hansen, B., Quadfasel, D., and Østerhus, S. (2008). "Observed and modelled stability of overflow across the Greenland-Scotland ridge." Nature **455**(7212): 519-522.

Oppo, D. W., McManus, J. F., and Cullen, J. L. (2003). "Palaeo-oceanography: Deepwater variability in the Holocene epoch." Nature **422**(6929): 277-277.

Ortiz, J. D., Mix, A. C., Rugh, W., Watkins, J. M., and Collier, R. W. (1996). "Deep-dwelling planktonic foraminifera of the northeastern Pacific Ocean reveal environmental control of oxygen and carbon isotopic disequilibria." Geochimica et Cosmochimica Acta **60**(22): 4509-4523.

Ortlieb, L., Escribano R., Follegati R., Zuñiga, O., Kong, I., Rodriguez L., Valdes J., Guzman N., and Iratchet P. (2000). "Recording of ocean-climate changes during the last 2,000 years in a hypoxic marine environment off northern Chile (23° S)." Revista chilena de historia natural **73**: 221.

Orvik, K. A., and Niiler, P. (2002). "Major pathways of Atlantic water in the northern North Atlantic and Nordic Seas toward Arctic." Geophysical Research Letters **29**(19): 1896.

Pak, D. K., and Kennett, J. P. (2002). "A FORAMINIFERAL ISOTOPIC PROXY FOR UPPER WATER MASS STRATIFICATION." Journal of foraminiferal research **32**(3): 319-327.

Peeters, F. J. C. (2007). "Scanning Electron Microscope (S.E.M.) image of planktic foraminifera " PLANKTIC FORAMINIFERA: S.E.M. IMAGES Retrieved 21.01.09, 2009, from http://www.geo.vu.nl/~peef/photography/foraminifera/files/page1-2000-full.html

Pflaumann, U., Duprat, J., Pujol, C. and Labeyrie, L. D. (1996). "SIMMAX: A Modern Analog Technique to Deduce Atlantic Sea Surface Temperatures from Planktonic Foraminifera in Deep-Sea Sediments." Paleoceanography **11**: 15-35.

Pinet, P. R. (2006). Invitation to Oceanography, 4th edition. D. W. DeChambeau, Jones & Bartlett Publishers, Inc.**:** 594 pp.

Rahmstorf, S. (2002). "Ocean circulation and climate during the past 120,000 years." Nature **419**(6903): 207-214.

Rahmstorf, S. (2006). Thermohaline Ocean Circulation. Encyclopedia of Quaternary Sciences. S. A. Elias, Elsevier, Amsterdam.

Reverdin, G., Niiler, P. P., and Valdimarsson, H. (2003). "North Atlantic Ocean surface currents." Journal of Geophysical Research **108**(C1): 3002, doi:10.1029/2001JC001020.

Rossby, T. (1996). "The North Atlantic Current and Surrounding Waters: At the Crossroads." Reviews of Geophysics **34**(4): 463-481.

Ruddiman, W. F. (1972). "Sediment Redistribution of the Reykjanes Ridge; Seismic Evidence." Geological Society of America bulletin **83**(7): 2039.

Ruddiman, W. F. (2001). Earth's climate: Past and Future. M. Wallerstein, Folchetti, N., and B. Brooks, W. H. Freeman and Company, New York, U. S.**:** 465 pp.

Sarnthein, M., Winn, K., Jung, S. J. A., Duplessy, J., Labeyrie, L., Erlenkeuser, H., and Ganssen, G. (1994). "Changes in East Atlantic Deepwater Circulation Over the Last 30,000 years: Eight Time Slice Reconstructions." Paleoceanography **9**(2): 209-267.

Sautter, L. R., Thunell, R. C. (1991). "Seasonal Variability in the $\delta^{18}O$ and $\delta^{13}C$ of Planktonic Foraminifera from an Upwelling Environment: Sediment Trap Results from the San Pedro Basin, Southern California Bight." Paleoceanography **6**(3): 307-334.

Schlitzer, R. (2000). "Electronic Atlas of WOCE Hydrographic and Tracer Data Now Available." Eos Trans., AGU **81**(5): 45p.

Schlitzer, R. (2009). "Ocean Data View." Retrieved 31.06, 2009, from http://odv.awi.de.

Schmidt, G. A., Bigg, G. R., and Rohling, E. J. (1999). "Global Seawater Oxygen-18 Database." Retrieved 29.04, 2009, from http://data.giss.nasa.gov/o18data.

Schmitz, W. J. J., and McCartney, M. S. (1993). "On the North Atlantic Circulation." Reviews of Geophysics **31**(1): 29-43.

Shackleton, N. J. (1974). "Attainment of isotopic equilibrium between ocean water and benthonic foraminifera genus *Uvigerina*: Isotopic changes in the ocean during the last glacial " Coll Internat Centr Nat Tech Sci **219**: 203-210.

Sharp, Z. (2007). Chapter 2: Terminology, standards, and mass spectrometry. Stable Isotope Geochemistry, Pearson Prentice Hall, Pearson Education, Inc., U. S.

Simstich, J., Sarnthein, M., Erlenkeuser, H. (2003). "Paired $\delta^{18}O$ signals of *Neogloboquadrina pachyderma* (s) and Turborotalita quinqueloba show thermal stratification structure in Nordic Seas." Marine Micropaleontology **48**(1-2): 107-125.

Smith, W. H. F., and Sandwell, D. T. (1997). "Global Sea Floor Topography from Satellite Altimetry and Ship Depth Soundings." Science **277**(5334): 1956-1962.

Solomon, S., Qin, D., Manning, M., Alley, R. B., Berntsen, T, Bindoff, N. L., Chen, Z., Chidthaisong, A., Gregory, J. M., Hegerl, G. C., Heimann, M., Hewitson, B., Hoskins, B. J., Joos, F., Jouzel, J., Kattsov, V., Lohmann, U., Matsuno, T., Molina, M., Nicholls, N., Overpeck, J., Raga, G., Ramaswamy, V., Ren, J., Rusticucci, M., Somerville, R., Stocker, T. F., Whetton, P., Wood, R. A., and Wratt, D. (2007). Technical Summary. Climate Change 2007: The Physical Science Basis, Contribution of Working Group 1 to the Fourth Assessment Report of Intergovernmental Panel on Climate Change. S. Solomon, D. Quin, M. Manning, Z. Chen, M. Marquis, K. B. Averyt, M. Tignor, and H. L. Miller, Cambridge University Press, Cambridge, United Kingdom and New York, NY, USA.

Spero, H. J., and Lea, D. W. (1996). "Experimental determination of stable isotope variability in *Globigerina bulloides*: implications for paleoceanographic reconstructions." Marine Micropaleontology **28**(3-4): 231-246.

Stow, D. A. V., Faugères, J. C., Howe, J. A., Pudsey, C. J., and Viana, A. R. (2002). "Bottom currents, contourites and deep-sea sediment drifts: current state-of-the-art." Geological Society, London, Memoirs **22**(1): 7-20.

Stuiver, M., and Reimer P. J. (1993). "Extended ^{14}C Data Base and Revised CALIB 3.0 ^{14}C age Calibration." Radiocarbon **35**(1): 215-230.

Sutton, R. T., and Hodson, D. L. R. (2005). "Atlantic Ocean Forcing of North American and European Summer Climate." Science **309**(5731): 115-118.

Talley, L. D. (1996). "North Atlantic circulation and variability, reviewed for the CNLS conference." Physica D: Nonlinear Phenomena **98**(2-4): 625-646.

Tett, S., Betts, R., Crowley, T., Gregory, J., Johns, T., Jones, A., Osborn, T., Öström, E., Roberts, D., and Woodage, M. (2006). "The impact of natural and anthropogenic forcings on climate and hydrology since 1550." Climate dynamics **28**(1): 3-34.

Thornalley, D. J. R., Elderfield, H., and McCave, I. N. (2009). "Holocene oscillations in temperature and salinity of the surface subpolar North Atlantic." Nature **457**(7230): 711-714.

Tolderlund, D. S. and A. W. H. Be (1972). "Seasonal distribution of planktonic foraminifera in the western North Atlantic." Micropaleontology **17**(3): 297-329.

Urey, H. C. (1947). "The thermodynamic properties of isotopic substances." Journal of Chemical Society: 562-581.

Urey, H. C. (1948). "Oxygen Isotopes in Nature and in the Laboratory." Science **108**(2810): 489-496.

Urey, H. C., Lowenstam H. A., Epstein S., and McKinney C. R. (1951). "Measurement of paleotemperatures and temperatures of the upper Cretaceous of England, Denmark, and the southeastern United States." Geological Society of America bulletin **62**(4): 399-416.

van Aken, H. M., and Eisma D. (1987). "The circulation between Iceland and Scotland derived from water mass analysis." Netherlands Journal of Sea Research **21**(1): 1-15.

van Aken, H. M., Becker, G. (1996). "Hydrography and through-flow in the north-eastern North Atlantic Ocean: the NANSEN project." Progress In Oceanography **38**(4): 297-346.

Wefer, G., Berger, W. H. (1991). "Isotope paleontology: growth and composition of extant calcareous species." Marine Geology **100**(1-4): 207-248.

Wold, C. N. (1994). "Cenozoic sediment accumulation on drifts in the northern North Altantic." Paleoceanography **9**(6): 917-941

Wu, G., and Hillaire-Marcel, C. (1994). "Oxygen isotope compositions of sinistral Neogloboquadrina pachyderma tests in surface sediments: North Atlantic Ocean." Geochimica et Cosmochimica Acta **58**(4): 1303-1312.

Zhang, R., and Delworth, T. L. (2006). "Impact of Atlantic multidecadal oscillations on India/Sahel rainfall and Atlantic hurricanes." Geophysical Research Letters **33**: L17712, doi:10.1029/2006GL026267.

APPENDIX

Appendix A

Table A: Sortable silt mean grain-size measurements. Numbers in red are from the first run, which is not used in this study.

Depth (cm)	1 Mean	2 Mean	3 Mean	Averge of 2 & 3
0,00	16,82	17,08	17,78	17,43
0,50	17,19	16,95	17,83	17,39
1,00	17,28	17,70	17,09	17,40
1,50	17,42	17,49	18,11	17,80
2,00	17,01	18,61	17,86	18,24
2,50	17,63	18,53	18,56	18,55
3,00	20,31	18,33	19,05	18,69
3,50	17,99	18,57	18,50	18,54
4,00	17,65	18,14	18,37	18,26
4,50	16,65	18,09	17,93	18,01
5,00	18,54	18,13	17,89	18,01
5,50	16,98	16,93	17,61	17,27
6,00	17,46	18,50	18,85	18,67
6,50	16,89	17,75	18,11	17,93
7,00	17,24	17,94	18,33	18,13
7,50	16,77	19,56	17,96	18,76
8,00	17,53	18,46	18,57	18,52
8,50	18,91	19,29	19,60	19,45
9,00	18,19	17,32	17,85	17,58
9,50	18,38	18,07	17,52	17,79
10,00	17,68	18,38	18,73	18,55
10,50	17,37	17,92	18,53	18,23
11,00	18,05	18,77	17,85	18,31
11,50	17,22	19,02	18,23	18,62
12,00	17,46	17,99	18,12	18,06
12,50	18,40	18,30	18,80	18,55
13,00	18,95	18,36	18,24	18,30
13,50	18,53	18,39	18,37	18,38
14,00	17,98	18,30	18,71	18,51
14,50	17,46	18,02	18,72	18,37
15,00				
15,50	17,40	17,75	18,43	18,09
16,00	18,33	18,82	18,32	18,57
16,50	17,96	18,71	18,99	18,85
17,00	17,97	18,43	19,13	18,78

17,50	18,16	20,77	18,84	19,80
18,00	18,45	18,58	18,85	18,72
18,50	18,32	19,48	18,25	18,87
19,00	18,81	18,68	18,94	18,81
19,50	17,94	18,81	18,90	18,86
20,00	17,52	19,04	18,28	18,66
20,50	17,72	18,62	18,88	18,75
21,00	17,94	19,01	18,91	18,96
21,50	18,42	17,69	18,81	18,25
22,00	18,07	19,07	18,81	18,94
22,50	18,08	18,80	18,11	18,46
23,00	18,09	18,73	18,46	18,59
23,50	18,50	18,28	18,38	18,33
24,00	18,14	18,17	18,60	18,39
24,50	18,37	17,91	17,57	17,74
25,00	17,97	18,74	18,14	18,44
25,50	18,03	18,79	18,89	18,84
26,00	18,06	18,30	19,15	18,72
26,50	18,37	18,25	19,10	18,67
27,00	18,33	17,90	18,75	18,32
27,50	18,81	18,89	19,08	18,98
28,00	18,61	18,83	18,66	18,75
28,50	18,51	18,93	19,22	19,07
29,00	17,99	18,62	18,93	18,78
29,50	17,88	19,09	19,29	19,19
30,00	18,24	18,47	18,46	18,47
30,50	19,23	17,83	18,52	18,17
31,00	18,03	18,61	18,80	18,70
31,50	17,99	18,20	18,24	18,22
32,00	18,35	17,75	18,57	18,16
32,50	17,92	18,77	17,76	18,26
33,00	16,90	17,19	18,05	17,62
33,50	18,47	17,92	18,55	18,23
34,00	19,22	18,38	18,77	18,58
34,50	17,36	18,08	18,06	18,07
35,00	18,02	18,23	18,11	18,17
35,50	17,85	17,74	18,51	18,13
36,00	17,36	19,26	17,59	18,43
36,50	18,51	18,49	18,48	18,48
37,00	18,59	19,68	18,25	18,96
37,50	18,01	17,96	18,40	18,18
38,00	18,39	18,90	18,52	18,71
38,50	18,06	18,57	18,72	18,65

39,00	18,45	18,16	18,62	18,39
39,50	18,42	18,26	17,98	18,12
40,00	17,32	18,51	18,88	18,69
40,50	17,77	19,35	18,85	19,10
41,00	18,30	18,74	18,40	18,57
41,50	18,00	18,94	18,89	18,91
42,00	17,22	18,66	18,73	18,69
42,50	17,22	18,17	18,74	18,46
43,00	18,54	18,43	19,38	18,90
43,50	18,18	18,80	19,33	19,06
44,00	17,80	18,43	19,22	18,83

Appendix B

Table B.1: *G. bulloides*. Numbers in red indicate all the samples measured on MAT 251

Depth (cm)	1 $\delta^{13}C$ (GB)	2 $\delta^{13}C$ (GB)	Average $\delta^{13}C$ (GB)	1 $\delta^{18}C$ (GB)	2 $\delta^{18}C$ (GB)	Average $\delta^{18}O$ (GB)
0,00	-0,65	-0,34	-0,50	1,35	1,66	1,51
0,50	-0,74		-0,74	1,66		1,66
1,00	0,04	0,06	0,05	1,64	1,76	1,70
1,50	-0,58	-0,03	-0,31	1,50	1,83	1,67
2,00	0,01	-0,12	-0,06	1,78	1,65	1,72
2,50	-0,11	-0,51	-0,31	1,91	1,59	1,75
3,00	-0,02	0,04	0,01	2,01	1,98	2,00
3,50	-0,13	-0,25	-0,19	1,55	1,66	1,61
4,00	0,25	-0,02	0,12	1,94	1,86	1,90
4,50	-0,53	-0,04	-0,29	1,64	1,82	1,73
5,00	0,21	0,19	0,20	1,95	1,92	1,94
5,50	0,23	-0,13	0,05	1,83	1,74	1,79
6,00	-0,52	-0,07	-0,30	1,34	1,91	1,63
6,50	0,03	0,13	0,08	1,93	1,77	1,85
7,00	-0,28	0,29	0,01	1,61	1,91	1,76
7,50	0,29	0,25	0,27	1,96	1,93	1,95
8,00	-0,07	0,12	0,03	2,05	1,85	1,95
8,50	0,12	-0,10	0,01	1,96	1,77	1,87
9,00	-0,04	0,08	0,02	1,81	1,91	1,86
9,50	-0,40	-0,02	-0,21	1,61	1,97	1,79
10,00	-0,12	0,03	-0,05	1,85	1,91	1,88
10,50	-0,34	-0,22	-0,28	1,81	1,75	1,78
11,00	-0,01		-0,01	1,79		1,79
11,50	-0,13	-0,37	-0,25	1,80	1,77	1,79
12,00	-0,44	-0,22	-0,33	1,58	1,76	1,67
12,50	-0,48	0,23	-0,13	1,49	1,72	1,61
13,00	0,02		0,02	1,93		1,93
13,50	-0,33	0,17	-0,08	1,79	2,04	1,92
14,00	-0,06	0,15	0,05	1,64	2,02	1,83
14,50		0,03	0,03		1,86	1,86
15,00	-0,05	-0,02	-0,04	1,86	1,57	1,72
15,50	-0,27	-0,43	-0,35	1,67	1,81	1,74
16,00	-0,07	-0,03	-0,05	1,85	1,72	1,79
16,50	-0,26	-0,27	-0,27	1,59	1,86	1,73
17,00	-0,13	-0,27	-0,20	1,57	1,79	1,68
17,50	0,22	-0,11	0,06	1,77	1,95	1,86
18,00	-0,25	-0,14	-0,20	1,64	1,94	1,79
18,50	-0,41	-0,15	-0,28	1,45	2,00	1,73

19,00	-0,28	-0,36	-0,32	1,66	1,57	1,62
19,50	-0,10	-0,11	-0,11	1,57	1,66	1,62
20,00	0,05	0,09	0,07	1,75	1,77	1,76
20,50	-0,08	-0,52	-0,30	1,52	1,51	1,52
21,00	0,01	-0,07	-0,03	1,75	1,65	1,70
21,50	-0,23	-0,09	-0,16	1,63	1,50	1,57
22,00	-0,11	-0,30	-0,21	1,75	1,59	1,67
22,50	-0,17	-0,44	-0,31	1,72	1,50	1,61
23,00	-0,45	-0,09	-0,27	1,72	1,64	1,68
23,50	0,00	-0,18	-0,09	1,88	1,43	1,66
24,00		-0,29	-0,29		1,49	1,49
24,50	-0,05	-0,52	-0,29	1,75	1,57	1,66
25,00	-0,30	-0,02	-0,16	1,71	1,85	1,78
25,50	-0,17	0,11	-0,03	1,83	1,75	1,79
26,00	-0,06	-0,11	-0,09	1,75	1,68	1,72
26,50	0,13	-0,08	0,03	1,51	1,65	1,58
27,00	-0,46	-0,31	-0,39	1,45	1,65	1,55
27,50	0,17	-0,69	-0,26	1,67	1,61	1,64
28,00	-0,20	-0,50	-0,35	1,77	1,59	1,68
28,50	-0,16	-0,20	-0,18	1,69	1,71	1,70
29,00	-0,44	-0,22	-0,33	1,72	1,77	1,75
29,50	-0,50	0,08	-0,21	1,47	1,90	1,69
30,00	0,05	-0,52	-0,24	1,83	1,62	1,73
30,50	-0,07	-0,40	-0,24	1,75	1,62	1,69
31,00	0,06	-0,04	0,01	1,69	1,78	1,74
31,50	-0,05	-0,12	-0,09	1,61	1,63	1,62
32,00	-0,33	-0,19	-0,26	1,50	1,90	1,70
32,50	-0,33	-0,18	-0,26	1,77	1,78	1,78
33,00	-0,36	0,13	-0,12	1,53	1,62	1,58
33,50	-0,11	-0,18	-0,15	1,75	1,86	1,81
34,00	-0,05	-0,15	-0,10	1,74	1,61	1,68
34,50	-0,09	-0,08	-0,09	1,93	1,67	1,80
35,00	-0,18	-0,54	-0,36	1,72	1,74	1,73
35,50	-0,06	-0,35	-0,21	1,73	1,46	1,60
36,00	-0,01	-0,10	-0,06	1,68	1,75	1,72
36,50	-0,19	0,11	-0,04	1,57	1,61	1,59
37,00	-0,23	-0,49	-0,36	1,60	1,36	1,48
37,50	-0,52	0,10	-0,21	1,65	1,79	1,72
38,00	-0,05	-0,20	-0,13	1,78	1,60	1,69
38,50	0,02	-0,35	-0,17	1,82	1,76	1,79
39,00	-0,12	0,06	-0,03	1,80	1,86	1,83
39,50	-0,08	-0,46	-0,27	1,84	1,55	1,70
40,00	-0,42	-0,49	-0,46	1,51	1,39	1,45

40,50	-0,31	-0,27	-0,29	1,46	1,73	1,60
41,00	0,10	0,05	0,08	1,89	1,87	1,88
41,50	-0,34	-0,12	-0,23	1,77	1,60	1,69
42,00	-0,40	-0,13	-0,27	1,55	1,78	1,67
42,50	-0,27	-0,23	-0,25	1,60	1,61	1,61
43,00	0,05	-0,21	-0,08	1,89	1,51	1,70
43,50	-0,31	-0,91	-0,61	1,80	1,41	1,61
44,00	-0,33	-0,14	-0,24	1,80	1,75	1,78
44,00		-0,46	-0,46		1,59	1,59

Table B.2: *N. pachyderma* (d).

Depth (cm)	**1 $\delta^{13}C$ (NPD)**	**2 $\delta^{13}C$ (NPD)**	**Average $\delta^{13}C$ (NPD)**	**1 $\delta^{18}C$ (NPD)**	**2 $\delta^{18}C$ (NPD)**	**Average $\delta^{18}O$ (NPD)**
0,00	0,29	0,40	0,34	1,67	1,57	1,62
0,50	0,31	0,25	0,28	1,47	1,51	1,49
1,00	0,51	0,46	0,49	1,44	1,62	1,53
1,50	0,69	0,64	0,66	1,71	1,52	1,62
2,00	0,56	0,46	0,51	1,50	1,53	1,52
2,50	0,54	0,48	0,51	1,45	1,56	1,51
3,00	0,42	0,54	0,48	1,48	1,59	1,54
3,50	0,45	0,47	0,46	1,60	1,56	1,58
4,00	0,47	0,75	0,61	1,61	1,65	1,63
4,50	0,68	0,24	0,46	1,63	1,58	1,61
5,00	0,55	0,31	0,43	1,58	1,53	1,56
5,50	0,59	0,65	0,62	1,43	1,52	1,48
6,00	0,79	0,61	0,70	1,72	1,42	1,57
6,50	0,63	0,62	0,62	1,61	1,54	1,58
7,00	0,69	0,40	0,55	1,68	1,50	1,59
7,50	0,66	0,75	0,71	1,61	1,58	1,60
8,00	0,55	0,63	0,59	1,62	1,66	1,64
8,50	0,35	0,53	0,44	1,50	1,73	1,62
9,00	0,56	0,60	0,58	1,70	1,72	1,71
9,50	0,48	0,59	0,53	1,65	1,66	1,66
10,00	0,67	0,66	0,67	1,74	1,67	1,71
10,50	0,53	0,42	0,47	1,67	1,49	1,58
11,00	0,27	0,55	0,41	1,52	1,49	1,51
11,50	0,62	0,29	0,45	1,65	1,37	1,51
12,00	0,52	0,35	0,44	1,60	1,38	1,49
12,50	0,45	0,57	0,51	1,37	1,62	1,50
13,00	0,79	0,36	0,58	1,71	1,50	1,61
13,50	0,36	0,53	0,44	1,49	1,58	1,54
14,00	0,51	0,56	0,53	1,65	1,54	1,60

14,50	0,63	0,53	0,58	1,56	1,64	1,60
15,00	0,50	0,37	0,44	1,58	1,49	1,54
15,50	0,65	0,43	0,54	1,63	1,66	1,65
16,00	0,43	0,47	0,45	1,55	1,37	1,46
16,50	0,65	0,59	0,62	1,58	1,61	1,60
17,00	0,37	0,54	0,46	1,36	1,51	1,44
17,50	0,54	0,58	0,56	1,72	1,52	1,62
18,00	0,49	0,43	0,46	1,55	1,44	1,50
18,50	0,63	0,50	0,56	1,59	1,70	1,65
19,00	0,29	0,38	0,33	1,33	1,42	1,38
19,50	0,40	0,35	0,37	1,58	1,35	1,47
20,00	0,34	0,49	0,42	1,33	1,54	1,44
20,50	0,39	0,41	0,40	1,49	1,74	1,62
21,00	0,30	0,28	0,29	1,30	1,36	1,33
21,50	0,46	0,43	0,44	1,34	1,45	1,40
22,00	0,32	0,32	0,32	1,47	1,45	1,46
22,50	0,55	0,41	0,48	1,35	1,44	1,40
23,00	0,37	0,35	0,36	1,49	1,37	1,43
23,50	0,53	0,49	0,51	1,62	1,59	1,61
24,00	0,43	0,51	0,47	1,37	1,48	1,43
24,50	0,46	0,50	0,48	1,22	1,50	1,36
25,00	0,44	0,39	0,41	1,55	1,57	1,56
25,50	0,41	0,46	0,44	1,61	1,58	1,60
26,00	0,41	0,58	0,50	1,54	1,70	1,62
26,50	0,36	0,42	0,39	1,56	1,37	1,47
27,00	0,27	0,37	0,32	1,36	1,46	1,41
27,50	0,42	0,62	0,52	1,58	1,69	1,63
28,00	0,56	0,35	0,46	1,67	1,50	1,59
28,50	0,46	0,50	0,48	1,57	1,66	1,62
29,00	0,41	0,57	0,49	1,65	1,63	1,64
29,50	0,45	0,56	0,51	1,43	1,69	1,56
30,00	0,42	0,49	0,45	1,52	1,64	1,58
30,50	0,56	0,45	0,50	1,56	1,62	1,59
31,00	0,72	0,45	0,58	1,78	1,55	1,67
31,50	0,29	0,34	0,31	1,50	1,63	1,57
32,00	0,46	0,32	0,39	1,61	1,49	1,55
32,50	0,22	0,57	0,40	1,48	1,69	1,59
33,00	0,33	0,51	0,42	1,45	1,65	1,55
33,50	0,34	0,35	0,34	1,49	1,60	1,54
34,00	0,21	0,37	0,29	1,40	1,61	1,50
34,50	0,55	0,57	0,56	1,66	1,52	1,59
35,00	0,61	0,31	0,46	1,64	1,47	1,55
35,50	0,35	0,49	0,42	1,38	1,53	1,46

36,00	0,55	0,35	0,45	1,63	1,56	1,59
36,50	0,24	0,30	0,27	1,46	1,44	1,45
37,00	0,41	0,32	0,36	1,58	1,41	1,50
37,50	0,29		0,29	1,47		1,47
38,00	0,32	0,48	0,40	1,54	1,50	1,52
38,50	0,38	0,59	0,49	1,49	1,52	1,50
39,00	0,54	0,34	0,44	1,52	1,43	1,48
39,50	0,29	0,50	0,40	1,52	1,52	1,52
40,00	0,47	0,36	0,42	1,71	1,47	1,59
40,50	0,41	0,22	0,31	1,49	1,44	1,47
41,00	0,59	0,41	0,50	1,66	1,61	1,64
41,50	0,43	0,30	0,37	1,65	1,56	1,61
42,00	0,35	0,44	0,39	1,52	1,49	1,51
42,50	0,47	0,36	0,42	1,52	1,44	1,48
43,00	0,48	0,29	0,38	1,55	1,52	1,54
43,50	0,35	0,32	0,33	1,47	1,44	1,46
44,00	0,22	0,41	0,31	1,47	1,42	1,45

Table B.3: *G. inflata*.

Depth (cm)	**1 $\delta^{13}C$ (GI)**	**2 $\delta^{13}C$ (GI)**	**Average $\delta^{13}C$ (GI)**	**1 $\delta^{18}C$ (GI)**	**2 $\delta^{18}C$ (GI)**	**Average $\delta^{18}O$ (GI)**
0,00						
0,50						
1,00	0,91	0,94	0,93	1,86	1,96	1,91
1,50	0,93	0,90	0,92	1,88	1,92	1,90
2,00	0,93		0,93	1,92		1,92
2,50	0,81		0,81	1,98		1,98
3,00	1,13	0,91	1,02	2,05	2,01	2,03
3,50	1,00	1,09	1,05	1,95	2,08	2,02
4,00	0,85	0,89	0,87	1,93	1,91	1,92
4,50	1,12	0,86	0,99	2,00	1,85	1,93
4,50	1,05		1,05	1,93		1,93
5,00		1,15	1,15		1,99	1,99
5,00	0,90	1,17	1,04	1,87	1,99	1,93
5,50	1,01		1,01	2,17		2,17
5,50	0,90	1,06	0,98	1,88	1,88	1,88
6,00	1,15	0,94	1,05	1,99	1,95	1,97
6,50	0,93		0,93	1,97		1,97
7,00	1,25	1,25	1,25	2,02	2,03	2,03
7,50	0,93	1,04	0,99	1,96	1,86	1,91
8,00	1,17	1,24	1,21	1,83	2,03	1,93
8,50	1,08	1,11	1,10	2,07	2,05	2,06

9,00	1,18	0,95	1,07	1,99	1,86	1,93
9,50	1,06	0,92	0,99	1,83	1,95	1,89
10,00	1,03	0,89	0,96	2,09	1,74	1,92
10,50	1,25	0,76	1,01	1,97	1,70	1,84
11,00	1,07	0,84	0,96	1,96	1,78	1,87
11,50	0,99	1,24	1,12	1,78	1,89	1,84
12,00	1,13	1,05	1,09	1,96	1,80	1,88
12,50	0,94	1,07	1,01	1,61	2,06	1,84
13,00	0,92	0,81	0,87	1,92	1,81	1,87
13,50	1,04	1,03	1,04	1,88	1,83	1,86
14,00	0,72	0,81	0,77	1,58	1,54	1,56
14,50	0,84	1,08	0,96	1,67	1,89	1,78
15,00	0,84	0,85	0,85	1,60	1,82	1,71
15,50	0,84	1,03	0,94	1,87	2,07	1,97
16,00	0,65	0,68	0,67	1,63	1,76	1,70
16,50	0,99	0,86	0,93	1,78	1,73	1,76
17,00	0,95	0,99	0,97	1,81	1,88	1,85
17,50	1,11	0,97	1,04	1,93	1,95	1,94
18,00	0,81	0,77	0,79	1,76	1,76	1,76
18,50	0,75	0,98	0,87	1,80	1,91	1,86
19,00	0,97	1,09	1,03	1,74	1,97	1,86
19,50	0,88	0,99	0,94	1,75	1,84	1,80
20,00	0,80	1,07	0,94	1,77	1,71	1,74
20,50	0,80	0,97	0,89	1,66	1,82	1,74
21,00	0,81	0,84	0,83	1,70	1,79	1,75
21,50	0,77	0,74	0,76	1,69	1,68	1,69
22,00	0,94	0,78	0,86	1,89	1,69	1,79
22,50	0,94	0,81	0,88	1,84	1,79	1,82
23,00	1,11	0,80	0,96	2,07	1,80	1,94
23,50	0,84	0,86	0,85	1,95	1,90	1,93
24,00	0,95	0,94	0,95	2,02	1,82	1,92
24,50	0,85	0,69	0,77	1,85	1,89	1,87
25,00	0,91	0,89	0,90	1,85	1,89	1,87
25,50	0,91	0,71	0,81	1,80	1,71	1,76
26,00	0,95	0,94	0,95	1,90	1,99	1,95
26,50	0,93	0,88	0,91	1,83	1,86	1,85
27,00	0,78	0,95	0,87	1,99	1,87	1,93
27,50	0,94	0,98	0,96	1,95	1,89	1,92
28,00	0,97	1,01	0,99	1,99	1,92	1,96
28,50	0,79	0,80	0,80	1,75	1,84	1,80
29,00	1,02	1,06	1,04	1,83	1,95	1,89
29,50	1,04	0,85	0,95	1,94	1,98	1,96
30,00	0,90	0,93	0,92	1,87	1,91	1,89

30,50	0,72	0,90	0,81	1,82	1,98	1,90
31,00	0,99	0,93	0,96	2,08	1,91	2,00
31,50	0,70	1,11	0,91	1,80	1,83	1,82
32,00	0,95	0,87	0,91	2,05	1,89	1,97
32,50	0,87	0,94	0,91	1,86	1,94	1,90
33,00	0,74	0,84	0,79	1,84	1,73	1,79
33,50	0,96	0,90	0,93	1,89	1,93	1,91
34,00	1,00	0,83	0,92	1,94	1,87	1,91
34,50	0,92	0,88	0,90	1,68	1,68	1,68
35,00	0,90	1,01	0,96	1,80	1,74	1,77
35,50	1,14	0,79	0,97	1,94	1,78	1,86
36,00	1,03	0,97	1,00	1,96	2,08	2,02
36,50	1,09	1,11	1,10	2,12	2,11	2,12
37,00	1,07	0,89	0,98	2,05	1,97	2,01
37,50	0,91	0,99	0,95	1,95	1,72	1,84
38,00	0,76	0,98	0,87	1,73	1,93	1,83
38,50		0,90	0,90		2,00	2,00
39,00	0,84	0,70	0,77	1,78	1,74	1,76
39,50	0,83	0,91	0,87	1,76	1,90	1,83
40,00	0,85	0,93	0,89	1,71	1,78	1,75
40,50	1,12	0,64	0,88	1,94	1,72	1,83
41,00	0,98	1,06	1,02	1,85	1,93	1,89
41,50	0,85	0,95	0,90	1,65	2,05	1,85
42,00	1,04	1,01	1,03	1,91	1,94	1,93
42,50	0,89	0,92	0,91	1,78	1,77	1,78
43,00	0,99	0,82	0,91	1,97	1,76	1,87
43,50	0,89	0,99	0,94	1,85	1,71	1,78
44,00	0,90	1,04	0,97	1,78	1,90	1,84

Appendix C

Table C: *C. wuellerstorfi*.

Depth (cm)	1 $\delta^{13}C$ (CW)	2 $\delta^{13}C$ (CW)	Average $\delta^{13}C$ (CW)	1 $\delta^{18}C$ (CW)	2 $\delta^{18}C$ (CW)	Average $\delta^{18}O$ (CW)
0,00	1,14	1,08	1,11	2,90	2,79	2,85
1,00	1,14		1,14	3,03		3,03
2,50	1,04		1,04	2,87		2,87
3,50	1,07			2,88		
4,00	1,11	1,00	1,05	3,01	2,97	2,99
4,50	0,89	1,09	0,99	2,94	2,95	2,94
5,50	1,06		1,06	2,88		2,88
6,00	1,13		1,13	2,90		2,90
7,50	1,14		1,14	2,98		2,98
8,50	0,78		0,78	2,97		2,97
9,50	1,37		1,37	2,92		2,92
11,00	0,70		0,70	2,89		2,89
19,00	0,90		0,90	2,82		2,82
19,50	1,13		1,13	2,93		2,93
22,00	1,09		1,09	2,77		2,77
23,50	0,98	1,03	1,00	2,79	2,85	2,82
24,00	0,87		0,87	2,80		2,80
30,00	1,25		1,25	2,75		2,75
31,50	0,96		0,96	2,79		2,79
32,00	1,17		1,17	2,82		2,82
32,50	1,36		1,36	2,91		2,91
33,00	1,15		1,15	2,75		2,75
34,00	0,40	0,78	0,59	2,95	2,79	2,87
34,50	1,16	1,21	1,18	2,76	2,75	2,76
35,00	1,19	1,26	1,23	2,87	2,72	2,80
36,00	0,93		0,93	2,90		2,90
38,00	0,18		0,18	2,82		2,82
39,00	1,12		1,12	2,71		2,71
40,50	1,07		1,07	2,99		2,99
42,00	1,26		1,26	2,92		2,92

Appendix D

Table D.1: *G. bulloides*

Depth (cm)	$\delta^{13}C$ (GB)	$\delta^{18}O$(GB)	Depth (cm)	$\delta^{13}C$ (GB)	$\delta^{18}O$(GB)
0,00			36,00		1,78
1,00	-0,04		37,00	-0,77	
2,00	-0,06	1,55	38,00	-0,44	1,34
3,00	-0,25	1,75	39,00	-0,62	1,57
4,00	0,12	1,26	40,00	-0,46	1,51
5,00		1,60	41,00	-0,28	1,61
6,00	-0,14	1,71	42,00	-0,13	1,72
7,00	-0,47	1,75	43,00	-0,40	1,89
8,00	-0,11	1,50	44,00	-0,17	1,63
9,00	-0,25	1,67	45,00	-0,21	1,63
10,00	-0,05	1,33	46,00	-0,45	1,68
11,00	-0,01	1,58	47,00		1,47
12,00	-0,18	1,89	48,00	-0,27	
13,00	0,07	1,61	49,00	-0,35	1,58
14,00	-0,43	1,64	50,00	-0,44	1,61
15,00	-0,16	1,56	51,00	-0,21	1,72
16,00	0,09	1,58	52,00	-0,15	1,76
17,00	-0,37	1,80	53,00	-0,38	1,86
18,00	-0,42	1,38	54,00	-0,34	1,76
18,00	-0,09	1,77	55,00	0,02	1,57
20,00	-0,25	1,56	56,00	-0,23	1,53
21,00	-0,04	1,50	57,00	0,04	1,73
22,00	0,23	1,68	58,00	-0,07	1,63
23,00	-0,25	1,87	59,00	-0,26	1,65
24,00	-0,45	1,79	60,00	-0,24	1,71
25,00	-0,26	1,49	61,00	-0,54	1,48
26,00	-0,33	1,83	62,00	-0,18	1,55
27,00	-0,51	1,62	63,00	-0,28	1,71
28,00	0,05	1,43	64,00	-0,14	1,68
29,00	-0,04	1,82	65,00	-0,21	1,66
30,00		1,55	66,00	-0,23	1,77
31,00	-0,39		67,00	0,15	1,62
32,00		1,51	68,00	-0,21	1,88
33,00	-0,01		69,00	-0,17	1,36
34,00	-0,27	1,40	70,00	0,01	1,63
35,00	-0,10	1,25	71,00		1,67

Table D.2: *N. pachyderma* (d)

Depth (cm)	1 $\delta^{13}C$ (NPD)	2 $\delta^{13}C$ (NPD)	Average $\delta^{13}C$ (NPD)	1 $\delta^{18}C$ (NPD)	2 $\delta^{18}C$ (NPD)	Average $\delta^{18}O$ (NPD)
0,00	0,59	0,44	0,52	1,64	1,52	1,58
1,00	0,35	0,68	0,52	1,44	1,66	1,55
2,00	0,40	0,54	0,47	1,47	1,67	1,57
3,00	0,46	0,58	0,52	1,54	1,72	1,63
4,00	0,44	0,39	0,42	1,69	1,49	1,59
5,00	0,52	0,58	0,55	1,72	1,72	1,72
6,00	0,50	0,31	0,41	1,49	1,51	1,50
7,00	0,45	0,60	0,53	1,54	1,94	1,74
8,00	0,40	0,47	0,44	1,55	1,53	1,54
9,00	0,54	0,58	0,56	1,58	1,62	1,60
10,00	0,57	0,52	0,55	1,64	1,55	1,60
11,00	0,37	0,36	0,37	1,43	1,44	1,43
12,00	0,48	0,41	0,45	1,57	1,57	1,57
13,00	0,48	0,35	0,42	1,67	1,49	1,58
14,00	0,44	0,52	0,48	1,54	1,57	1,56
15,00	0,27	0,23	0,25	1,65	1,61	1,63
16,00	0,40	0,41	0,41	1,61	1,56	1,59
17,00	0,47	0,50	0,49	1,62	1,74	1,68
18,00	0,27	0,48	0,38	1,59	1,72	1,65
18,00	0,53	0,39	0,46	1,70	1,55	1,62
20,00	0,31	0,54	0,43	1,53	1,61	1,57
21,00	0,20	0,26	0,23	1,49	1,58	1,54
22,00	0,36	0,50	0,43	1,55	1,66	1,61
23,00	0,33	0,25	0,25	1,55	1,62	1,62
24,00	0,40	0,24	0,32	1,63	1,46	1,55
25,00	0,31	0,25	0,28	1,53	1,46	1,50
26,00	0,53	0,42	0,48	1,52	1,51	1,51
27,00	0,55	0,35	0,45	1,75	1,49	1,62
28,00	0,38	0,29	0,34	1,53	1,46	1,50
29,00	0,40	0,18	0,29	1,51	1,48	1,50
30,00	0,33	0,44	0,39	1,52	1,58	1,55
31,00	0,36	0,53	0,45	1,51	1,68	1,60
32,00	0,43	0,40	0,42	1,54	1,62	1,58
33,00	0,33	0,56	0,45	1,56	1,82	1,69
34,00	0,42	0,10	0,26	1,62	1,55	1,59
35,00	0,43	0,14	0,29	1,51	1,43	1,47
36,00	0,14	0,44	0,29	1,53	1,67	1,60
37,00	0,43	0,30	0,30	1,75	1,63	1,63
38,00	0,39	0,44	0,42	1,56	1,53	1,54

39,00	0,55	0,40	0,48	1,69	1,61	1,65
40,00	0,34	0,53	0,44	1,40	1,88	1,64
41,00	0,50	0,15	0,33	1,87	1,55	1,71
42,00	0,53	0,24	0,39	1,59	1,54	1,57
43,00	0,47	0,22	0,35	1,65	1,52	1,59
44,00	0,40	0,50	0,45	1,62	1,67	1,64
45,00	0,39	0,21	0,30	1,54	1,85	1,69
46,00	0,38	0,31	0,35	1,67	1,64	1,65
47,00	0,49	0,32	0,41	1,64	1,48	1,56
48,00	0,32	0,50	0,41	1,39	1,69	1,54
49,00	0,31	0,58	0,45	1,61	1,74	1,67
50,00	0,29	0,46	0,38	1,65	1,75	1,70
51,00	0,46	0,66	0,56	1,56	1,58	1,57
52,00						
53,00	0,66	0,25	0,46	1,59	1,38	1,49
54,00	0,66	0,61	0,64	1,45	1,68	1,57
55,00	0,54	0,42	0,48	1,75	1,58	1,66
56,00	0,33	0,63	0,48	1,34	1,59	1,47
57,00		0,44	0,44		1,53	1,53
58,00	0,51	0,65	0,58	1,45	1,55	1,50
59,00		0,52	0,52		1,68	1,68
60,00	0,70	0,49	0,60	1,89	1,56	1,72
61,00	0,50	0,45	0,48	1,57	1,52	1,55
62,00	0,58	0,50	0,54	1,57	1,62	1,60
63,00	0,50	0,06	0,28	1,56	1,23	1,39
64,00	0,51	0,43	0,47	1,53	1,50	1,51

Appendix E

Table E: *C. wuellerstorfi*

Depth (cm)	1 $\delta^{13}C$ (CW)	2 $\delta^{13}C$ (CW)	Average $\delta^{13}C$ (CW)	1 $\delta^{18}C$ (CW)	2 $\delta^{18}C$ (CW)	Average $\delta^{18}O$ (CW)
1,00	0,50		0,50	2,82		2,82
4,00	1,06		1,06	2,90		2,90
5,00	1,27		1,27	2,85		2,85
6,00	1,24		1,24	2,71		2,71
7,00	1,03		1,03	2,85		2,85
8,00	1,10	0,93	1,02	3,04	2,76	2,90
11,00	1,11	1,19	1,15	2,61	2,91	2,76
12,00	1,02		1,02	2,74		2,74
13,00	0,85		0,85	2,83		2,83
14,00	1,38		1,38	2,73		2,73
18,00	0,71		0,71	2,92		2,92
20,00	0,79		0,79	2,93		2,93
22,00	1,09		1,09	2,85		2,85
24,00	1,22		1,22	2,74		2,74
25,00	0,79		0,79	2,91		2,91
27,00	1,14		1,14	2,85		2,85
28,00	0,89		0,89	2,87		2,87
29,00	1,15		1,15	2,87		2,87
30,00	0,71		0,71	2,94		2,94
32,00	1,18		1,18	2,84		2,84
33,00	0,59		0,59	2,48		2,48
34,00	1,21		1,21	2,75		2,75
35,00	1,11	1,14	1,13	2,88	2,97	2,93
36,00	0,86		0,86	2,78		2,78
37,00	1,16		1,16	2,72		2,72
38,00	0,84		0,84	2,84		2,84
39,00	1,32		1,32	2,98		2,98
40,00	1,26	0,67	0,97	2,74	2,68	2,71
41,00	0,88	1,17	1,03	2,78	2,79	2,79
42,00	1,27	1,24	1,26	2,76	2,73	2,75
43,00	0,89		0,89	2,75		2,75
44,00	1,02		1,02	2,82		2,82
45,00	1,24	0,91	1,08	2,76	2,77	2,77
46,00	0,68	1,03	0,86	2,83	2,79	2,81
47,00	1,24		1,24	2,84		2,84
48,00	1,13	1,22	1,18	2,69	2,75	2,72
49,00	1,09	1,22	1,16	2,71	2,74	2,73
50,00	1,15	0,70	0,93	2,93	2,70	2,82

51,00	0,64		0,64	2,85		2,85
52,00	1,09	1,23	1,16	2,84	2,90	2,87
53,00	1,24		1,24	2,96		2,96
54,00	1,08		1,08	3,01		3,01
55,00	1,08		1,08	2,93		2,93
56,00	1,06		1,06	2,88		2,88
58,00	1,09		1,09	2,83		2,83
61,00	0,71		0,71	2,84		2,84
62,00	0,55		0,55	2,86		2,86

Appendix F

Statistics

In order to verify the reproducibility of the measurements, statistical analyses have been carried out on all data sets used in this study.

GS06-144-09 MC-D:

Sortable silt mean grain-size

The down-core deviation from the mean of each replicate has been calculated to be ± 0.0987 ‰ (based on run 2 & 3), and show a normal distribution (Fig. F.1).

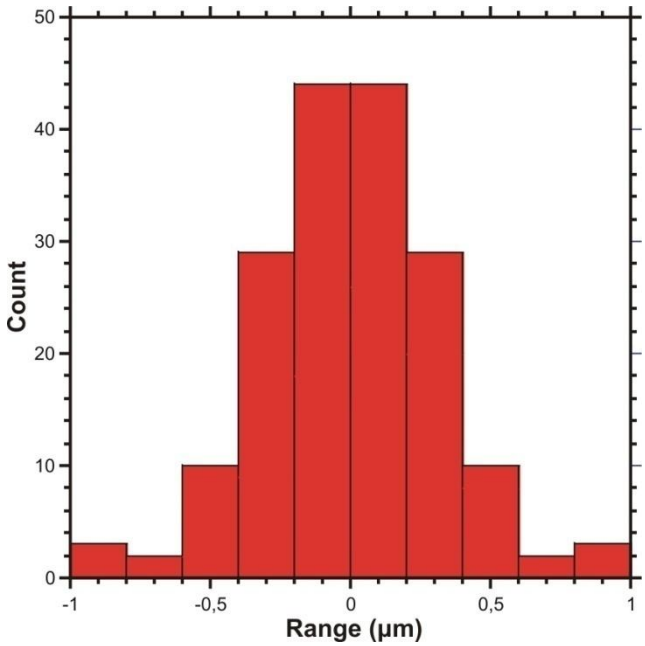

Fig. F.1: Replicates deviation from the mean of the sortable silt mean grain-size data set. The x-axis displays the range given in ‰, and the y-axis displays the number of counts.

The standard deviation (SD) has been calculated for the whole dataset using equation F.1, where $\bar{x}$ is the mean value of all replicates in each interval, x is the value of each measurement, n is the number of replicates (176), and k is the total number of intervals with replicates (88).

$$SD = \sqrt{\frac{\sum(\bar{x}-x)^2}{n-k}} \qquad \text{Equation F.1}$$

The SD for the sortable silt mean grain-size measurements is ±0.44 µm. The standard error of the mean (SEM) in each interval was calculated using equation F.2, where n indicates the number of replicates within the interval. The SEM for the sortable silt mean grain-size measurements with two replicates (n=2) is ± 0.31 µm.

$$\text{SEM} = \frac{SD}{\sqrt{n}} \qquad \text{Equation F.2}$$

The SEM of the 3 point running mean can similarly be calculated using equation F.2, and is ± 0.18 µm.

The standard deviation and the standard error for the oxygen isotope measurements have been calculated for each foraminifer species using equation F.1 and F.2.

G. bulloides

The average deviation of the mean $\delta^{18}O$ of all replicate is ± 0.084 ‰, and its distribution is shown in figure F.2. The standard deviation for the whole dataset is ± 0.15 ‰, while the standard error for intervals with two replicates is ± 0.11 ‰.

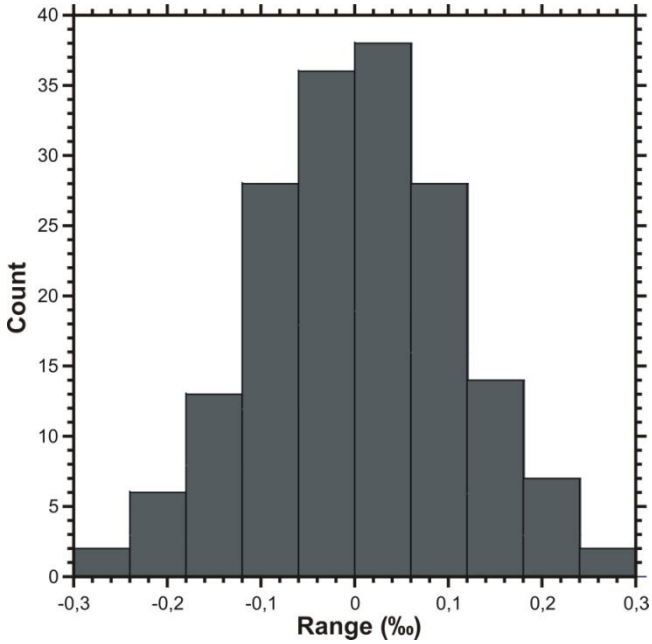

Fig. F.2: The distribution of the average deviation from the mean of all *G. bulloides* $\delta^{18}O$ replicates. The x-axis displays the range given in ‰, and the y-axis displays the number of counts.

N. pachyderma (d)

The average deviation of the mean $\delta^{18}O$ of all replicate is ± 0.057 ‰, and its distribution is show in figure F.3. The standard deviation for the whole dataset is ± 0.097 ‰, while the standard error for intervals with two replicates is ± 0.069 ‰.

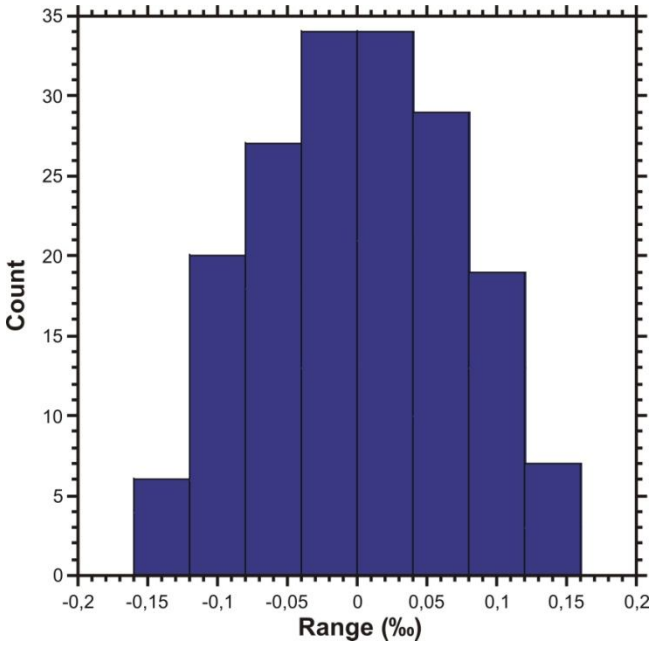

Fig. F.3: The distribution of the average deviation from the mean of all *N. pachyderma* (d) $\delta^{18}O$ replicates. The x-axis displays the range given in ‰, and the y-axis displays the number of counts.

G. inflata

The average deviation of the mean $\delta^{18}O$ of all replicate is ± 0.057 ‰, and its distribution is show in figure F.4. The standard deviation for the whole dataset is ± 0.1 ‰, while the standard error for intervals with two and three replicates are ± 0.073 ‰ and ± 0.059 ‰, respectively.

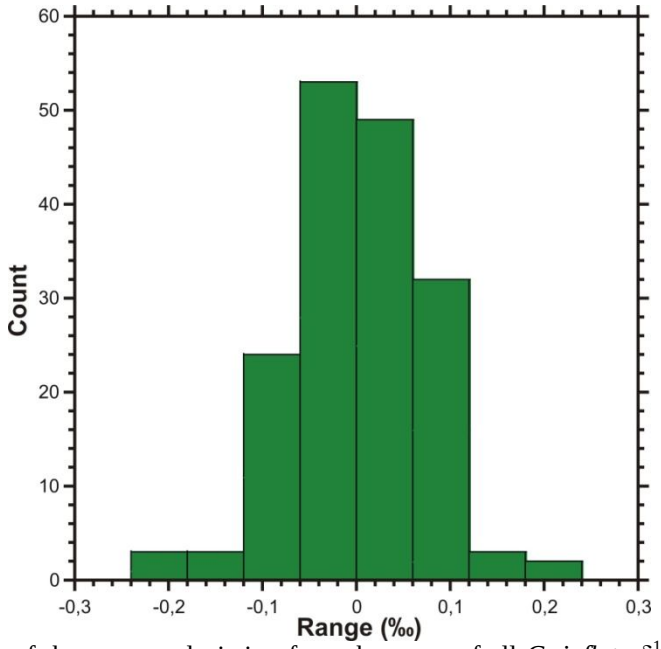

Fig. F.4: The distribution of the average deviation from the mean of all *G. inflata* $\delta^{18}O$ replicates. The x-axis displays the range given in ‰, and the y-axis displays the number of counts.

GS06-144-08 GC:

<u>*N. pachyderma* (d)</u>

The average deviation of the mean $\delta^{18}O$ of all replicate is ± 0.066 ‰, and its distribution is show in figure F.5. The standard deviation for the whole dataset is ± 0.12 ‰, while the standard error for intervals with two replicates is ± 0.085 ‰.

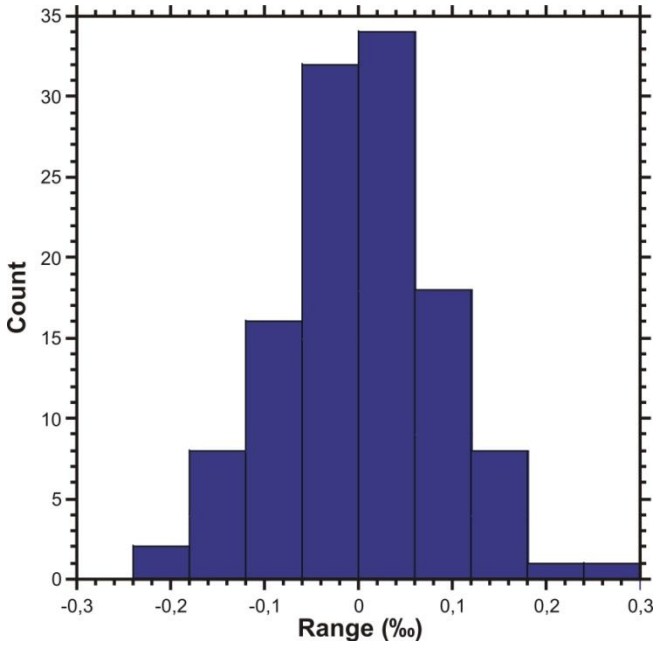

Fig. F.5: The distribution of the average deviation from the mean of all *N. pachyderma* (d) $\delta^{18}O$ replicates. The x-axis displays the range given in ‰, and the y-axis displays the number of counts.

C. wuellerstorfi

The average deviation of the mean $\delta^{18}O$ of all replicate is ± 0.05 ‰, and its distribution is show in figure F.6. The standard deviation for the whole dataset is ± 0.1 ‰, while the standard error for intervals with two replicates is ± 0.071 ‰. For the intervals with only one measurement, the standard error is assumed to be the same as the standard deviation.

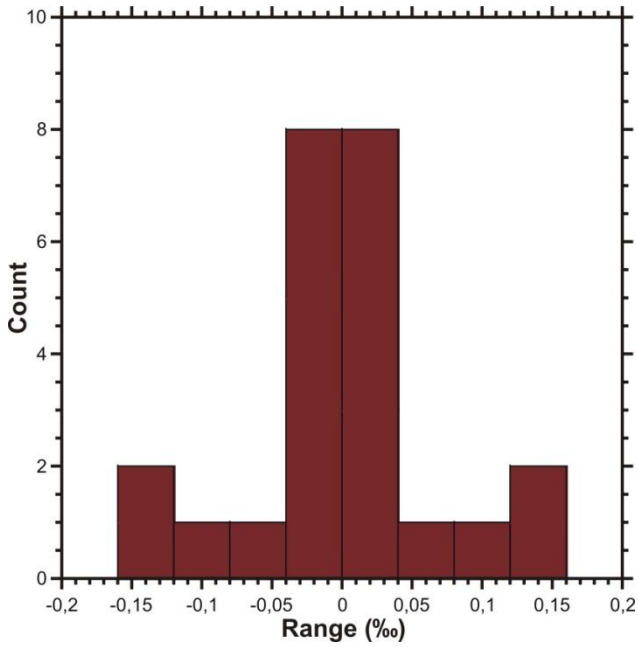

Fig. F.6: The distribution of the average deviation from the mean of all *C. wuellerstorfi* $\delta^{18}O$ replicates. The x-axis displays the range given in ‰, and the y-axis displays the number of counts.

Appendix G

Salinity and seawater $\delta^{18}O$ relationship in the study area

The regional mixing line in the study area between salinity and $\delta^{18}O$ of seawater was estimated from salinity and $\delta^{18}O$ data gathered from Schmidt et al. (1999) (Fig. G.1). The full dataset consists of 120 measurements of salinity and seawater $\delta^{18}O$ collected between 50-70°N, and 30-10°W. In order to achieve the most realistic mixing line, only the measurements closest to the core site was used (94 measurements) (Pers. comm. U. S. Ninnemann).

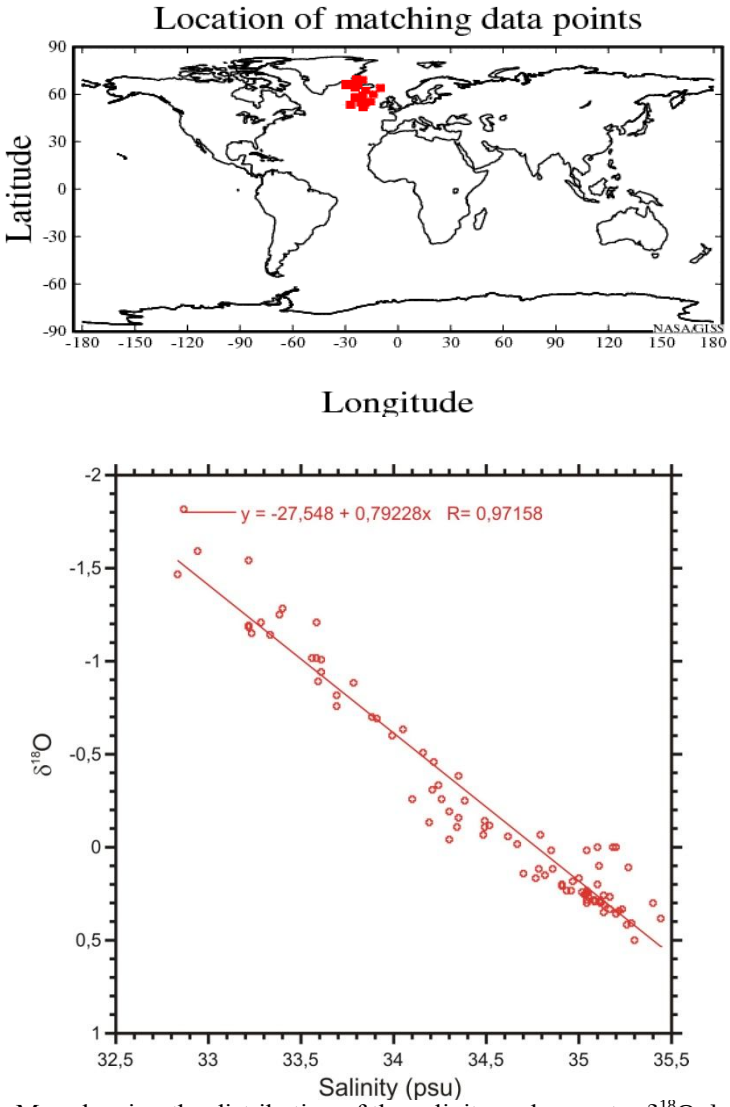

Fig. G.1: ***Upper panel*****:** Map showing the distribution of the salinity and seawater $\delta^{18}O$ data used for estimating the regional mixing line. ***Lower panel*****:** Plot showing the relationship between salinity and $\delta^{18}O$ of seawater in the study area. The mixing line is estimated by a linear fit through the data points. Map and data are gathered from Schmidt et al. (1999).

Appendix H

Core top $\delta^{18}O$ from planktonic foraminifera vs. $\delta^{18}O$ of equilibrium calcite

The different planktonic foraminifer species used in this study do not inhabit a specific depth during their life-cycle (subchapter 3.4.1). For example some species sink deeper into the water column during reproduction (Kohfeld et al., 1996; Simstich et al., 2003; Nyland et al., 2006). In order to constrain the calcification depth and timing of the foraminifers, core-top $\delta^{18}O_c$ is compared with the $\delta^{18}O$ value of equilibrium calcite ($\delta^{18}O_{ec}$) in the surface waters. Around the core site the $\delta^{18}O$ value of the surface waters ($\delta^{18}O_w$) is ~0.3 ‰ (VSMOW)(Schmidt et al., 1999).

Equilibrium calcite was calculated from oceanographic data gathered from the World Ocean Atlas 2005 (Antonov et al., 2006; Locarnini et al., 2006), which is presented here in table H.1 and H.2. First we used the salinity temperature relationship for the core site outlined in chapter 5.2 (Schmidt et al., 1999, Equation H.1). Thereafter, the $\delta^{18}O_w$ is reconverted from the VSMOW scale to the VPDB scale using Equation H.2, presented by Niebler et al. (1999), which is modified after Coplen et al. (1983), and Hut (1987). Finally, the $\delta^{18}O_{ec}$ was calculated by using the reconverted paleo-equation of Shackleton (1974), presented like this by Niebler et al. (1999) (Equation H.3).

$$\delta^{18}O_w\ [‰\ (VSMOW)] = -27.548 + 0.79228 \times S\ (psu) \qquad \text{Equation H.1}$$

$$\delta^{18}O_w\ [‰\ (VPDB)] = 0.99973 \times \delta^{18}O_w\ [‰\ (VSMOW)] - 0.27 \qquad \text{Equation H.2}$$

$$\delta^{18}O_{ec}\ [‰\ (VPDB)] = \delta^{18}O_w\ [‰\ (VPDB)] + 21.9 - \sqrt{310.61 + 10 \times T(°C)} \qquad \text{Equation H.3}$$

Table H.1: Salinity (psu) changes at 23.5°W, 60.5°N. Abbreviations: Winter = January-March, Spring = April-June, Summer = July-September, and Fall = October-December. Data collected from Antonov et al. (2006).

Depth (m)	Winter - S (psu)	Spring - S (psu)	Summer - S (psu)	Fall - S (psu)
0	35,1917	35,1905	35,1703	35,1776
20	35,2014	35,1749	35,1540	35,1915
50	35,2085	35,1792	35,1957	35,1924
75	35,2088	35,1813	35,2170	35,2017
100	35,2087	35,1819	35,2139	35,2081
150	35,2088	35,1789	35,2087	35,2098
200	35,2069	35,1751	35,2038	35,1998
250	35,2111	35,1793	35,2030	35,2028

Table H.2: Temperature (°C) changes at 23.5°W, 60.5°N. Abbreviations: Winter = January-March, Spring = April-June, Summer = July-September, and Fall = October-December. Data collected from Locarnini et al. (2006).

Depth (m)	Winter (T °C)	Spring (T °C)	Summer (T °C)	Fall (T °C)
0	8,0724	8,8187	11,4620	9,4062
20	8,1127	8,6922	11,3404	9,4415
50	8,1393	8,3802	10,1498	9,4156
75	8,1434	8,2015	9,2267	9,3059
100	8,1436	8,0966	8,8595	9,1472
150	8,1484	7,9487	8,5355	8,8788
200	8,1437	7,8833	8,3478	8,7028
250	8,1432	7,8361	8,2278	8,6096

A recent study as discovered that the $\delta^{18}O_c$ of foraminifers collected from core tops are 0.3 ‰ enriched compared with living foraminifers from the water column (Simstich et al., 2003). Thus, to correct for this anomaly, 0.3 ‰ has been added to the calculated $\delta^{18}O_c$ values. The results are presented in table H.3.

Table H.3: Calculated $\delta^{18}O_{eq}$ for the upmost 250 m at 23.5°W, 60.5°N. The values are presented relative to the VPDB scale, and are corrected for the 0.3 ‰ anomaly. Abbreviations: Winter = January-March, Spring = April-June, Summer = July-September, and Fall = October-December.

Depth (m)	Winter ($\delta^{18}O_{ec}$)	Spring ($\delta^{18}O_{ec}$)	Summer ($\delta^{18}O_{ec}$)	Fall ($\delta^{18}O_{ec}$)
0	2,4814	2,2927	1,6255	2,1360
20	2,4789	2,3121	1,6421	2,1382
50	2,4778	2,3939	1,9663	2,1453
75	2,4770	2,4406	2,2118	2,1800
100	2,4769	2,4675	2,3011	2,2246
150	2,4758	2,5026	2,3782	2,2930
200	2,4755	2,5161	2,4215	2,3291
250	2,4789	2,5314	2,4511	2,3549

Vital effects in *N. pachyderma* (d) have not been studied as much as *N. pachyderma* (s) and it has often been assumed that the morphotypes have the same vital effect (Niebler et al., 1999; Nyland et al., 2006). Due to the fact that there seem not to exist any studies concerning the vital effects in the *N. pachyderma* (d) morphotype, it is assumed that the vital effects found for *N. pachyderma* (s) is the same as *N. pachyderma* (d). Vital effects in *N. pachyderma* (s) has been calculated to be -0.4 ‰ (Wu & Hillaire-Marcel, 1994), -0.6 ‰ (Nyland et al., 2006), -0.7 ‰ (Kohfeld et al., 1996; Ortiz et al., 1996), and -0.9 ‰ to -1‰ (Bauch et al., 1997; Simstich et al., 2003).

The core top value of *N. pachyderma* (d) at 0 cm (~2002 AD) is 1.62 ‰. If one uses the -0.4 ‰ vital effect the value fits best at 50 m water depth (1.57 ‰) during summer, while with -0.5 ‰ vital effect the value fits best between 50-75 m (1.47-1.71 ‰) during summer, or 0-75 m (1.63-1.68 ‰) during fall. With a vital effect of -0.6 ‰ the value fits best with 75 m (1.61 ‰) during summer, or 100 m (1.62 ‰) during fall, while with a vital effect of -0.7 ‰ the best fit is 20-30 m (1.61-1.64 ‰) during spring, or 100-125 m (1.60-1.65 ‰) during summer. If one apply a vital effect of -0.8 ‰ to -1 ‰ the corresponding depth will be too deep in all four seasons, and is therefore unlikely.

N.pachyderma (d) is in this study assumed to calcify during summer, in agreement with Nyland et al. (2006), hence from the calculations above the species is most likely to calcify during summer at 50-125 m water depth. Pak & Kennett (2002) found *N. pachyderma* (d) to calcify between 50-75 m water depth, while Nyland et al. (2006) found around 50 m. Thus *N. pachyderma* (d) probably calcifies mostly between 50-75 m water depths, but some individuals may calcify as deep as 125 m water depth.

According to (Keigwin et al., 2005) *G. bulloides* calcifies in near equilibrium with the ambient water in spring and winter, which is in agreement with Sautter & Thunnell (1991). Other researchers have found a vital effect of -0.5 ‰ (Spero & Lea, 1996), and even as high as -0.95 ‰ (Mortyn & Charles, 2003). The core top value of *G. bulloides* is 1.51 ‰ (2002 AD).

If one assumes calcification in equilibrium with $\delta^{18}O_c$ none of the calculations match. With a vital effect of -0.5 ‰ the corresponding depth is 50 m (1.47 ‰) during summer, while with a vital effect of -0.9 ‰ the corresponding depth is 50 m (1.49 ‰) during spring or 200 m (1.53 ‰) during summer. If one assumes a vital effect of -1 ‰ the corresponding depth is 150-200 m (1.50-1.52 ‰) during spring. *G. bulloides* is assumed to calcify during spring to summer (subchapter 3.4.1) (Bemis et al., 1998) at depths between 0-50 m (Bemis et al., 1998; Niebler et al., 1999; Pak & Kennett, 2002). Based upon these studies, and the paleotemperature calculations, it is assumed most of the *G. bulloides* individuals calcify at depths between 0-50 m in late spring and summer, while some individuals may calcify as deep as 200 m.

G. inflata is known to deviate from $\delta^{18}O_{ec}$ by ± 0.4 ‰ (subchapter 3.4.1). Unfortunately we do not have any values of core top (0 cm) of *G. inflata*. Thus, the comparison will be with the value for 1 cm depth (~1989 AD), which is 1.91 ‰. If one applies a vital effect of -0.4 ‰ the best fit is 100 m (1.90 ‰) during spring, or 200 m (1.93 ‰) during fall, while with a vital

effect of -0.3 ‰ the corresponding depth is 75 m (1.91 ‰) during summer, or 100 m (1.92 ‰) during fall. Applying a vital effect of -0.2 ‰ the only reasonable match is 75 m (2.01 ‰) during summer. Vital effects from -0.1 ‰ to +0.4 ‰ give to shallow depths, and these calculations are disregarded, because *G. inflata* is known to be a relatively deep dwelling species (Niebler et al., 1999; Ganssen & Kroon, 2000; Mortyn & Charles, 2003; Cléroux et al., 2007). Based on the calculations, it seems like *G. inflata* calcifies at depths between 75-200 m, between late spring and early fall in the study area. This is in agreement with Niebler et al. (1999), Ganssen & Kroon (2000), Mortyn & Charles (2003) and Cléroux et al. (2007). The winter mixed layer is as deep as 200 m during late spring to early summer in the study area (Ganssen & Kroon, 2000), thus, since *G. inflata* lives as deep as 200 m below sea level, it is a good indicator for winter temperature/salinity changes (Cléroux et al., 2007).

Appendix I

^{210}PB dating

The results of the ^{210}Pb dating on core GS06-144-09 MC-D is presented here, as received from the Gamma Dating Center in Copenhagen. The estimated age and accumulation rate for each depth interval is presented in table 4.1, while figure I.1 shows an age versus depth plot based on the dating results, with the age uncertainty plotted as error bars. Figure I.2 shows the down-core variability of dry bulk density, unsupported ^{210}Pb content, and ^{137}Cs content.

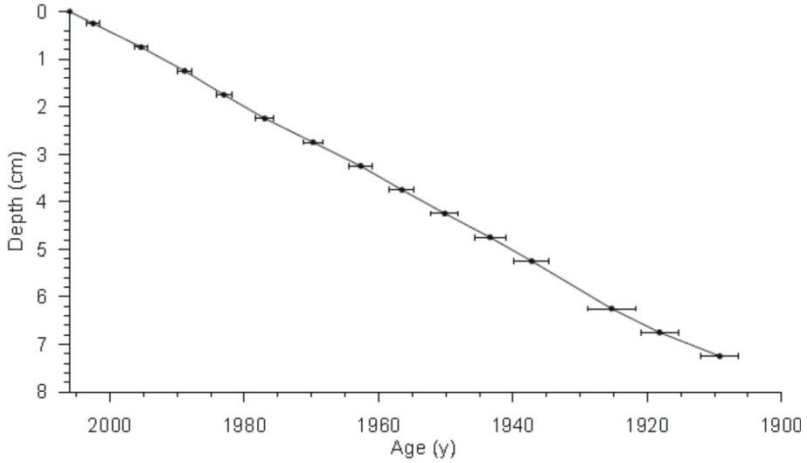

Fig. I.1: Plot over depth in the core (cm) versus estimated age (AD).

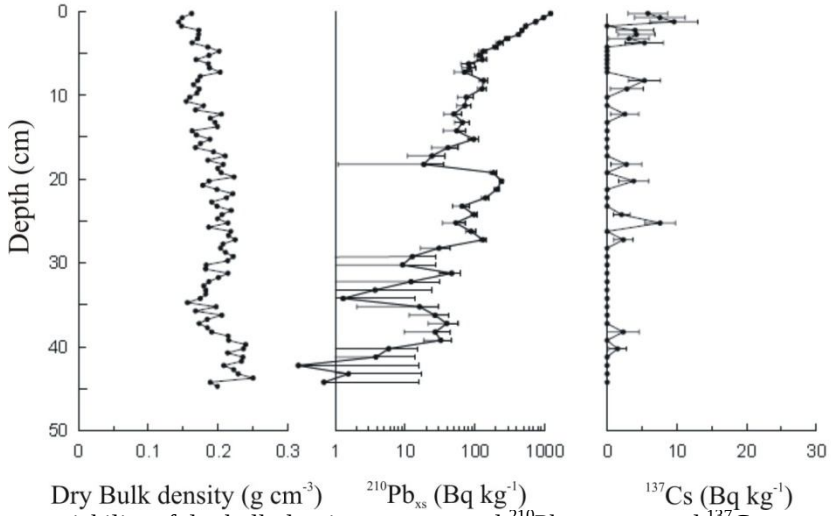

Fig. I.2: Down-core variability of dry bulk density, unsupported ^{210}Pb content, and ^{137}Cs content.

Appendix J

AMS ^{14}C dating

The results of the AMS ^{14}C dating of core GS06-144-09 MC-D and GS06-144-08 GC is presented here (Table J.1), as received from Leibniz-Laboratory for Radiometric Dating and Stable Isotope Research, Christian-Albrechts-University of Kiel, Germany.

Table J.1: Dates received 21.09.2007.

	Sample Description	Corrected pMC†	Conventional Age	$\delta^{13}C$(‰)‡
KIA 34242	GS06-144-09MC D ; 0 cm ; 1.0 mg C	99.06 ± 0.27	75 ± 20 BP	2.37 ± 0.13
KIA 34243	GS06-144-09MC D ; 11.5 cm ; 0.8 mg C	93.62 ± 0.24	530 ± 20 BP	-0.72 ± 0.12
KIA 34244	GS06-144-09MC D ; 30 cm ; 1.0 mg C	91.09 ± 0.22	750 ± 20 BP	1.60 ± 0.22
KIA 34245	GS06-144-08GC ; 0 - 1 cm ; 0.6 mg C	91.41 ± 0.27	720 ± 25 BP	0.43 ± 0.14
KIA 34246	GS06-144-08GC ; 0 - 1cm ; 1.0 mg C	91.04 ± 0.22	755 ± 20 BP	3.22 ± 0.14
KIA 34247	GS06-144-08GC ; 40 - 41 cm ; 0.7 mg C	84.87 ± 0.27	1350 ± 25 BP	-0.56 ± 0.27
KIA 34248	GS06-144-08GC ; 40 cm ; 1.0 mg C	83.84 ± 0.24	1400 ± 25 BP	2.15 ± 0.17
KIA 34249	GS06-144-08-GC ; 80 - 91 cm ; 1.0 mg C	78.13 ± 0.22	1980 ± 25 BP	2.00 ± 0.05
KIA 34250	GS06-144-08GC ; 119 - 120 cm ; 0.9 mg C	72.11 ± 0.21	2625 ± 25 BP	-0.83 ± 0.08
KIA 34251	GS06-144-08GC ; 120 - 121 cm ; 0.7 mg C	71.71 ± 0.21	2670 ± 25 BP	-0.57 ± 0.21

Appendix K

Spectral analysis of the phasing between ISOW flow vigor and AMO

Spectral analysis has been performed on the phasing between ISOW flow vigor and AMO (Fig. K.1). Figure K. 1 shows that the phasing between the two proxies is most significant at zero lag, representing about 50 % of the variability.

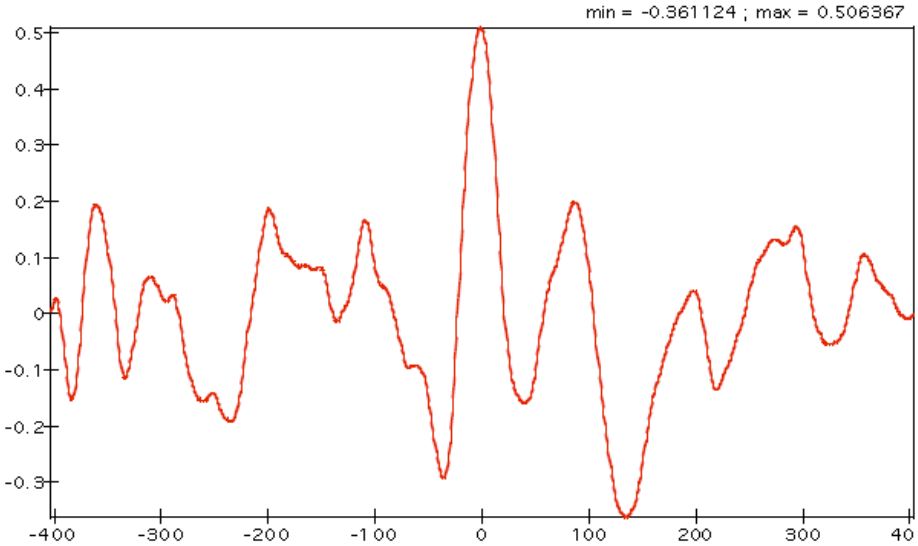

Fig. K.1: Spectral analysis showing the phasing between ISOW vigor and AMO. The ISOW data used in the analysis are with the adjusted age model. The analysis was performed by U. S. Ninnemann.

Appendix L

Climate forcing mechanism

Our records of ISOW paleocurrent and paleocirculation have shown multiple variations on both multidecadal, and centennial timescales over the past ~1350 years. The ultimate mechanism behind these variations is not known, but could be related to solar and volcanic forcings. Figure L.1 shows our proxies for paleocurrent and paleocirculation plotted versus solar and volcanic forcings.

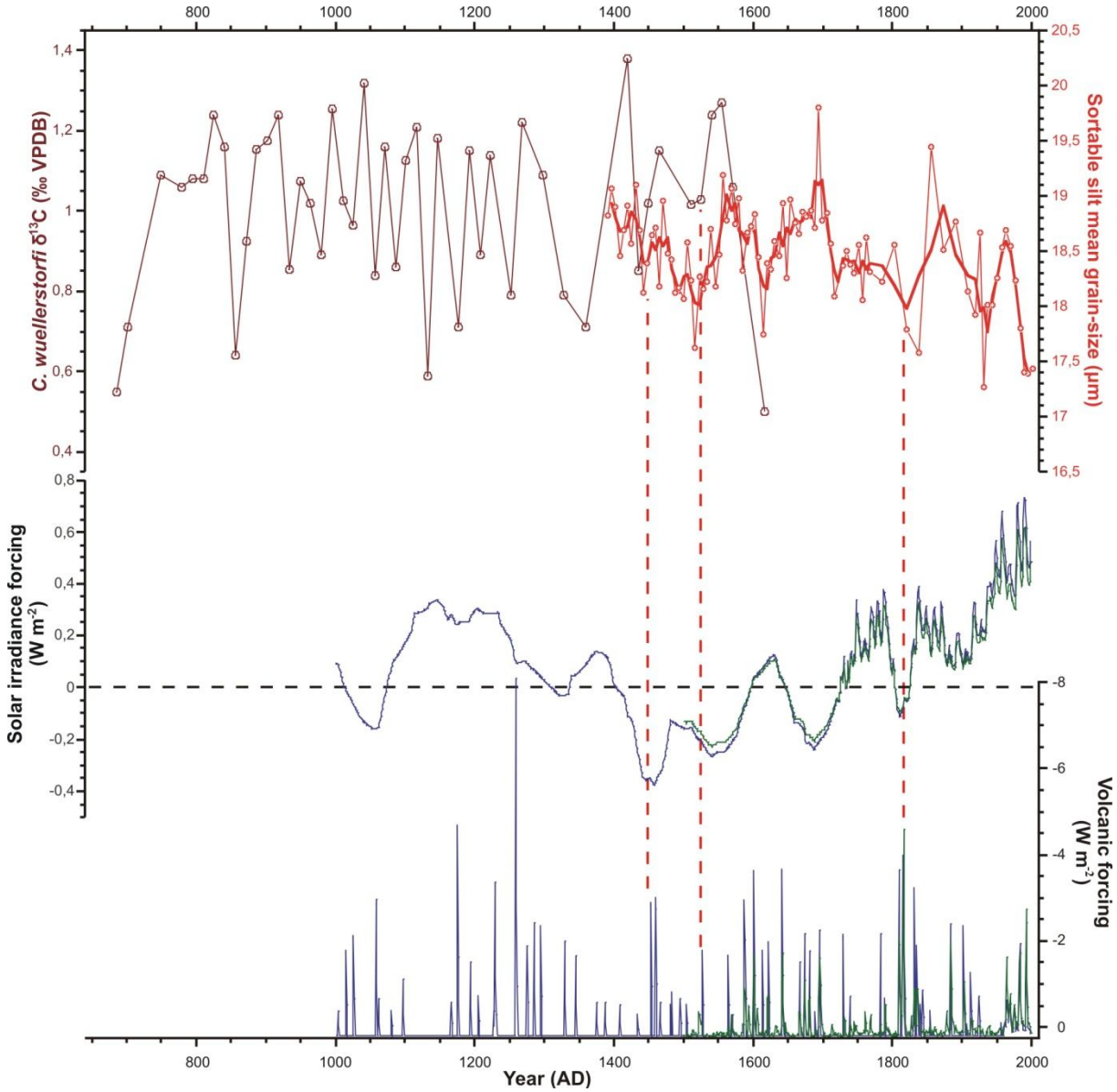

Fig. L. 1: ISOW paleocurrent and paleocirculation proxy plotted versus solar and volcanic forcing. Graphs in blue are from González-Rouco et al. (2003) (GSZ2003), for both solar and volcanic forcing, while graphs in green are from Tett et al. (2006) (TBC2006), for both solar and volcanic forcings. The red stippled line indicates coeval changes between all proxies.

These two simulations of solar and volcanic forcings are two of the 12 simulations used in the IPCC 4th assessment report (Jansen et al., 2007), and are used because they showed relatively good correlation with the western branch of the Nordic Seas overflows (Johansen 2008).

The paleocurrent and paleocirculation proxies show good correlation with solar and volcanic forcings at three occasions during the past ~600 years, ~1450 AD, ~1525 AD and ~1820 AD, where reduced overflow coeval with a reduced solar insolation and increased volcanic activity. During these events solar forcing seems to be the controlling factor, while the volcanic activity amplifies the signal. The event centered around 1450 AD involved reduced overflow in both overturning branches (Fig. 6.4). These findings suggest that some of the ISOW flow speed minima and $\delta^{13}C$ minima are forced, and that the response time of the ocean circulation to forcing is fast. Nevertheless, the lack of coherence between our proxies for ISOW variability and external forcing at several other occasion during the last ~600 years, indicate that the ocean has an internal variability that cannot be explained in a simple way by solar and/or volcanic forcing.